Title	Study for muonic atom formation and the following muon cascade process : Muon capture experiment for low pressure gases and Development of charge separation system after muonic atom formation
Author(s)	吉田, 剛
Citation	大阪大学, 2017, 博士論文
Version Type	VoR
URL	https://doi.org/10.18910/61484
rights	
Note	

Study for muonic atom formation and the following muon cascade process

- Muon capture experiment for low pressure gases and Development of charge separation system after muonic atom formation -

(ミュオン原子形成とそれに伴うミュオンカスケード過程に関する研究
-低圧気体でのミュオン捕獲実験およびミュオン原子形成後の電荷選別システムの開発-)

Go YOSHIDA

A Thesis Submitted to Graduate School of Science,

Osaka University

2017

Abstract

A negatively charged muon is one of the elementary particles with property of the same charge of electron and 2.2 μs of lifetime, and 105.6 MeV/c^2 of rest mass. The muon can create the orbital on the nucleus like atomic electrons. Such an atomic system which has a muon as the constituent other than the nucleus and electrons is called “muonic atom”. Although a muonic orbital is much smaller than an electronic orbital due to heavy mass of a muon, valence electrons or weak binding atomic electrons strongly influence the initial stage of muon capture process. When the muon is captured by a molecule, muonic atom formation process, such as muon capture probability in constituent atom, is affected by the electron arrangement around the muon capturing atom. However, the details of muon capture process such as the interaction among captured muon and electrons, the initial state of captured muon and electron state after formation of muonic atom have still not been understood.

In this thesis, to reveal the interaction among the muon and atomic electrons in the initial stage of muonic atom formation, muon irradiations for low pressure gases (CO, CO_2, COS, and CS_2) were performed at the J-PARC, Japan. Sample densisties were enough low to be regarded as isolated state after muonic atom formation. Muonic X-rays emitted from muonic atom were measured by germanium semiconductor detectors. From the analysis of muonic X-rays, the muon capture ratio and the muonic X-ray structure were obtained. Muonic X-ray structure reflects initial quantum state (principal quantum number and angular momentum quantum number) of captured muon. The muon irradiation study was also conducted for hydrogen mixture gas samples to provok the muonic atom formation via muon transfer that occur only in hydrogen

containing system.

The large chemical environmental effect in the muonic atom formation was found especially in carbon oxides. The muon capture process for the carbon atom in CO molecule was clearly different from these for CO_2 and COS. Per atom muon capture ratio of carbon to oxygen atom in CO; $A(C/O)_{CO}$, is 30 % larger than that in CO_2, or COS. Distribution of the initial angular momentum quantum number of captured muons in carbon atom was also different in CO from that in CO_2 and COS. On the other hand, initial angular momentum quantum number distribution of muons captured by oxygen atoms was almost same among CO, CO_2, and COS. From these result, the contribution of the lone pair electrons on the carbon atom in CO molecule in muon capture phenomena was firstly deduced quantitatively.

To verify the atomic electron state just after formation of muonic atom, a new experimental mothod to investigate the charge state of muonic atom was proposed. As the first step for this study, the muonic atom extraction and charge separation system was developed based on a TOF-MS technique. Although the details of muon cascade process have still not been understood, it is known that the muonic atom loses their electrons by Auger process and becomes multi-valent positive ion. When a molecule captures a muon, the molecule loses their original structure due to Coulomb explosion. Charge state of muonic atom can be distinguished by TOF-MS, and the system can be applicable to create the muonic atom beam. Evaluation and optimization of the system was performed using the ion generation by laser ablation. Mass resolution R = 260 was achieved and this value is sufficient to distinguish muon mass (0.1 u). Preliminary experiment using muon beam was performed at J-PARC, and the background signals accompaning muon beam were evaluated.

Table of Contents

Chapter1. General Introduction

1.1 Character of Muon

A muon is one of elementally particles belonging to lepton (see Figure 1). Muon was discovered by Carl D. Anderson and Seth Neddermeyer in 1936, while studying cosmic radiation [1]. A muon has a positive or negative electrical charge same as an electron. Rest mass of muon is 105.6 MeV/c^2, this is 206.7 times of mass of electron. A muon has individual life time of 2.2 μs in vacuum, and decay to two neutrinos and an electron; $\mu^- \rightarrow \nu_\mu + e^- + \nu_e$.

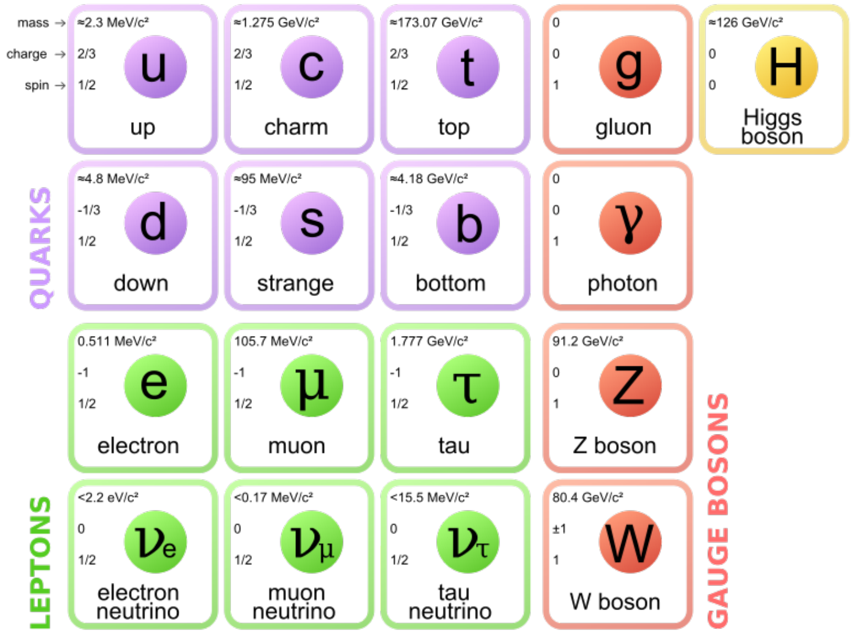

Fig.1-1 Standard model of elementally particles [2].

1.2 Muonic atom

A negatively charged muon (muon) can form an atom like system with a nucleus, so called exotic atom. An exotic atom is an atomic system which consists of sub-atomic particles (proton, neutron and electron) and one or more other particles whose charge is same as the replaced particles [3]. For example, when electrons might be replaced by other negatively charged particles such as muons or pions, the atomic systems are called muonic atoms and pionic atoms, respectively. These substitute particles are usually unstable, thus, exotic atoms typically have very short lifetimes.

In this thesis, muonic atom formation process was studied. Muonic atom is an atomic system which has a negatively charged muon substituted for an electron. When a muon enters in a substance, the muon loses its kinetic energy by collisions with electrons in a substance in accordance with the Bethe–Broch equation. Finally, the muon is captured by the coulomb field of a nucleus when its kinetic energy decrease to several ten eV, and then a muonic atom is formed [4].

In a muonic atom, the muon has particular orbital like an orbital electron. Muon and electron are different particle each other, the muon creates an atomic orbital completely different from that of electron. Bohr radius of the muonic orbit is shown in formula (1-1). Because a muon is about 200 times heavier than an electron, a muonic orbit is 200 times smaller than an electronic orbital (0.0028 Å). An orbital muon exists very close to the nucleus than orbital electrons. Schematic view of muonic atom is shown in Fig. 1-2. A muon creates an “orbital” but this figure shows an “orbit” for the convenience.

$$r_n = \frac{\epsilon_0 n^2 h^2}{\pi m e^2} \qquad (1\text{-}1)$$

r_n : radius of orbit

h : Plank constant

ε_0 : permittivity of vacuum

m : mass of particle

e : elementary charge

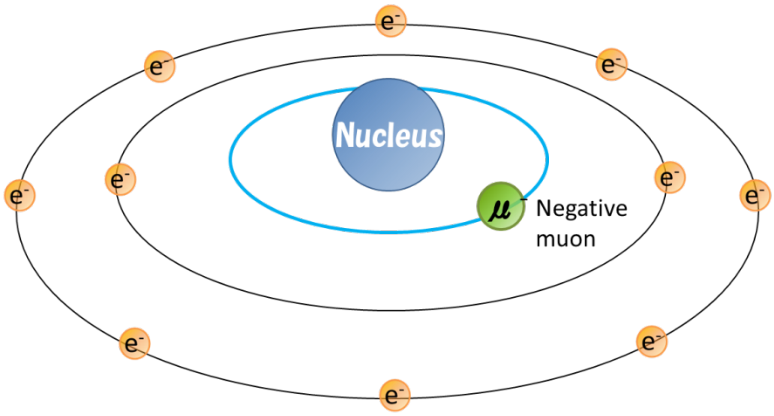

Fig.1-2 Schematic view of muonic atom. In a muonic atom, the muon has the individual orbital like an orbital electron. Muon and electron are different particle each other, the muon creates an orbital different from electronic orbital. Muonic orbit is about 200 times smaller than electronic orbit. Note, a muon creates an "orbital" but this figure shows an "orbit" for the convenience.

Due to the strong shielding effect by orbital muon for the nuclear charge in muonic Z atom, the effective charge of the nucleus looks like Z-1 from orbital electrons. So, it is believed that a muonic Z atom behaves as if a Z-1 atom. Actually, slightly differences between a muonic Z atom and a Z-1 atom are also observed, though the K-series electronic X-ray energies of Z-1 atom are almost same as those of muonic Z atom after its formation [5,6]. On the other hand, the kinetic isotope effects in muonic helium (consisting of a helium nucleus, an electron and a negatively charged muon) regarded as a heavy hydrogen isotope and muonium (consisting of a positively charged muon and an electron) regarded as a light hydrogen isotope were also reported by μSR method [7]. However, the chemical properties of the muonic atoms still have been hardly investigated from the view point of valence electron arrangement.

1.3 Muon cascade process

In a muonic atom, the muon has quantum numbers like orbital electrons (principal quantum number: n, angular momentum quantum number: l). Just after a muon is captured by an atom, the captured muon is in a highly exited state, and immediately de-excites to the muonic 1s atomic state [8]. Initially, the muon de-excitation by Auger process is dominant, because the radius of muonic orbital is large and the wave function of the orbital muon has relatively large overlap with the wave functions of orbital electrons. When the muon de-excites deeply and electron density around the muon becomes small, the muon emits characteristic X-rays (muonic X-ray) in muon de-excitation. Whole these continuous muon de-excitation processes are called as muon cascade process. After the muon reached the muonic 1s atomic state, the muon decays with mean life of 2.2 μs or is absorbed by the nucleus with weak interaction [9]. These processes are competitive with each other. The schematic view of muon de-excitation is shown in Fig. 1-3.

The muon emits Auger electrons and/or muonic X-rays during its de-excitation. From measuring of Auger electrons, muonic X-rays and charge state of muonic atom, the muon cascade process and the initial state of captured muon (Fig. 1-4) can be investigated. The electron state of muonic atom after formation has never been known. Auger electron measurement is also very difficult and only pioneering work was known [10]. On the other hand, muonic X-ray measurement can be achieved using semiconductor photon detectors due to high energy of muonic X-rays. Cascade path of muon can be estimated by analyzing muonic X-ray structure, that is, muonic X-ray emission intensity pattern such as muonic Lyman lines using simulation of muon cascade process [11,12]. There are many studies to understand muonic atom formation process from muonic X-ray measurement. But detail state of the muon in muon cascade process has still been not understood.

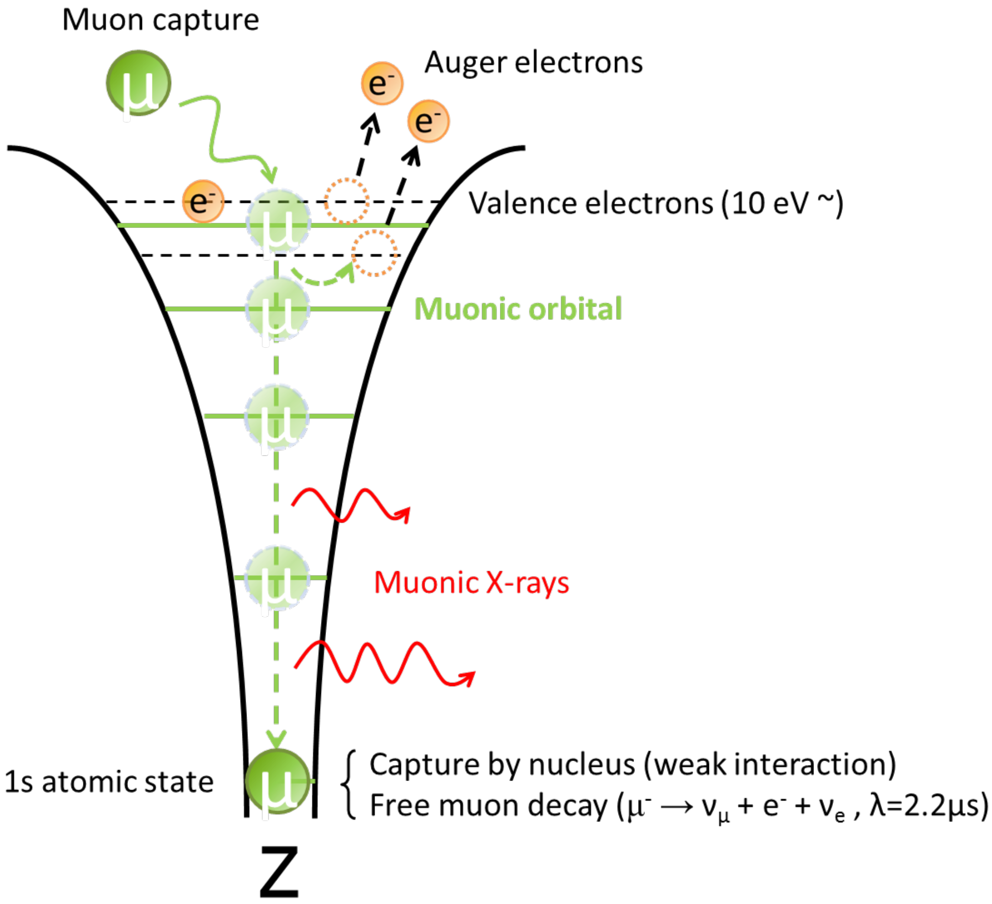

Fig. 1-3 Schematic view of muon capture and muonic atom formation. Muon is captured in highly excited state and immediately de-excite to muonic 1s state. Muonic de-excitation process consists of Auger electron emittions and characteristic X-ray (muonic X-ray) emission. After the muon reached a muonic 1s atomic state, the muon will decay with mean life of 2.2 μs or will be absorbed by a proton with weak interaction.

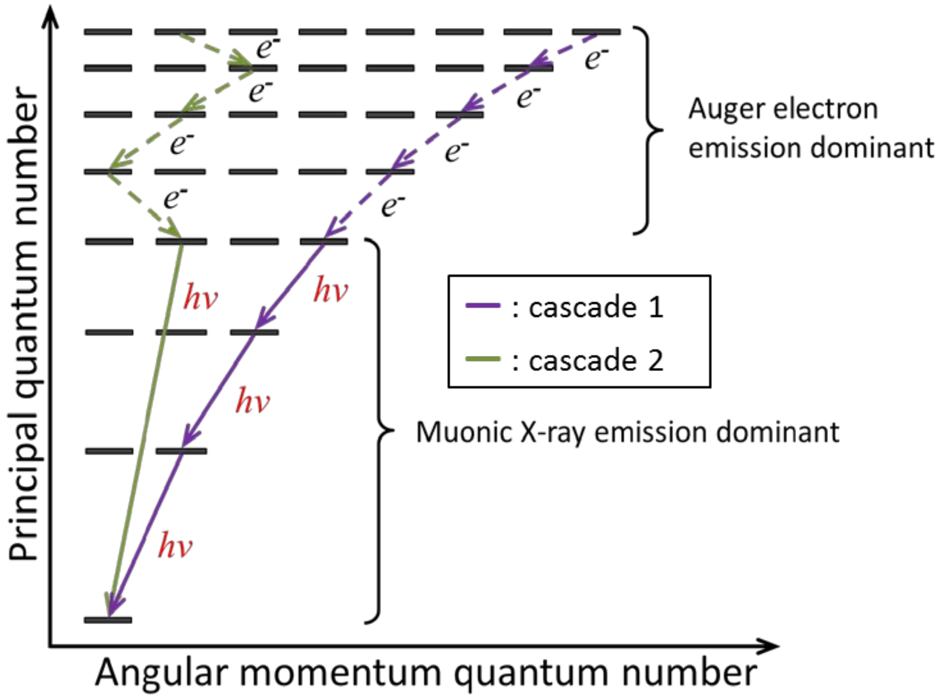

Fig.1-4 Schematic view of transition paths in muonic de-excitation. Muonic X-ray emission pattern is reflected by initial quantum state of captured muon.

1.4 Muon transfer from muonic hydrogen atom

When a muon is captured by a hydrogen atom, the only electron in the atom is replaced by the muon and muonic hydrogen atom (μ^-p) is formed. The muonic hydrogen atom is small size neutral atom and regarded as an electrically neutral particle. In fact, muonic hydrogen atom can diffuse in the substance easily like a neutron. Muonic hydrogen atom can penetrate electron cloud without coulomb repulsion and can approach to very close to the nucleus of other atom. When the muonic hydrogen atom reaches to near the heavier nucleus ($Z > 2$), the muonic hydrogen atom gives the muon to the deeper atomic levels of the nucleus. This phenomenon is called muon transfer process. Because the energy potential of the muon accepter is more stable than that of the muon donor (muonic hydrogen atom), thus, muon transfer process progresses spontaneously. Schematic view of muon transfer is shown in Fig. 1-5.

A muon captured by hydrogen atom transfers to other atom from excited state or from 1s (ground) state of the muonic hydrogen. Because of very short life of muonic excited state, former case only occurs in high dense system and intermolecular system. For example, a hydrogen atom in hydrocarbon molecule captures a muon and immediately gives the muon to just near the bonding carbon. On the other hand, the latter case occurs anywhere as long as muonic hydrogen atom exists. The muon can transfer only to the orbital having larger binding energy than the energy of 1s state of muonic hydrogen atom (μ^-p 1s : 2.531 keV), that is, principal quantum number and angular momentum quantum number of transferred muon become small than the case of muon captured by an atom directly. As a result, in the muon transfer process, because of the difference of initial quantum state of the muon, muonic X-ray structure becomes different from that of the muon captured by an atom directly.

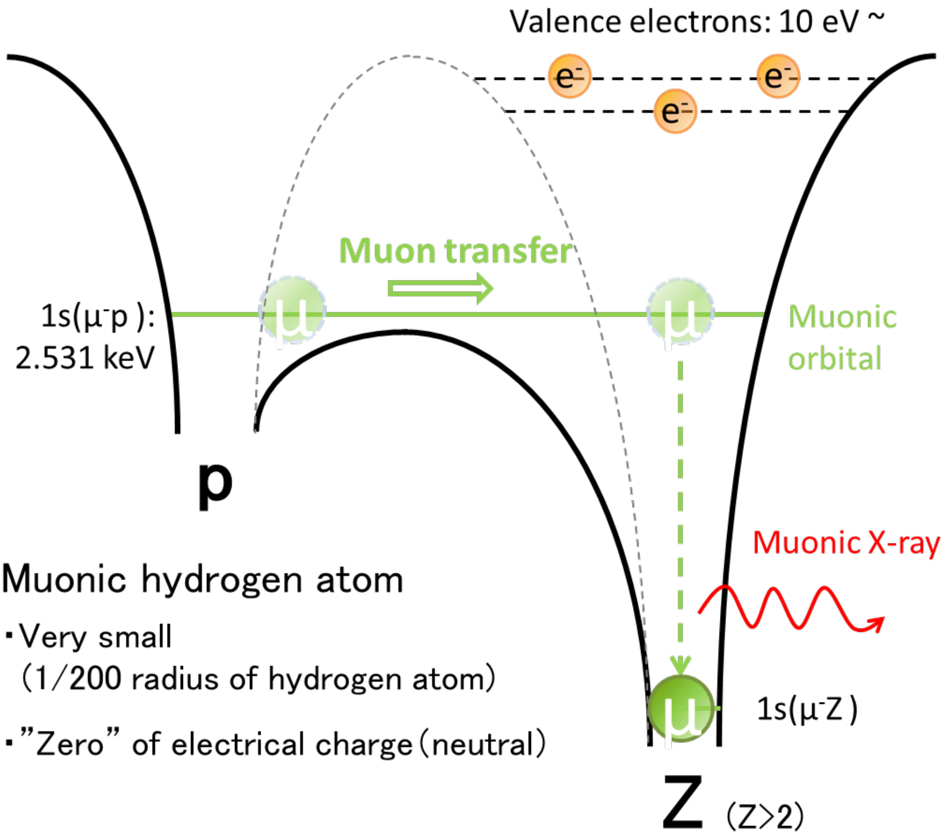

Fig. 1-5 Muon transfer from muonic hydrogen atom (μ^-p) to Z. muon can only transfer to the orbit has larger binding energy than the energy of 1s state of muonic hydrogen atom (μ^-p 1s : 2.531 keV).

1.5 Chemical environmental effect of muonic atom formation

It is known that the muonic atom formation process is influenced by the chemical environment of muon captureing atom. This is known as “chemical effect”. For example, in a case of muons were captured by boron nitrides which have two different structures; one is cubic like diamond, the other is hexagonal like graphite, relative muon capture probability of boron atom to nitrogen atom has 20 % difference between two structures [13]. Difference of muonic X-ray structures depending on molecular structures was also reported in the same literature [13]. This result implies that the electron arrangement around the muon capturing atom contributes to muon capture phenomenon though the muonic orbital is much smaller than these of electrons.

Many theoretical and/or empirical models have been proposed to explain muonic atom formation process. The first approach was performed by Fermi and Teller (Fermi-Teller’s Z-low) [4]. They described energy loss processes of the muon (and other negatively charged particle which are called meson at the period) in the substance based on classical collision theory. In this model, muon capture probability of atom in the molecule shown as Z_1Z_2, is described as (1-3).

$$A(Z_1/Z_2) = \frac{Z_1}{Z_2} \qquad (1\text{-}3)$$

This model only considers the charge of nucleus which captures a muon, and the electron arrangement around muon capturing atom were out of consideration. Many experimental results of muon capture ratios have showed a deviation from Z-low. These results suggested that the muon capture probability depended on elemental periodicity of the muon (and other particles like a pion) capturing atom.

Petrukhin revised Z-low [14] based on the stopping power of pions in various density hydrogen samples experimentally. In this model, muon capture probability of atom is proportional to $Z^{1/3}$ described as (1-4)

$$A(Z_1/Z_2) = \frac{Z_1^{\frac{1}{3}} - 1}{Z_2^{\frac{1}{3}} - 1} \qquad (1\text{-}4)$$

Petrukhin's model well reproduced experimental result than the Z-low, though this model also could not explain dependence to the elemental periodicity of muon capture probability of atom.

Daniel revised Z-low based on Thomas–Fermi statistical model [15,16], and muon capture probability is described as (1-5) [17]. After that, Daniel involved influence of shield of nuclear charge by atomic electrons and atomic radius of muon capturing atom in the Z-low described as (1-6) [18,19].

$$A(Z_1/Z_2) = \frac{Z_1^{\frac{1}{3}} \ln(0.57Z_1)}{Z_2^{\frac{1}{3}} \ln(0.57Z_2)} \qquad (1\text{-}5)$$

$$A(Z_1/Z_2) = \frac{Z_1^{\frac{1}{3}} \ln(0.57Z_1) \cdot R(Z_2)}{Z_2^{\frac{1}{3}} \ln(0.57Z_2) \cdot R(Z_1)} \qquad (1\text{-}6)$$

Daniel's model much well reproduced experimental result than the Petrukhin's model, and could explain the dependence to the elemental periodicity of muon capture probability of atom. But, Daniel's model could not explain the differences of muon capture ratio depending on molecular structures like allotropes.

Same as muonic atom, a chemical environment effect on pionic atom formation process also reported. A pion which is attributed to meson has same charge as a muon, thus a negatively charged pion can be captured by a nucleus and the pionic atom is formed. In a pionic atom, the pion is absorbed by the nucleus with strong interaction, unlike the case of muon. As a remarkable aspect for pion capture, when a pion is captured by hydrogen atom, two gamma rays corresponding to the pion mass energy are emitted in the opposite direction each other. Because a pion can interact with proton by the strong interaction, the following reaction is provoked; $\pi^- + p \rightarrow n + \pi^0$, $\pi^0 \rightarrow 2\gamma$ (140MeV , $\lambda \sim 10^{-14}$ s). The probability of π^0 generation depends on Panovsky ratio [20,21]. These gamma rays were measured using scintillation counters and/or Cherenkov counter, and a lot of pion capture experiments for hydrogen containing system such as various organic compounds and metal hydrides have been performed.

From these experiments, chemical environmental effects on pion capture were discovered. The pion capture probability in hydrocarbon was very low, and relative pion capture probability for hydrogen atom was changed by structure of pion capturing molecule. To explain the chemical environmental effect for pion capture, Ponomarev established the Large Molecular model (LMM model) which is assumed the mesomolecular orbital in the initial process of muon capture [22]. At the later, Schneuwly revised the Ponomarev’s model so that can be applying for general compounds, from results of muon capture for various oxides [23].

In the Schneuwly’s model, a negatively charged particle is captured in the substitution of an electron. The capture ratio of a particle for compound depends on the number of electrons; covalent and localized (atomic) electrons. When a negatively charged particle is captured in the substitution of a covalent electron, it exists in a "mesomolecular orbital" and then transfers to a mesoatomic orbital by radiation transition. So the particle capture probability of constituent atom is strongly influenced by the distribution of covalent electrons. The transfer probability from mesomolecular orbital to each atomic orbital is described by electronegativity. If a negatively charged particle is introduced instead of a localized electron on atom, it is regarded that they are captured in atomic orbitals directly. The capture ratio $A(Z_1/Z_2)$ for $Z_{1k}Z_{2l}$ compound is follows

$$A(Z_1/Z_2) = \frac{n_1 + \nu_1 \omega_1}{n_2 + \nu_2 \omega_2} \qquad (1\text{-}6)$$

where

$$\omega_1 = \frac{p_1 q_1}{p_1 q_1 + p_2 q_2} \qquad \omega_2 = \frac{p_2 q_2}{p_1 q_1 + p_2 q_2} = 1 - \omega_1$$

$$p_1 = \frac{1}{2}(1 - \sigma_1) \qquad p_2 = \frac{1}{2}(1 - \sigma_2) = 1 - p_1$$

$$q_1 = \frac{Z_1^2}{Z_1^2 + Z_2^2} \qquad q_2 = \frac{Z_2^2}{Z_1^2 + Z_2^2} = 1 - q_1$$

ν_1 and ν_2 are the valencies of the Z_1 and Z_2 atom in the compound, n_1 and n_2 are the numbers of localized electrons in Z_1 and Z_2 atoms that have small binding energy (<60 eV [23]). The covalent electron inclination is described by σ (in the equal balanced covalent binding, $\sigma = 0$). The parameter "q" means the radiative transition rate from the mesomolecular orbital to the mesoatomic orbital.

The LMM model well reproduces the experimental atomic capture ratio for oxide [24]. However, some deviations were found especially in low atomic number region [25]. Imanishi proposed the new q definition as follows [26].

$$q_1 = \frac{Z_{1\mathrm{eff}}}{Z_{1\mathrm{eff}} + Z_{2\mathrm{eff}}} \qquad q_2 = \frac{Z_{2\mathrm{eff}}}{Z_{1\mathrm{eff}} + Z_{2\mathrm{eff}}}$$

Z_{eff} means the number of effective electrons relate to particle transfer process from the mesomolecular orbital to the atomic orbital. In this model, a charged particle in mesomolecular orbital transfers to atomic Z orbital through Auger process. By reproducing the experimental results by this model, number of electrons related to muon capture can be estimated.

1.6 Previous studies for muon capture

Until now, many experiments had been performed and various empirical and/or theoretical models had been proposed to reveal the chemical effect for muon capture, however, the initial process of muonic atom formation and the initial state of the muon in muonic atom have never been cleared.

There are two major problems in the previous studies on the muonic atom formation process. 1) Muonic X-ray is influenced by sample density. Many previous experiments have been conducted by using dense samples like crystal and high pressure gases. In such conditions, the collisions between the muonic atom and other molecules occur competitively with muon cascade. Some electrons transfer from other molecule to the muonic atom during muon cascade by the collision (electron refilling). As a result, cascade path of the muon is influenced by refilling electrons, and the initial state of captured muon cannot be estimated from muonic X-rays. 2) Available information from muon cascade is limited. Although the muonic atom outputs many information during the muon cascade, such as Auger electrons, muonic X-rays, and the muonic atom itself (it becomes multivalent positively charged ion just after its formation), only muonic X-rays can be observed. There is the only one report for Auger electron measurement during muonic atom formation [10]. The observation of the muonic atom after its formation has never been reported, we have never konwn what kind of valencies (electric charge) the muonic atom has after formation.

1.6-1 Sample density effect for muonic X-ray

Electron refilling by collision with other atom and/or molecule during muon cascade makes it quite complicated [27-33]. As shown in Fig 1-6, the refilling electrons may change the de-excite path of a captured muon. Due to experimental easiness, many previous studies were performed by using high density materials (they were usually solid, liquid, and high pressure gases, consist of large atomic number elements) as muon capturing samples. Self-absorption of muonic X-ray is negligible and incident muons stop easily in high density samples. However, collisions between the muonic atom and other atoms and/or molecules frequent occur in this condition. As a result, muonic cascade paths are changed by refilling electrons and estimation for proper initial quantum state of captured muon become very difficult (almost impossible). The influence of sample density appears in muonic X-ray structure is known as density effect.

Both theoretically and experimentally, it is not reasonable to investigate chemical effect of muonic atom formation in the presence of the density effect. Many parameters, such as speed of muonic atom, mean free pass of muon, and cross section of electron refilling, have to be considered. Some researchers had tried to set speed of electron refilling as a parameter of muonic de-excitation, however, they couldn't discuss the quantitativeness for the density effect and chemical environmental effect each other, appearing in muonic X-ray structure.

On the other hand, an experiment to reveal the threshold of density effect was performed by using low pressure nitrogen oxides; NO, NO_2 and N_2O, as samples [34]. According to the result of this experiment, muonic X-ray structure (relative intensity ratio of K-series X-rays to K_α) is independent from sample density below 100 kPa for a two atomic molecule and 20 kPa for a three atomic molecule [34]. That is, in this condition, muonic atoms can be regarded as isolated state during its de-exitation.

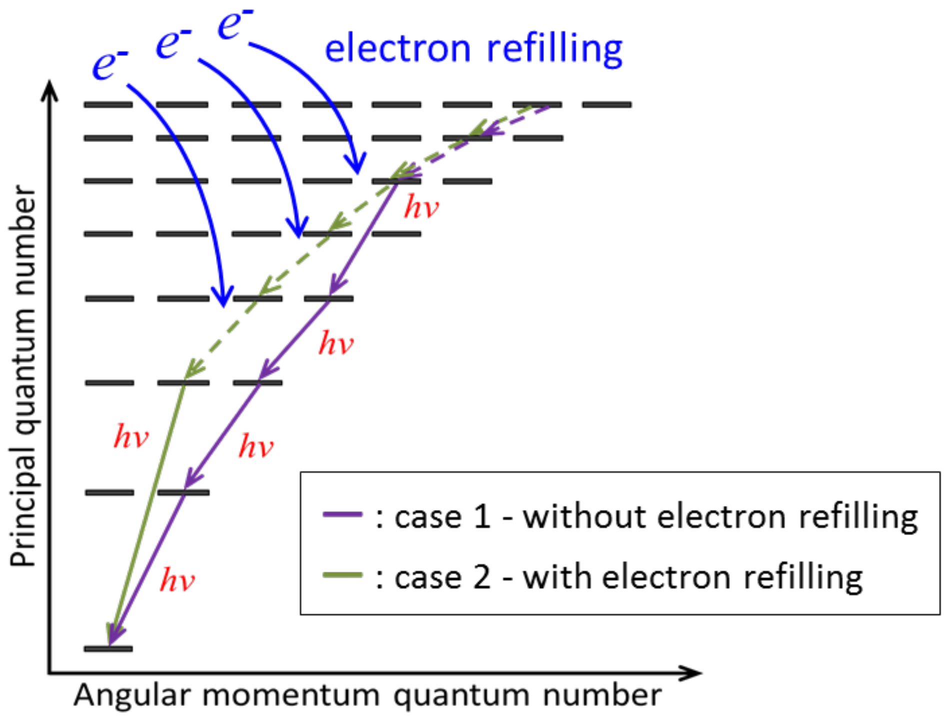

Fig. 1-6 Schematic view of electron refilling during muonic de-excitation. Auger processes in muonic de-excitation are easily provoked by refilling electrons. As a result, muonic X-ray emitting pattern is changed.

Performing the muon capture experiment at the isolated system, it may reveal the chemical effect in muon transfer process. It is generally believed that no chemical effect is appeared in the muon transfer from muonic hydrogen to other atom. Because, a transferred muon enters in a deeper atomic muon's level of accepter atom, the muon cannot interact with orbital electrons in outer shell.

On the other hand, some experimental results which suggest existence of the chemical effect of pion transfer in organic compounds were reported [35-38]. The large difference of pion capture compared with muon capture is the fact that the captured pion don’t reach the 1s state in its de-excitation. As mentioned above, a pion in pionic hydrogen atom is captured by a proton and immediately decays to photons. Whereas pions transfer from only pionic excited state ($n \geq 2$) of pionic hydrogen atom, muons transfer from both excited state and ground (1s) state of muonic hydrogen atom. If de-excitation rate of a muon in muonic hydrogen atom is enough faster than collision frequency (can be regarded as an isolated state), muon transfer from 1s state only occurs.

In this way, though there are various discussions about the chemical environmental effect of muon transfer process, comprehensive discussion has never been conducted yet and the existence of chemical environmental effect in muon transfer process is still vailed in mystery.

1.6-2 The information from muon cascade and initial state of the muon

As mentiond, the muon interacts with an atomic electron having weak binding energy (it suppoed below 100 eV) and then creates own orbital around the nucleus. Especially, initial process of muonic atom formation is quite interesting from the view point of chemistry, but the muonic atom after formation has never been measured directly. Currently, only the muonic X-ray gives information about it (by using cascade calculation [11]), though the muonic atom also outputs the information as Auger electrons and muonic atom ion after its formation.

If the observation of muonic atom becomes possible combining with the observation of muonic X-rays and Auger electrons, the muonic atom formation process can be understood more deeply. For example, the charge of the muonic atom just after its formation can be determind precisely by both Auger electron measurement and muonic atom measurement. It will also support the results of muonic X-ray measurement performed previously.

Once the muonic atom is formed, it becomes multivalent positively charged ion immediately due to Auger electron emission. So, the muonic atoms after formation may be attracted by electric fields and magnetic fields.

1.7 Aim of this work

The fInal goal of this study is the revealing muonic atom formation process comprehensively. For this purpose, two major aims were set in this thesis.

The first aim is the investigation of chemical environmental effect of muonic atom formation by measuring muonic X-rays which are emitted at the muonic atom formation. Here, two ways of muonic atom formation process; both direct muon capture by an atom and muon transfer from muonic hydrogen atom, are set as the research target. For the first aim, especially the following experimental conditions were focused; simple structure molecules which consist of carbon, oxygen and sulfur atoms, and low pressure gaseous sample. Using these samples, it is considered that the relation between the electron arrangement around constituent atom and the muon capture process can be discussed in detail. The muon capture ratio and the initial state of captured muon were derived from these samples, and the difference from the chemical environment was discussed.

The second aim is the verifying the charge behavior of muonic atom just after its formation, by extracting the recoiled muonic atom ion and observing it. The extraction of the muonic fluorine atom from PTFE target was planned, and the experimental system was developed, as a first step for the seconed aim. Combining with this study and the muonic X-ray measurement, we can more deeply understand for muonic atom formation.

This thesis is composed of the following chapters. Accelerator facility (J-PARC) where all muon irradiation experiments were performed is described in Chapter 2. The facility provides the world highest intensity pulsed muon beam. In Chapter 3, experimental results of muon irradiation for simple structure gaseous samples (CO, CO_2, COS and CS_2) and hydrogen containing system (H_2+CO, H_2+CO_2, H_2+COS and H_2+CS_2) are described. Discussion about muon capture probavirity for constituent atoms and initial quantum states of captured muon are also described. In Chapter 4, development and assessment of the muonic atom extraction system for verifying charge behavior of the muonic atom just after its formation are described. Concluding remarks of this thesis are described in Chapter 5.

Chapter2. Accelerator Facility

In this chapter, the accelerator facility where were performed muon beam irradiations is described. All experiments for muonic atoms were performed at the MUSE D1-prot in MLF, J-PARC, Japan, as the visiting researcher. The beam time of each work was June 2012 (2012A0039), March 2013 (2012B0103), May 2014 (2014A0204), April 2016 (2015A0192), June 2016 (2015A0237) and December 2016 (2016A0295).

2.1 About accelerator facility

2.1-1 Accelerator facility: J-PARC

J-PARC (Japan Proton Accelerator Research Complex) is a high intensity and high energy proton accelerator facility is located at the Tokai, Ibaraki, Japan. The J-PARC provides high intensity secondary beams of muons, neutrons, hadrons, and neutrinos, from primary proton beams.

The J-PARC consistes of three proton accelerators: a 400 MeV linear accelerator (LINAC: operating at 180 MeV in 2016), a 3 GeV rapid-cycling synchrotron (RCS) and a 50 GeV (30 GeV in 2016) main ring (MR).

The proton beams which are accelerated by the LINAC are provided to both the RCS and the MR to product secondary particles. In normal operation mode, over 90% of the protons accelerated in the RCS are directed to the muon and neutron production targets in the Materials and Life Science Experimental Facility (MLF). The remaining protons are transported to the MR for further acceleration before being extracted via one of two MR extraction ports. In each case, target materials and designs are employed to maximize the efficient production of the desired secondary particle beam (©2014 J-PARC Center. [39]).

All muon experiments written in this thesis were performed in the Materials and Life Science Experimental Facility.

Table 2-1 Specification of accelerators in J-PARC (at Novemver 2014) [40].

	LINAC	RCS	MR
Extraction Beam Energy	400 Mev	3 GeV	30 GeV
Repetition	40ms (25 Hz)	40ms (25 Hz)	2.5 - 6.0s
Average Beam Current	30 mA x 500 μs	90 μA(Average)	8 μA(Average)
Average Beam Power	Maximum 130 kW	300 kW	240 kW

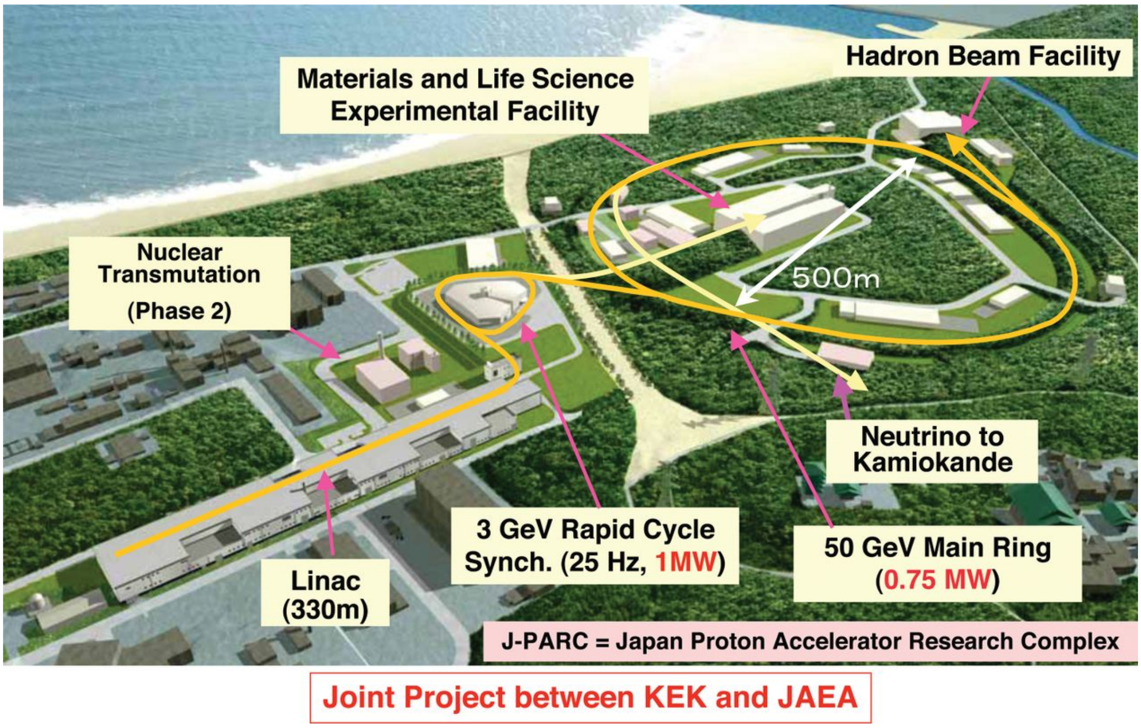

Fig. 2-1 Bird's-eye view of the entire facility of J-PARC [40].

2.1-2 Muon experimental facility: MLF MUSE

The MLF (Materials and Life Science Experimental Facility) is experimental facility for materials science and life science researches using high intensity muon and neutron beam. The MLF has 7 muon port (5 lines have been under construction, two beam lines; D1 and D2 in Fig. 2-2, are available currently) and 21 neutron beam ports (1 line has been under construction, 20 lines are available currently). The Muon experimental area in the MLF is called Muon Science Establishment: MUSE [41,42]. Muons and neutrons are produced by primary proton beams (3 GeV, 333 μA at the maximum, and a repetition rate of 25 Hz). The source of muons and neutrons are located on the proton beam axis as shown in Fig. 2-2. As muon source, the rotating muon target made from graphite [43] (Fig. 2-3) has been installed since 2015, before that, the static target made from graphite (Fig. 2-4) had been used.

The proton beams from the RCS enters muon target then various secondary particles such as neutron, electron and pion are generated by nuclear reaction. In the D-line, pions are selectively conducted by a focusing triplet quadrupole magnet and a bending magnet system with separating pion momentum, and injected in a solenoid magnet. The pions completely decay; two-body decaying into muon and muon neutrino, on the way of their trip due to very short life of pion (26 ns). The backward decay muons produced from the pions are transported by using triplet quadrupole magnets and bending magnets systems, and are extracted as particle beams to beam port (experimental area). The layout drawing of magnets arrangement of the muon beam line (D-Line) is described in Fig. 2-5. Details and specifications of D-Line components are written in elsewhere [44].

The Muon beam is available as pulsed form depending on the primary proton beam in the MUSE. In the J-PARC, double bunched muon beams have been available in normal operation mode. Since 2015, property of muon beam had changed from double bunched to single bunched, because of change of upstream proton beam operation. The detail of muon beam in the MUSE is described in chapter 2-2.1.

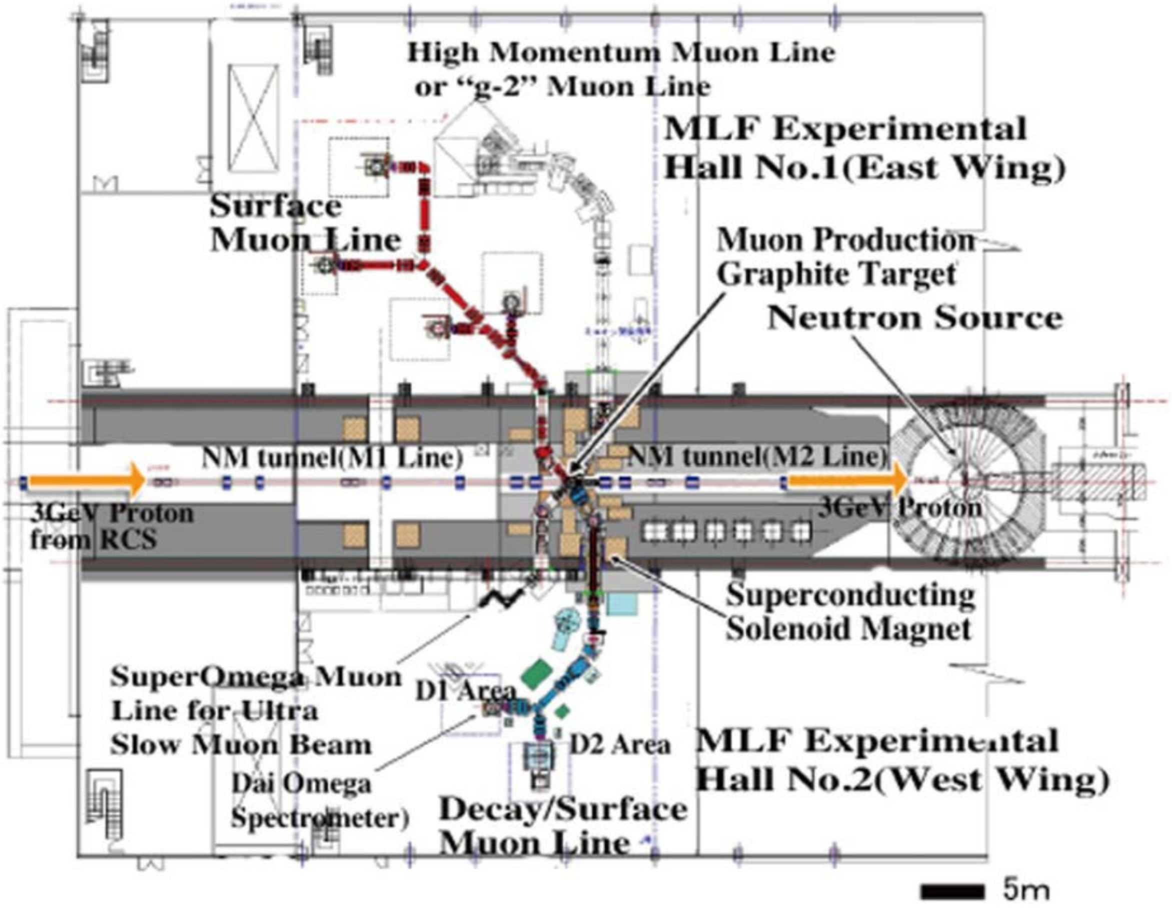

Fig. 2-2 Schematic drawing of the MUSE facility located on the first floor of the MLF building [41].

Fig. 2-3 Rotating muon target in the MUSE facility; installed in 2015 [43].

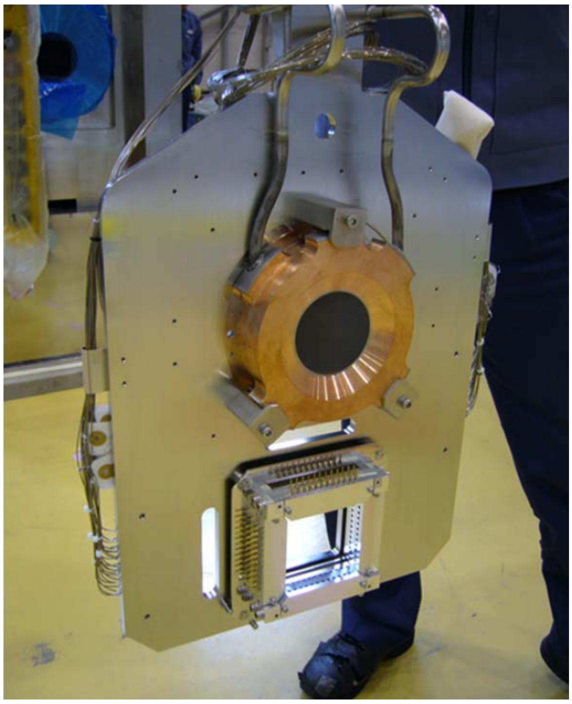

Fig. 2-4 Graphite target for muon generation in the MUSE facility [41]. It had been used until 2014. A graphite disk is fit into a copper frame for edge cooling. A beam profile monitor is seen underneath the graphite target.

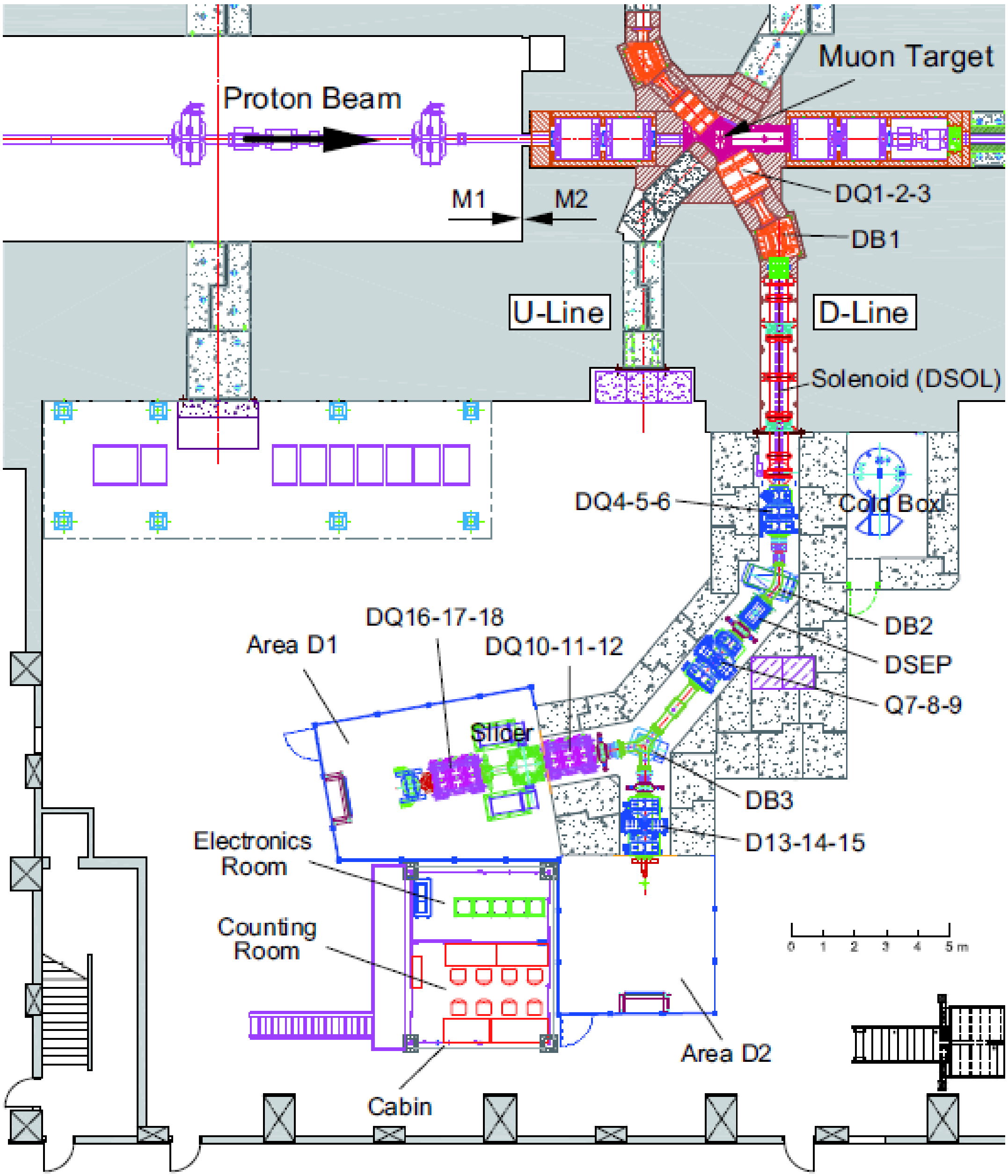

Fig. 2-5 Layout of the D-Line components in the MUSE [44].

2.2 About experimental setup

2.2-1 Property of muon beam available in the MUSE

In the MUSE, the muon beam is available as single pulsed time structure of 100 ns width (FWHM) with 25 Hz repetition rate, and 150 kW power, currently (Fig 2-6). The experiment proposal number 2014A0197, 2015A0237 and 2016A0295 were performed by using single bunched beam. In this condition, approximately 10^4 muons whose momentum 20 MeV/c are available per second.

Before 2014, the muon beam had a double-pulsed time structure of 100 ns width, separated by 600 ns with a repetition rate of 25 Hz (Fig 2-7). The experiment proposal number 2012A0039 and 2012B0103 were performed by using double bunched beam. In this condition, approximately 10^3 muons whose momentum 20 MeV/c are available per second.

Positively charged muon beam is also available in the MUSE, it is mainly used for muon spin resonance (μSR) method to investigate magnetic property of various materials. Details of muon beam available in the MUSE are summarized in Table 2-2 [45].

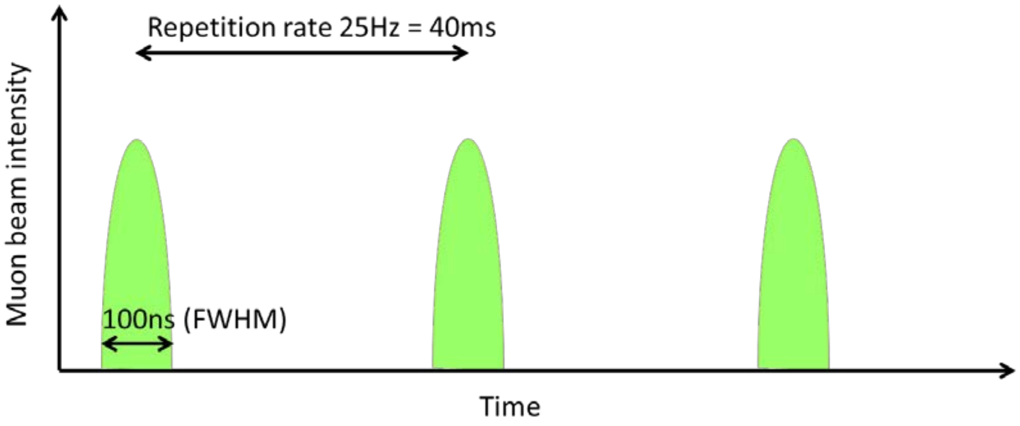

Fig. 2-5 Schmatic view of single pulsed muon beam (Current sepc.).

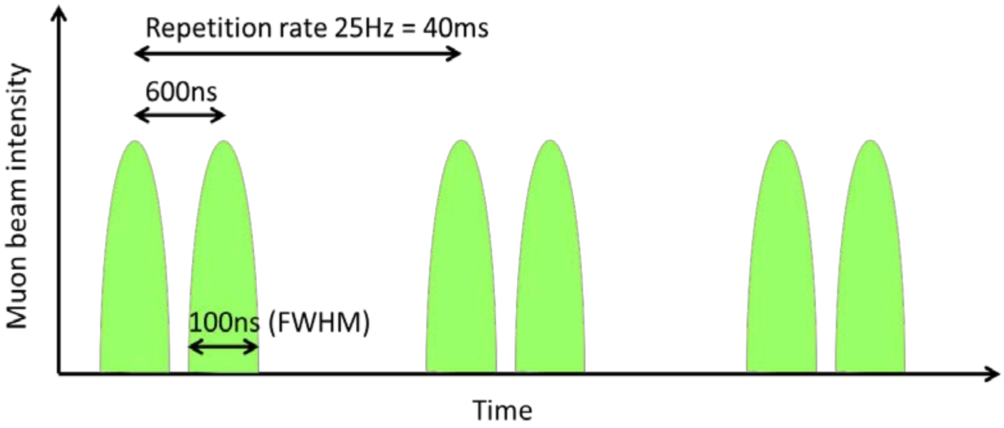

Fig. 2-6 Schmatic view of double pulsed muon beam (~2014).

Table 2-2 Specification of accelerators in J-PARC (at Novemver 2014) [45].

	Surface Muon: μ^+	Decay Muon: μ^+, μ^-
Beam Energy	4.1 MeV	5-50 MeV
Depth	～0.2 μ	1mm-～cm
Energy Distribution	～15%	～15%
Pulse Width	～100 ns	～100 ns
Beam Size	30 mm × 40 mm	70 mm × 70 mm
Beam Intensity	3×10^7 s^{-1}	10^{6-7} s^{-1}
Number of Ports	2	2

2.2-2 Outline of muon beam experimental area

As mentioned, the Muon facility in the MLF has two beam lines one is “D1”, the other is “D2” currently (Fig. 2-5).

The D1-area is designed for μSR spectrometry and has the plastic scintillators for detecting electrons from muon decay, the electromagnet system for generating high magnetic field, and the correction magnets for geomagnetism [46]. A time distribution of decay electrons can be measured by using this spectrometer, that is time resolved emission spectrum can be obtained. Over view of the D1 experimental area and the μSR spectrometer are shown in Fig. 2-7. The μSR spectrometer can be installed a cryostat at the upside hole of spectrometer.

The D2-area is open geometry for general purpose experimrnts (Fig. 2-8). Users can install individual experimental equipments for muon beam irradiaton. Non-destructive element analysis by measument of muonic X-ray, elementary particle physics, nuclear muon capture, and various type experiments have been performed in the D2 area.

In this thesis, muon irradiation for gas samples (2012A0039, 2012B0103, and 2014A0204) were performed in the D1 area, and muonic atom beam extraction experiments (2015A0237 and 2016A0295) were performed in the D2 area, respectively.

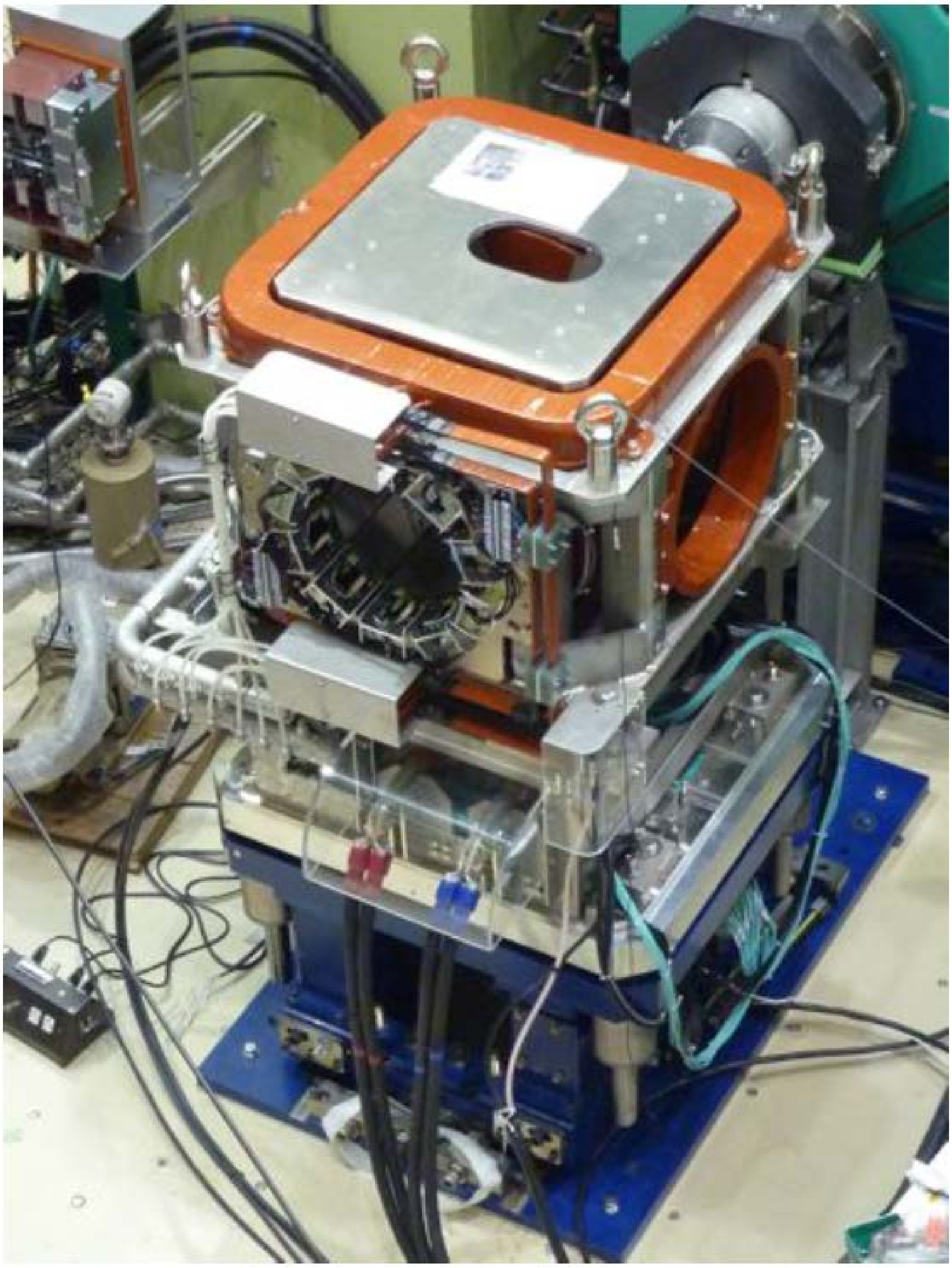

Fig. 2-7 Full view of the D1 spectrometer and beam port [46].

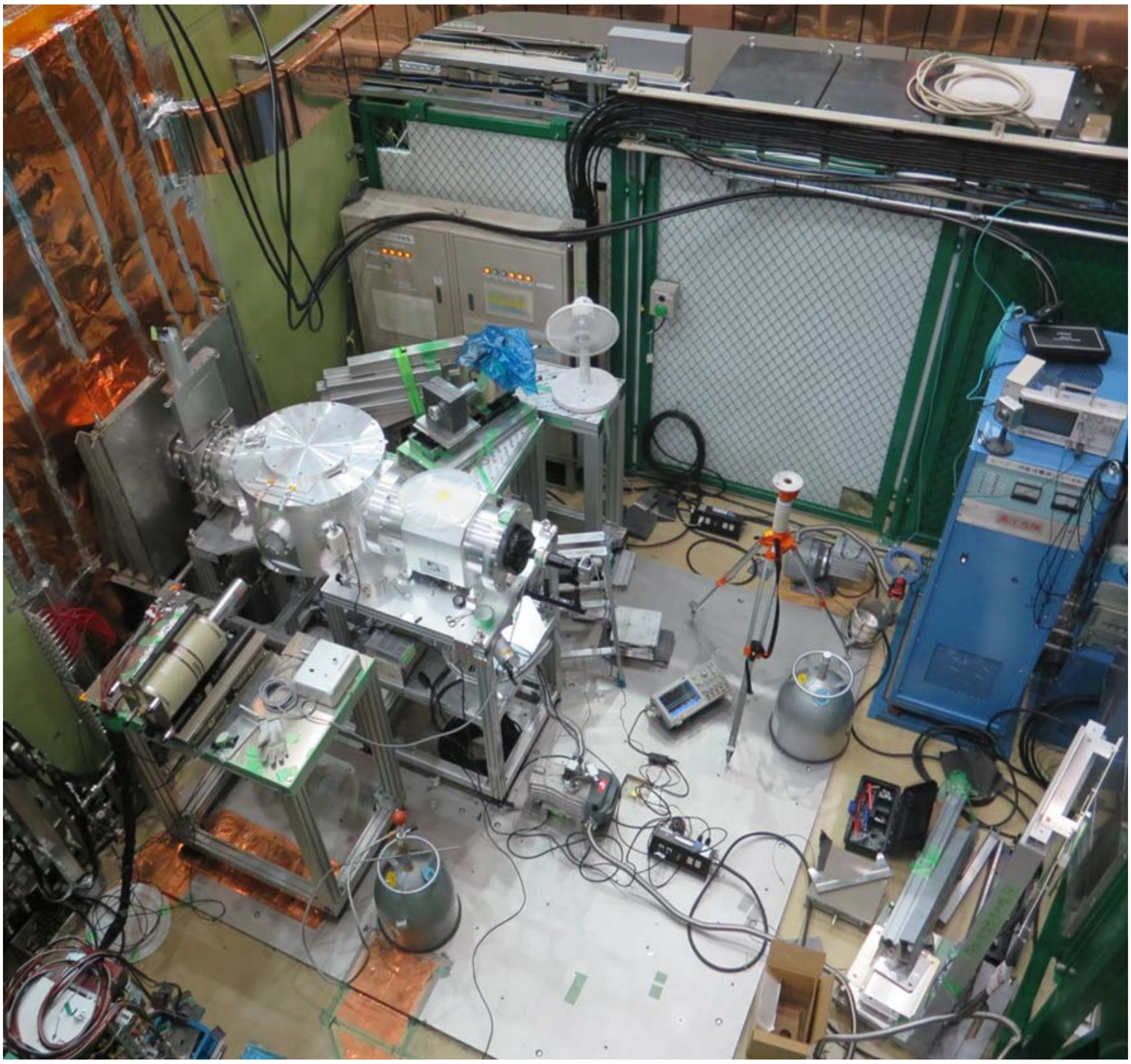

Fig. 2-8 Overview of the D2 area, in this picture, the experimental set up for non-destructive element analysis was installed.

Chapter3. Muon capture experiment for gaseous samples; CO, CO_2, COS and CS_2

The muon irradiation experiments for pure gas samples; CO, CO_2, COS, and CS_2, and hydrogen mixed gas samples; H_2+CO, H_2+CO_2, H_2+COS, and H_2+CS_2, were performed to investigate chemical effect on muon capture and muonic atom formation in detail. In this chapter, results and disucussions from these experiments were described.

The strategy of this study is described in 3-1. The experimental procedure, method of the analysis, results and discussion about muon experiment are described in 3-2. Muonic X-ray spectra of each sample and peak assignment result are described in 3-3. Muon capture ratio deduced from muon capture numbers of carbon, oxygen, and sulfur atom are described in section 3-4. Discussions for muon capture ratio were described in 3-5. In this section, number of electrons contribute to muon capture probability of atom were estimated by LMM model. Muonic X-ray structure; emission pattern of muonic X-rays from carbon, oxygen, and sulfur atoms, are described in 3-6. Discussions for initial quantum state of captured muon were described in 3-7. Discussions for influence of lone pair electrons on carbon atom in CO molecule are described in 3-8. Discussions for chemical environmental effect on muon capture for H_2+CO and H_2+CO_2 system were described in 3-9. It was revealed that, muons transferred from a muonic hydrogen atom behave differently from the muons directly captured by an atom.

3.1 Strategy for this study

As mentioned, simple structure and low density samples which can be regarded as isolated state during muon cascade, is necessary to investigate chemical effect on muonic atom formation. From the fact, the following experimental conditions were proposed to investigate chemical effect on muonic atom formation, as reasonable way.

i. Sample consists of light element and has simple structure
ii. Sample is low pressure gas at muon beam irradiation

To deliver the muon experiment in above conditions, the low pressure gaseous molecules consist of only carbon, oxygen, and sulfur atom; 10 kPa ~ 40 kPa of CO, CO_2, COS, and CS_2, were chosen as muon irradiation samples. This system has some unique features. While samples have different molecular structures each other, they have same components. It is expected that experimental results from these molecules are easy to compare because they consist of same atom and have same structure. Geometrical differences are almost negligible, because they don't have bending structure and/or chemical resonance. It is difficult to evaluate the effect of geometrical difference for muonic atom formation precisely. For CO_2, COS and CS_2, valence electron arrangement is same among three molecules, but a sulfur atom is 1.6 times larger than an oxygen atom. Comparing muonic X-rays from three molecules, the information of inner shell electron and the influence of size of atom on muon capture process may become clear.

To perform muon experiments under the quite low density sample condition, the ultra-low energy muon beam at J-PARC MUSE [41,42] had been developed. Using this beam, we can stop muon beam properly even if in a very thin sample.

In addition, to reveal the existence of chemical effect in muon transfer process, muon irradiation experiment for hydrogen mixture gaseous sample; H_2+CO, H_2+CO_2, H_2+COS and H_2+CS_2 under the conditions for the isolated state were performed.

3.2 Experimental

3.2-1 Experimental setup

The experimental setup was established in D1 experimental area as shown in Fig. 3-1. A gas chamber which contains sample gases was installed at the center of the μSR spectrometer (both upstream side and downstream side of 2π plastic scintillators). Gas chamber is made from aluminum, diameter of chamber is 100 mm and length is 580 mm, it is approximately 7L inner volume (shown in Fig. 3-2). The chamber has four windows, one (50 μm thickness of poly-imide film) directs to axial side (upstream side of muon beam) is for entrance of muon beam, other three (75 μm thickness of poly-imide films, or 100 μm thickness of aluminum films) direct to radius side are for measurement of muonic X-rays from samples. Sample gas exchange system is installed at the downstream side of the chamber, it consists of stainless steel tubes (swagelok), valves, gas cylinde with regulator, and pressure gauge (0.02 ~ 200 kPa).

The muon beam was irradiated to the chamber and the muonic X-rays were measured by two to three germanium detectors. Some blocks and sheets made from lead and/or tin were set as radiation shield.

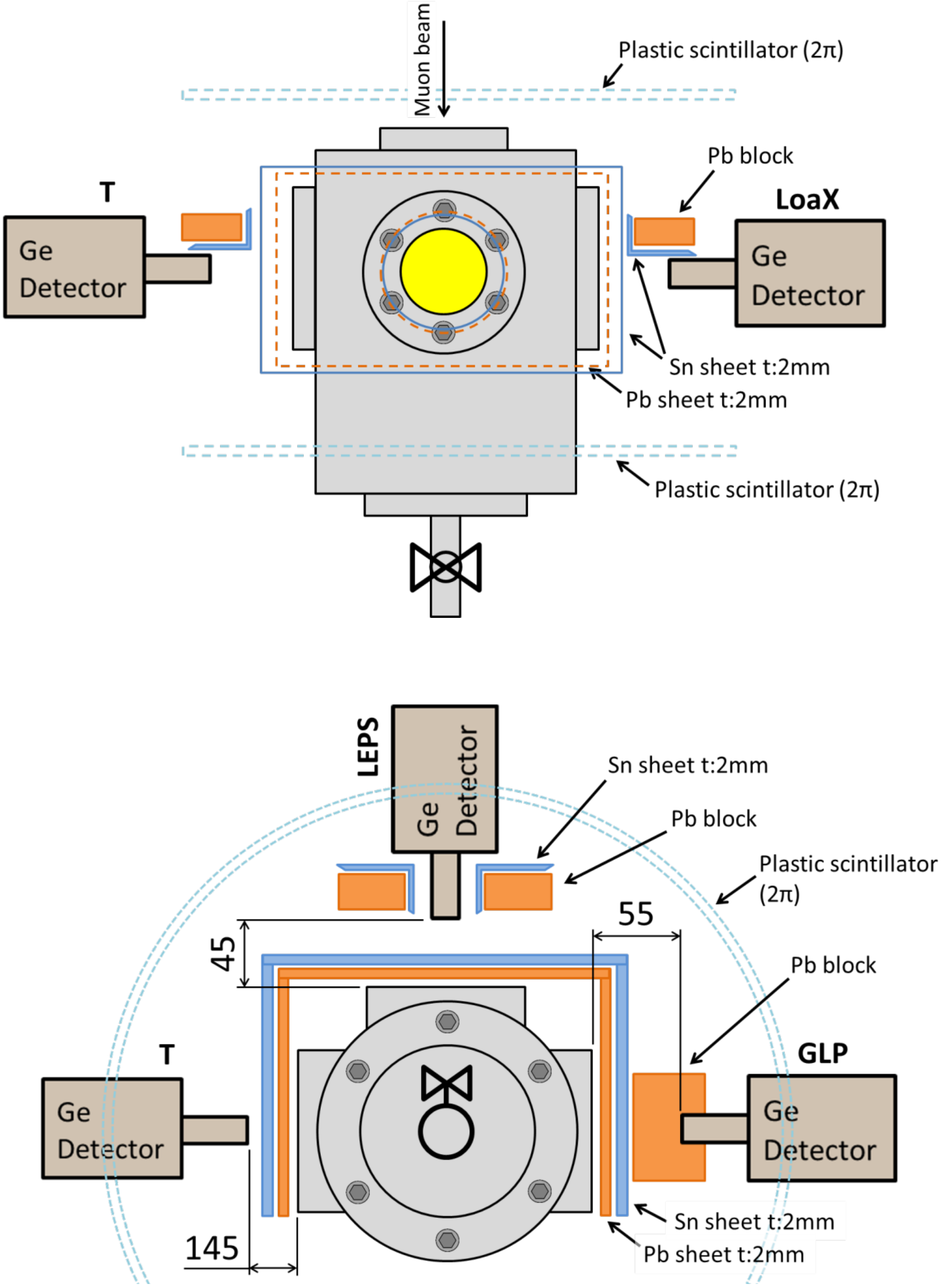

Fig. 3-1 Schematic view of experimental setup (Top: plan view, Bottom: flont view).

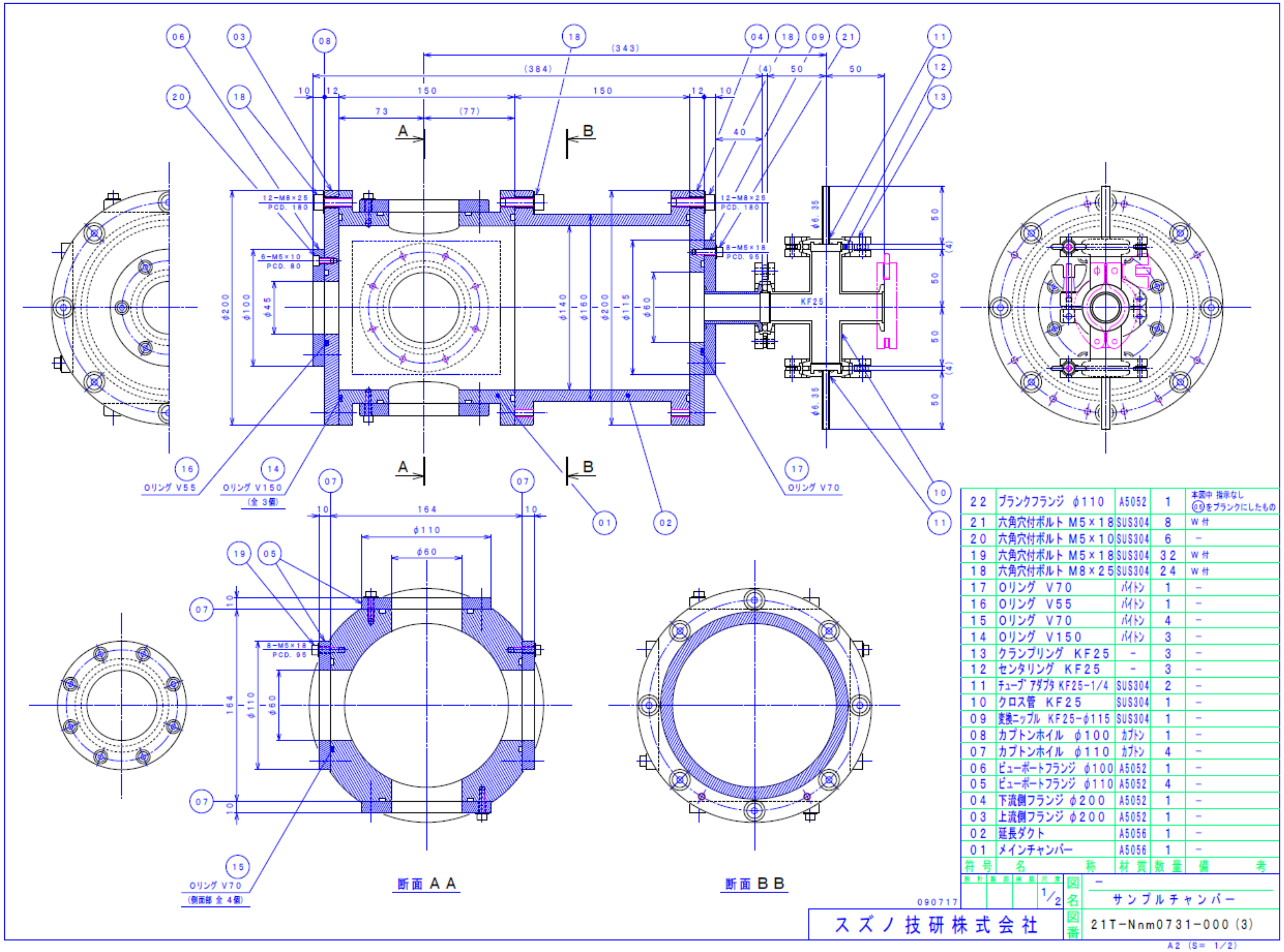

符号	名称	材質	数量	備考
22	ブランクフランジ φ110	A5052	1	本図中 指示なし ⑤をブランクにしたもの
21	六角穴付ボルト M5×18	SUS304	8	W 付
20	六角穴付ボルト M5×10	SUS304	6	−
19	六角穴付ボルト M5×18	SUS304	32	W 付
18	六角穴付ボルト M8×25	SUS304	24	W 付
17	Oリング V70	バイトン	1	−
16	Oリング V55	バイトン	1	−
15	Oリング V70	バイトン	4	−
14	Oリング V150	バイトン	3	−
13	クランプリング KF25	−	3	−
12	センタリング KF25	−	3	−
11	チューブアダプタ KF25−1/4	SUS304	2	−
10	クロス管 KF25	SUS304	1	−
09	変換ニップル KF25−φ115	SUS304	1	−
08	カプトンホイル φ100	カプトン	1	−
07	カプトンホイル φ110	カプトン	4	−
06	ビューポートフランジ φ100	A5052	1	−
05	ビューポートフランジ φ110	A5052	4	−
04	下流側フランジ φ200	A5052	1	−
03	上流側フランジ φ200	A5052	1	−
02	延長ダクト		A5056	1	−
01	メインチャンバー	A5056	1	−

Fig. 3-2 Drawing of the gas chamber.

3.2-2 Germanium semiconductor detectors

In all experiments, Germanium semiconductor detectors described in Table 3-1 were used for muonic X-ray measurement. They are portable detectors and designed for low-energy photon measurement. Because the energies of muonc oxygen and muonic carbon X-ray are in low energy region (around 100 keV), these low energy type detectors are suitable for this study. As a matter of convenience, the detectors were numbered as det-1 ~ det-5 respectively.

Table 3-1 Germanium semiconductor detectors for muonic X-ray measurement, window is made from Berilium for det-1, 2, 3, and 5, window material of det-4 is Carbon.

Detector number		det-1	det-2	det-3	det-4	det-5
Supplier		ORTEC	CANBERRA	ORTEC	CANBERRA	ORTEC
Model		LoaX 36300/15-P-S	GL0515	GLP-16195/10-P-S	BE2020	GLP-36360/13P4
Germanium crystal	diameter	35.9 mm	25.2 mm	16.0 mm	51.5 mm	36.0 mm
	thickness	14.0 mm	15.0 mm	10.0 mm	20.8 mm	13.0 mm
	type	Co-axial	Planer	Planer	Planer	Planer
Resolution		300 eV at 5.9 keV 585 eV at 122keV	250 eV at 5.9 keV 550 eV at 122keV	195 eV at 5.9 keV 495 eV at 122keV	350 eV at 5.9 keV 650 eV at 122keV	360 eV at 5.9 keV 585 eV at 122keV
Window thickness		0.5 mm (Be)	0.15 mm (Be)	0.127 mm (Be)	0.6 mm (C)	0.254 mm (Be)

3.2-3 Sample gases and gas exchange system

Simple molecule compounds consist of carbon, oxygen, and sulfur were used as muon irradiation samples. Pure gas samples described in Table 3-2 were used in experiments for investigating muon capture process to sample molecule directly. Hydrogen containing samples described in Table 3-3 were used in experiments for investigating muon transfer process from muonic hydrogen atom to sample molecule. Each of the experiments was performed at different periods described in Table 3-2 and 3-3.

Sample gases were inlet to the gas chamber by sample exchange system described in Fig. 3-3. It consists of stainless steel tubes (swagelok), valves, gas cylinde with regulator, pressure gauge (0.02 ~ 200 kPa), and vacuum pump. Sample gas handling is performed in following procedures. First, all components were vacuumed to 10^0 Pa, sample gas was inlet to the chamber, all components were vacuumed again to 10^0 Pa, and finally, sample gas was inlet to the chamber at appropriate pressure. CS_2; liquid at room temperature, was vaporized by vacuuming and introduced to the chamber gaseous form. Hydrogen mixture samples were purchased as pre-mixed gas cylinders (H_2+CO and H_2+CO_2), but H_2+COS and H_2+CS_2 were mixed manually while reading the pressure gauge. Gas temperature was monitored by temperature sensor attached on outside of the chamber.

Table 3-2 Specification of accelerators in J-PARC (at Novemver 2014).

Ssample	Pressure	Irradiation time	Period	Experiment No.	Detectors
CO (99.99%)	40 kPa	16.0 h	Jun. 2012	2012A0039	1, 2
CO_2 (99.99%)	20 kPa	9.1 h	Jun. 2012	2012A0039	1, 2
COS (99.99%)	18 kPa	24.8 h	Jun. 2012	2012A0039	1, 2
	10 kPa	29.5 h	Feb. 2013	2012B0103	1, 2
CS_2	20 kPa	14.3 h	Apr. 2016	2015A0192	2, 4, 5

Table 3-3 Specification of accelerators in J-PARC (at Novemver 2014).

Ssample	Pressure	Irradiation time	Period	Experiment No.	Detectors
H_2+CO (1.000%)	99 kPa	8.9 h	Mar. 2014	2014A0204	2, 3, 4
	50 kPa	11.0 h	Mar. 2014	2014A0204	2, 3, 4
H_2+CO_2 (1.025%)	99 kPa	9.4 h	Mar. 2014	2014A0204	2, 3, 4
	50 kPa	13.0 h	Mar. 2014	2014A0204	2, 3, 4
H_2+COS (1%)	99 kPa	9.0 h	Apr. 2016	2015A0192	2, 4, 5
H_2+CS_2 (1%)	99 kPa	9.0 h	Apr. 2016	2015A0192	2, 4, 5

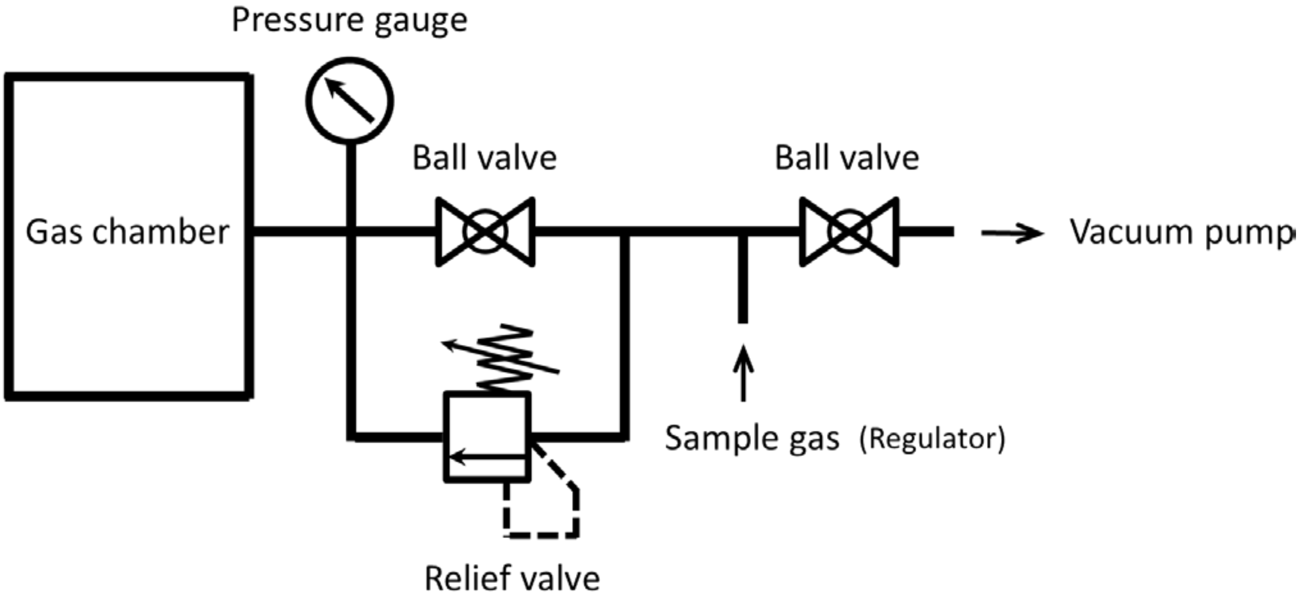

Fig. 3-3 Schematic view of gas handling (exchange) system.

3.2-4 Data acquisition system and circuit configuration

In the MUSE, muonic X-ray spectra can be obtained by using the data acquisition system (DAQ) consists of NIKI-GLASS A3300, and NIM circuits shown in Fig. 3-4. In 2015, DAO system had changed from CAMAC (Computer Automated Measurement And Control) to current system. Whereas, CAMAC system was operated in experiments for 2012A0039, 2012B0103, and 2014A0204, current system was operated in experiments for 2015A0192. Previous DAQ system is described in Fig. 3-5.

In all experiments, signals from germanium detector which coincident with accelerator operation were selectively measured. In addition, all signals were measured by list-mode (event by event mode), that is, all of obtained data have individual information both energy and timing. A detector outputs two same signal attributed to muonic X-ray injection, one was treated as an energy signal and conducted to spectroscopy amplifier (S. AMP), and the other was treated as a timing signal. Timing signals from detector were amplified by fast filter amplifier (F. AMP), then, separated from low-amplitude noises by constant fraction discriminator (CFD). Signal from fast filter amplifier is divided to two directions, one goes to TDC and recorded as timing information, the other goes to gate generator. Gate generator creates a timing gate signal width of 20μs, and this signal and a signal from spectroscopy amplifier (energy signal) are taken coincidence. Signal from spectroscopy amplifier can only goes to ADC and recorded as energy information, in the case of coincident with gate signal.

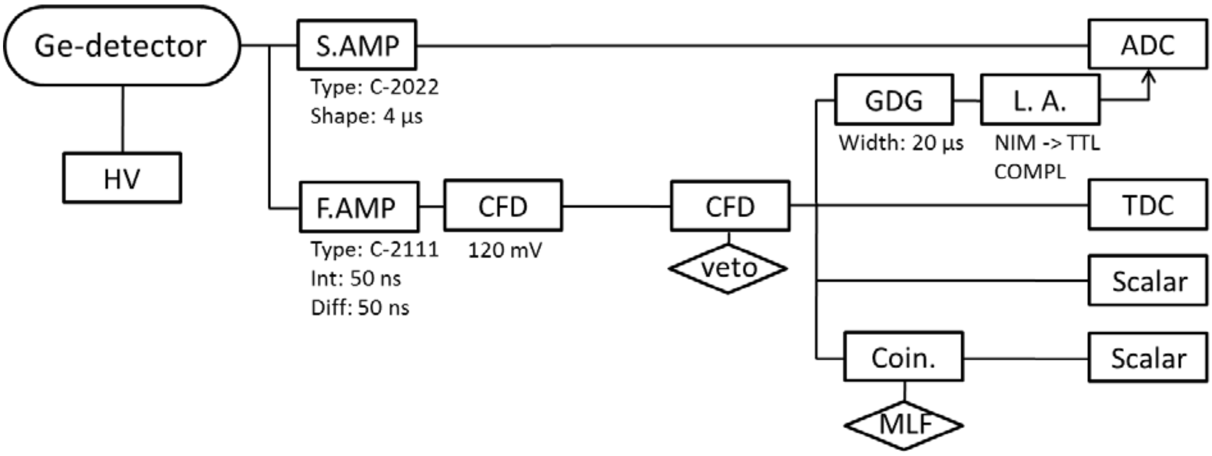

Fig. 3-4 Data acquisition system: DAQ in MLF (before 2014).

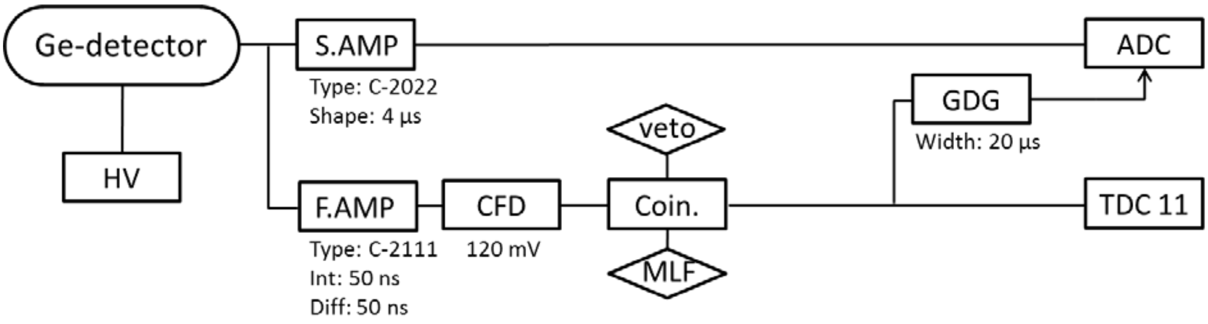

Fig. 3-5 Data acquisition system: DAQ in MLF (After 2015).

3.3 Result I: Muonic X-ray spectrum

3.3-1 Muonic X-ray spectra obtained from list mode measurement

The muonic X-ray spectra were obtained by list mode measurement, that is, each data which constitutes spectrum has both the time information and the energy information. Therefore, both histograms intensity/energy (ADC) and intensity/time (TDC) can be created from the measurement spectrum. As representative, ADC and TDC histograms created by the muonic X-ray spectrum of 55 kPa of neon samples are shown in Fig. 3-6.

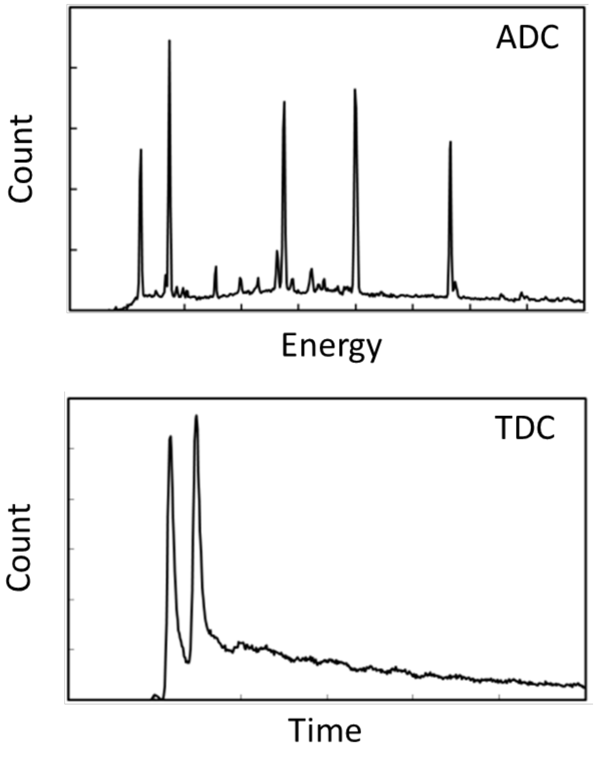

Fig. 3-6 Muonic X-ray spectrum of Ne, 55 kPa condition measured by detector 1, ADC: energy histogram (top), TDC: time resolved emission histgram (bottom).

3.3-2 Signal improvement of measured spectrum (noise reduction)

Since the signals attributed to muonic X-ray coincident with the timing of muon beam pulse, improvement of S/N is possible by extracting the signals which are coincident with the muon beam and creating the spectrum. In other word, background noises can be reduced significantly by this method. For example, signal improvement (background noise reduction) procedure of 55 kPa of neon sample, and the comparison of before /after improvement are shown in Fig. 3-7 and 3.8 respectively. In this figure, at first, TDC histogram is created by the peak region of muonic x-ray of μNe(3-2), then the TDC histogram which is reflected only the data from μNe(3-2) is created. From the TDC histogram, ADC histogram can be reproduced and background noises are significantly reduced, but signal intensity is not reduced.

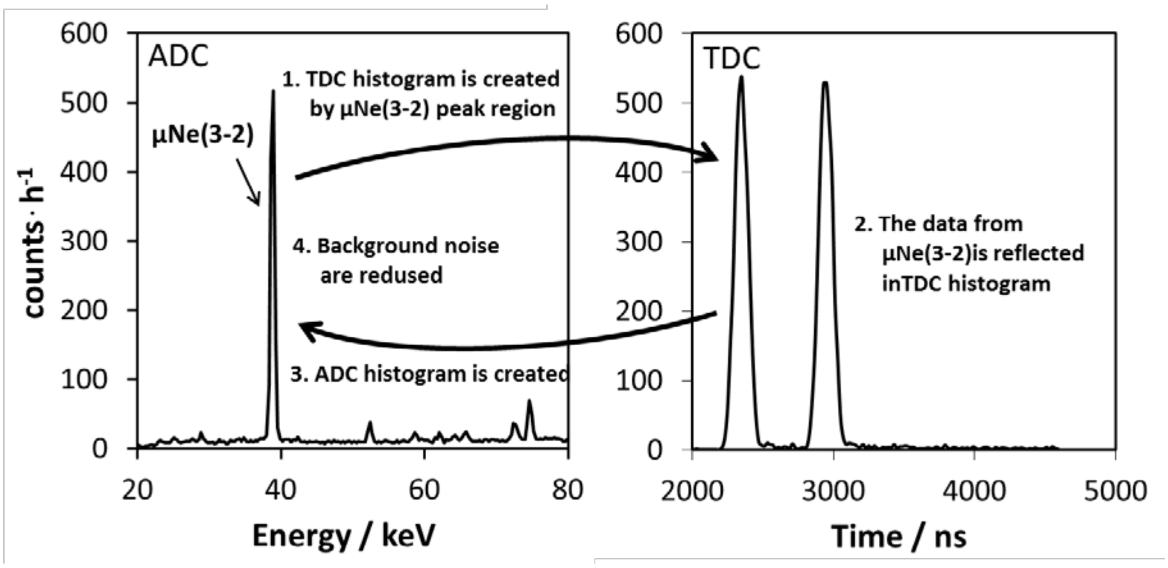

Fig. 3-7 signal improvement (background noise reduction) procedure in measurement spectrum for 55 kPa of neon sample.

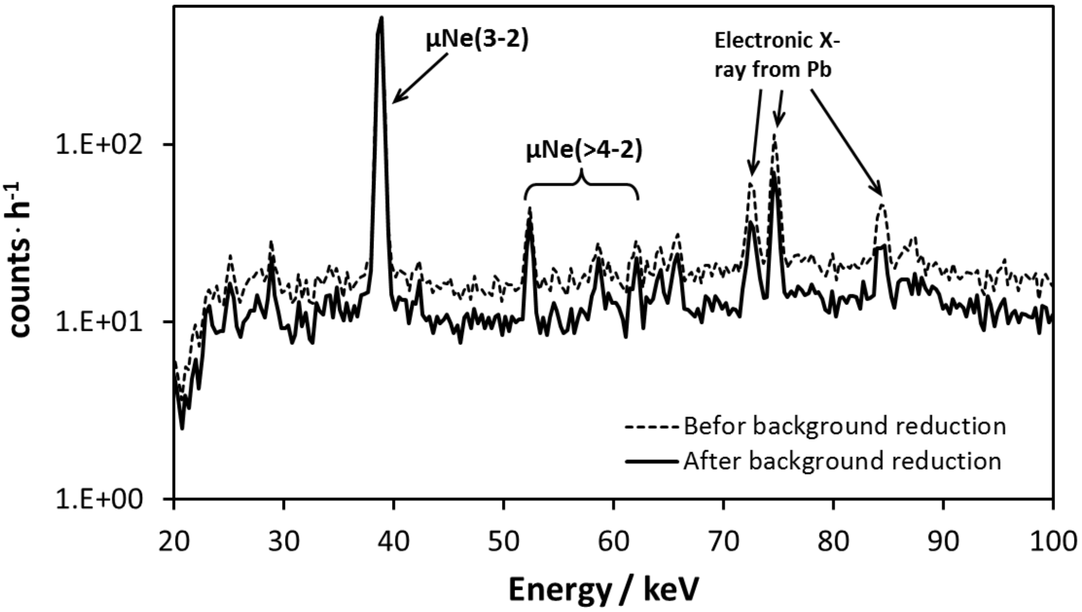

Fig. 3-8 The comparison of before /after signal improvement (background noise reduction).

3.3-3 Detection efficiency of germanium semiconductor detectors

The detection efficiencies of the germanium semiconductor detectors used in the experiment were determined by Monte Carlo simulation (EGS-5 code) [47]. As shown in Fig. 3-9, the calculation was conducted in the condition which is reproduced geometrical layout of the experiment. Specifically, under the condition that the muon beam of the same momentum as the experiment (18.8 MeV / c ± 5%) was irradiated into the gas chamber filled with gas samples, and the muon stop position distribution was estimated. It is assumed that muonic X-rays are discharge from each stop position of the muon. By using this calculation, the detection efficiency of each muonic X-ray energy identified by spectrum analysis were determined, shown in Fig. 3-10.

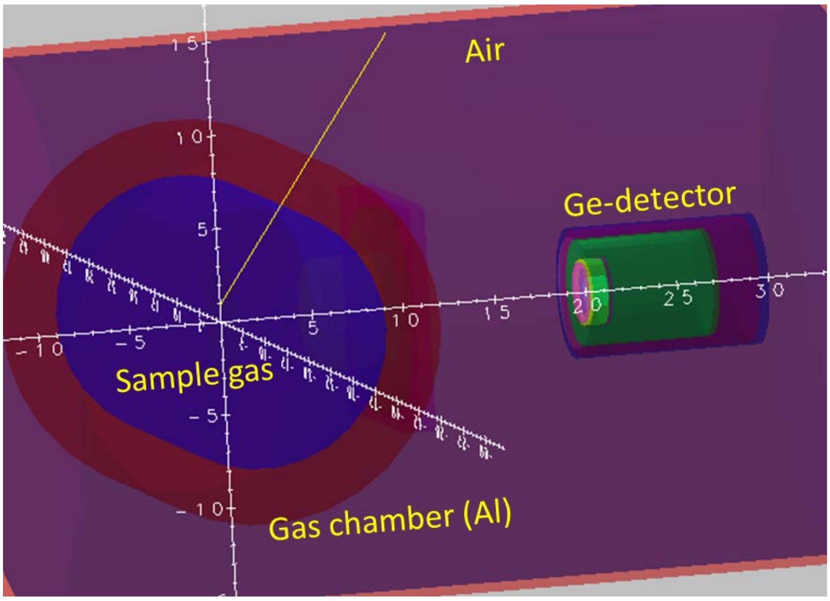

Fig.3-9 Geometrical relations of each component in EGS-5 calculation.

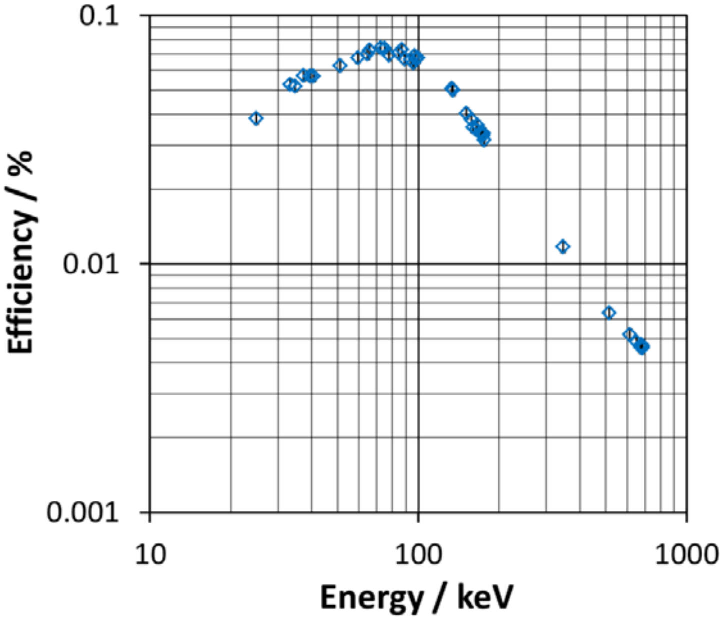

Fig.3-10 The detection efficiency of each muonic X-ray energy for germanium detector 1 in the experiment 2012A0039, calculated by EGS-5 code [47].

3.3-4 Muonic X-ray spectra of pure gas samples

Muonic X-ray spectra of pure gas samples were obtained from the experiments of 2012A0039 (CO: 40 kPa, CO_2: 20 kPa, COS: 18 kPa), 2012B0103 (COS: 10 kPa), and 2015A0192 (CS_2: 20 kPa). Muon irradiations for pure Ne gas (55 kPa in 2012A0039 and 20 kPa in 2012B0103) and pure H_2 gas (99 kPa in 2015A0192) were also performed for estimation of background signals. As representatives, muonic X-ray spectra of Ne, CO_2, and COS are shown in Fig. 3-11 ~ 3-13, respectively. The numbers in parenthesis means the transition of principal quantum numbers by muonic X-ray emission, that is, (2-1) means muonic Kα X-ray. Low background condition enabled us to obtain high transition X-rays from $n \geq 4$ state to 1s in all samples. Due to low intensities of these X-rays, such transitions have been hardly reported until now. In muonic X-ray spectra, the Balmer series of oxygen (25 ~ 44 keV), the Lyman series of carbon (75 ~ 100 keV), and the Lyman series of oxygen (133 ~ 178 keV), were identified. The Balmer series of carbon (14 ~ 25 keV) was also identified by detector 2, 3, and 5, though the enrgy was too small to detect by detector 1 and 4.

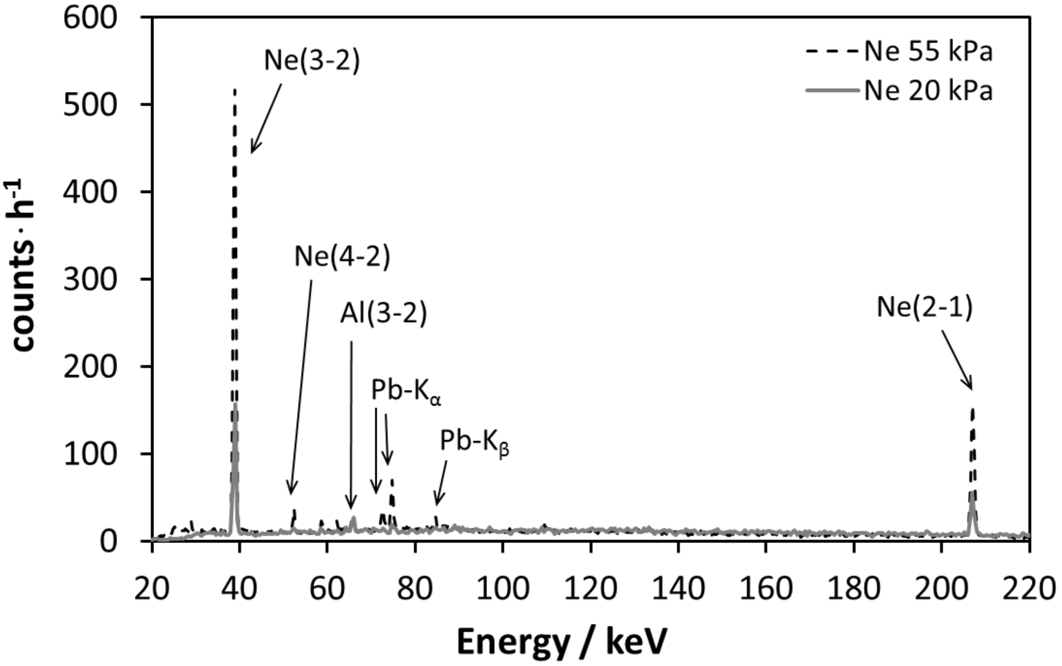

Fig. 3-11 Muonic X-ray spectrum for Ne sample (20~220 keV).

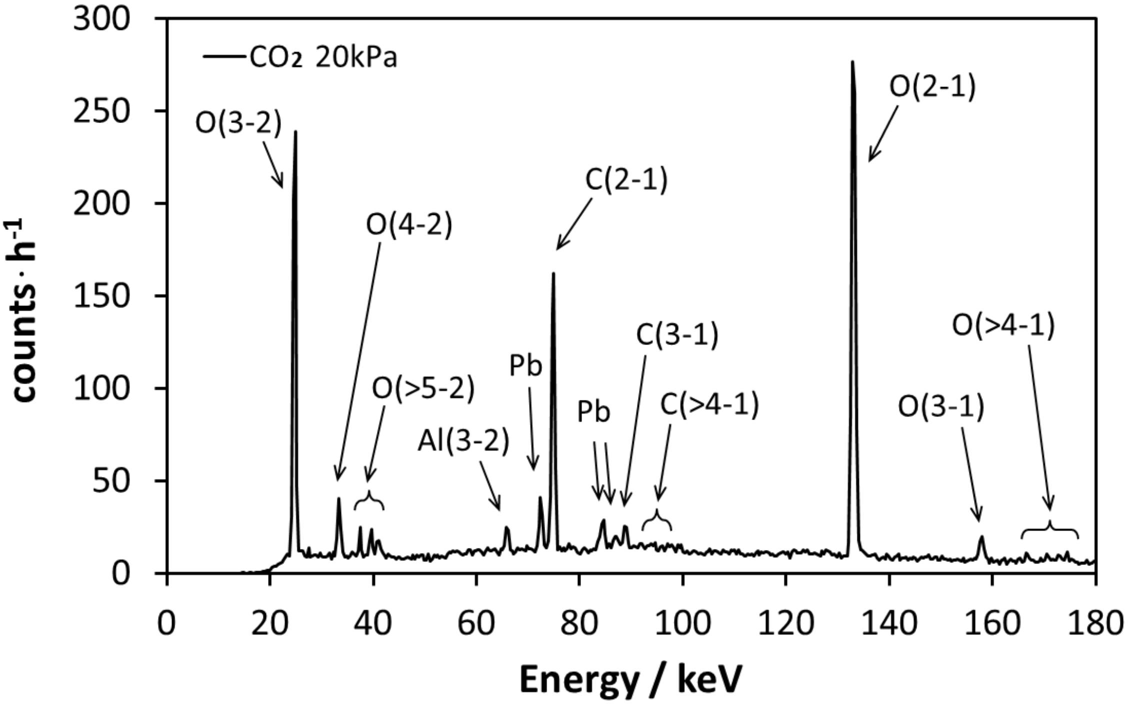

Fig. 3-12 Muonic X-ray spectrum for CO_2 sample (0~180 keV).

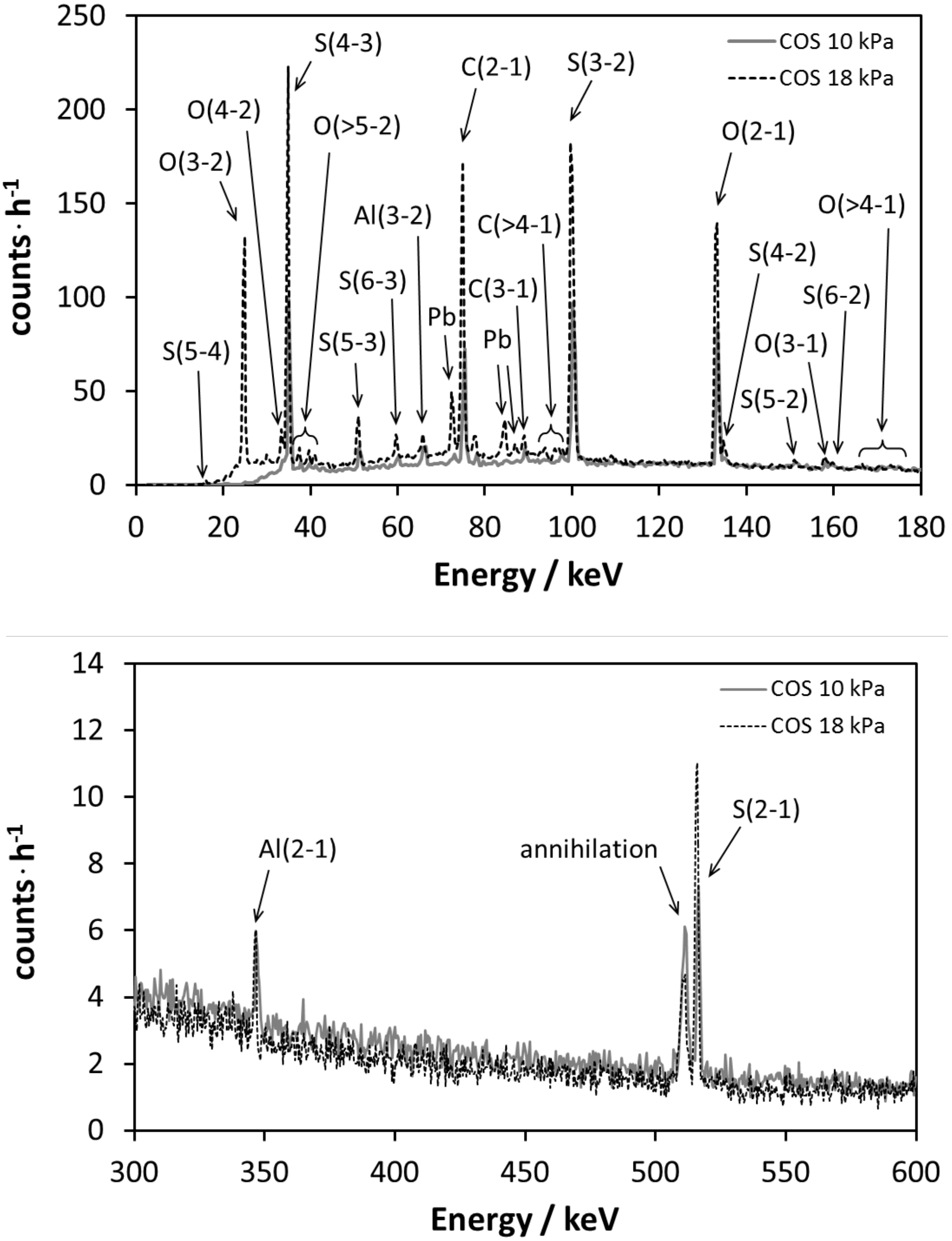

Fig. 3-13 Muonic X-ray spectrum for COS sample (Top: 0~180 keV, Bottom: 300~600 keV).

Emission rates of Muonic X-rays from carbon, oxygen, and sulfur atoms were deduced from muonic X-ray specra of CO, CO_2, COS, and CS_2, and these are summarized in Table 3-4 ~ 3-8. These have been corrected by detection efficiencies of each detector obtained by EGS-5 caluculation [47]. Columns on the table indicate transitions of X-rays emission, X-ray energies [48] (see Appendix), and X-ray emission rate (per second) of each detector, from left to right. In the tables, μC(n'-n) means the X-ray emitting when the muon in muonic carbon de-excites to n' to n, that is, μC(2-1) means K_α X-ray of muonic carbon. μO(n'-n), μS(n'-n) are same manner..

X-ray peaks for μC(2-1): 75.4 keV, μC(3-1): 89.3 keV, μO(3-2): 24.9 keV, μO(4-2): 33.6 keV, and μS(3-2): 99.9 keV are overlapped with background peaks for electronic X-ray of Pb-$K_{\alpha1}$:75.0 keV, μAl(4-2): 88.9 keV, electronic X-ray of Sn-K_α:25.2 keV, μAl(5-3): 33.7 keV, and μAl(5-2): 99.6 keV, respectively. Therefore, intensities of these peaks were corrected by subtracting background peaks which were deduced from background spectra of muon irradiation for Ne, and H_2, gases.

The diferences attributed to detectors were found in muonic X-ray emission rate for sulfur in COS and CS_2 samples (summarized in Table 3-6 ~ 3-8). The Lyman series X-rays deduced from COS with 18 kPa (det-1, det2), COS with 10 kPa (det-2), and CS_2 (det-4) were well corresponded each other. However, μS(3-1) for COS with 10 kPa (det-1) was smaller than other values, in contrast, μS(3-1) for CS_2 (det-5) was larger than other values. The definite reason still has been unclear. Possible reason for this is energies of muonic Lyman X-rays for sulfur atom (600 keV ~). For germanium detector, measurement for this region is more difficult than lower energy region, such as around 100 keV, due to character of detector efficiency.

Table 3-4 Muonic X-ray emission rate of each transition (for CO 40 kPa).

Transitions	Energy [48]	Emission rate of muonic X-rays / s^{-1} det-1	det-2
Lyman series			
μC(2-1)	75.4 keV	213.8 ± 7.4	201.3 ± 6.1
μC(3-1)	89.3 keV	15.7 ± 1.1	18.2 ± 1.0
μC(4-1)	94.2 keV	4.9 ± 0.8	6.2 ± 0.7
μC(5-1)	96.5 keV	4.3 ± 0.8	2.3 ± 0.7
μC(6-1)	97.7 keV	3.4 ± 0.6	1.5 ± 0.6
μC(7-1)	98.4 keV	3.5 ± 0.6	2.5 ± 0.6
μC(>8-1)	98.9 keV	7.5 ± 1.0	4.8 ± 0.9
μO(2-1)	133.3 keV	292.7 ± 9.7	270.8 ± 7.7
μO(3-1)	159.2 keV	16.7 ± 1.4	16.5 ± 1.2
μO(4-1)	167.9 keV	6.3 ± 1.1	4.9 ± 0.9
μO(5-1)	171.9 keV	5.9 ± 1.2	3.9 ± 0.9
μO(6-1)	174.1 keV	5.8 ± 1.1	3.5 ± 0.7
μO(7-1)	175.4 keV	5.2 ± 1.0	4.0 ± 0.8
μO(8-1)	176.3 keV	4.5 ± 1.1	3.3 ± 0.9
μO(>9-1)	176.9 keV	4.8 ± 1.5	2.5 ± 1.2
Balmer series			
μC(3-2)	14.0 keV		264.8 ± 10.6
μC(4-2)	18.8 keV		16.7 ± 1.4
μC(5-2)	21.1 keV		4.5 ± 1.1
μC(6-2)	22.3 keV		2.3 ± 1.0
μC(>7-2)	23.1 keV		4.6 ± 1.0
μO(3-2)	24.9 keV	292.2 ± 11.2	284.9 ± 8.5
μO(4-2)	33.6 keV	20.4 ± 1.2	19.4 ± 1.2
μO(5-2)	37.6 keV	6.8 ± 0.8	7.5 ± 0.7
μO(6-2)	39.8 keV	8.4 ± 0.9	6.0 ± 0.7
μO(7-2)	41.1 keV	7.0 ± 0.8	4.7 ± 0.7
μO(>8-2)	42.0 keV	5.0 ± 1.4	1.4 ± 1.1

Table 3-5 Muonic X-ray emission rate of each transition (for CO_2 20 kPa).

		Emission rate of muonic X-rays / s^{-1}	
Transitions	Energy [48]	det-1	det-2
Lyman series			
μC(2-1)	75.4 keV	73.0 ± 5.0	71.7 ± 4.2
μC(3-1)	89.3 keV	12.9 ± 1.3	10.8 ± 1.1
μC(4-1)	94.2 keV	4.6 ± 1.0	6.0 ± 0.8
μC(5-1)	96.5 keV	3.3 ± 1.0	2.6 ± 0.8
μC(6-1)	97.7 keV	2.5 ± 0.9	2.4 ± 0.8
μC(>7-1)	98.4 keV	5.9 ± 1.5	7.0 ± 1.4
μO(2-1)	133.3 keV	321.6 ± 11.0	312.6 ± 9.2
μO(3-1)	159.2 keV	23.2 ± 2.1	20.4 ± 1.7
μO(4-1)	167.9 keV	8.2 ± 1.6	5.6 ± 1.2
μO(5-1)	171.9 keV	5.7 ± 1.6	6.2 ± 1.3
μO(6-1)	174.1 keV	6.0 ± 1.6	7.7 ± 1.2
μO(7-1)	175.4 keV	6.2 ± 1.6	7.7 ± 1.3
μO(8-1)	176.3 keV	3.7 ± 1.5	4.0 ± 1.1
μO(>9-1)	176.9 keV	-1.7 ± 2.0	1.4 ± 1.6
Balmer series			
μC(3-2)	14.0 keV		89.3 ± 4.6
μC(4-2)	18.8 keV		5.7 ± 1.4
μC(5-2)	21.1 keV		3.4 ± 1.3
μC(6-2)	22.3 keV		3.4 ± 1.3
μC(>7-2)	23.1 keV		4.2 ± 4.3
μO(3-2)	24.9 keV	317.2 ± 12.6	297.1 ± 9.2
μO(4-2)	33.6 keV	29.4 ± 1.9	26.1 ± 1.5
μO(5-2)	37.6 keV	11.2 ± 1.2	11.1 ± 1.1
μO(6-2)	39.8 keV	14.1 ± 1.3	11.0 ± 1.0
μO(7-2)	41.1 keV	9.2 ± 1.1	7.9 ± 1.0
μO(>8-2)	42.0 keV	3.4 ± 1.4	4.2 ± 1.6

Table 3-6 Muonic X-ray emission rate of each transition (for COS 18 kPa).

Transitions	Energy [48]	Emission rate of muonic X-rays / s^{-1} det-1	det-2
Lyman series			
μC(2-1)	75.4 keV	69.8 ± 4.3	71.9 ± 3.3
μC(3-1)	89.3 keV	9.8 ± 0.9	12.1 ± 0.7
μC(4-1)	94.2 keV	3.6 ± 0.7	4.3 ± 0.5
μC(5-1)	96.5 keV	3.2 ± 0.7	2.7 ± 0.5
μC(6-1)	97.7 keV	3.4 ± 0.6	3.1 ± 0.5
μC(>7-1)	98.4 keV	2.5 ± 0.6	2.2 ± 0.4
μO(2-1)	133.3 keV	156.7 ± 5.3	147.3 ± 4.3
μO(3-1)	159.2 keV	10.5 ± 1.2	10.8 ± 0.9
μO(4-1)	167.9 keV	6.3 ± 1.1	6.6 ± 0.8
μO(5-1)	171.9 keV	5.8 ± 1.2	7.1 ± 0.9
μO(6-1)	174.1 keV	5.8 ± 1.2	4.4 ± 0.7
μO(7-1)	175.4 keV	4.3 ± 0.9	4.1 ± 0.7
μO(8-1)	176.3 keV	3.9 ± 1.1	2.6 ± 0.7
μO(>9-1)	176.9 keV	0.7 ± 1.4	0.9 ± 0.9
μS(2-1)	516.0 keV	160.5 ± 8.1	180.1 ± 7.5
μS(3-1)	615.9 keV	18.3 ± 3.5	18.7 ± 3.3
μS(4-1)	650.8 keV	8.9 ± 3.1	9.6 ± 3.4
μS(5-1)	667.0 keV	8.1 ± 3.3	6.6 ± 3.1
μS(6-1)	675.8 keV	4.2 ± 3.3	9.1 ± 3.0
μS(7-1)	681.1 keV	6.7 ± 3.3	5.3 ± 2.9
μS(8-1)	684.5 keV	3.3 ± 3.1	7.5 ± 3.1
μS(9-1)	686.9 keV	11.2 ± 6.9	5.4 ± 2.8

Table 3-6 Muonic X-ray emission rate of each transition (for COS 18 kPa, continued).

		Emission rate of muonic X-rays / s^{-1}	
Transitions	Energy [48]	det-1	det-2
Balmer series			
μC(3-2)	14.0 keV	±	79.3 ± 3.5
μC(4-2)	18.8 keV	±	5.4 ± 0.9
μC(5-2)	21.1 keV	±	3.7 ± 0.8
μC(6-2)	22.3 keV	±	1.9 ± 0.8
μC(>7-2)	23.1 keV	±	4.8 ± 0.8
μO(3-2)	24.9 keV	166.3 ± 6.5	156.8 ± 4.7
μO(4-2)	33.6 keV	15.4 ± 1.0	14.5 ± 0.8
μO(5-2)	37.6 keV	6.8 ± 0.8	5.1 ± 0.5
μO(6-2)	39.8 keV	7.0 ± 0.8	3.8 ± 0.5
μO(7-2)	41.1 keV	4.9 ± 0.7	3.8 ± 0.5
μO(8-2)	42.0 keV	0.7 ± 0.6	0.9 ± 0.4
μO(>9-2)	42.5 keV	1.6 ± 1.0	1.2 ± 0.6
μS(3-2)	99.9 keV	173.3 ± 4.9	149.0 ± 3.8
μS(4-2)	134.8 keV	16.6 ± 1.1	15.1 ± 0.9
μS(5-2)	151.0 keV	6.8 ± 1.0	7.9 ± 0.8
μS(6-2)	159.8 keV	6.3 ± 1.2	5.5 ± 0.8
μS(7-2)	165.1 keV	3.7 ± 1.0	5.4 ± 0.9

Table 3-7 Muonic X-ray emission rate of each transition (for COS 10 kPa).

		Emission rate of muonic X-rays / s^{-1}	
Transitions	Energy [48]	det-1	det-2
Lyman series			
μC(2-1)	75.4 keV	32.2 ± 1.7	32.3 ± 1.8
μC(3-1)	89.3 keV	4.9 ± 0.5	7.1 ± 0.6
μC(4-1)	94.2 keV	1.0 ± 0.4	2.4 ± 0.5
μC(5-1)	96.5 keV	1.5 ± 0.4	1.2 ± 0.5
μC(6-1)	97.7 keV	1.4 ± 0.4	1.3 ± 0.5
μC(>7-1)	98.4 keV	0.2 ± 0.4	1.7 ± 0.5
μO(2-1)	133.3 keV	68.7 ± 2.5	71.4 ± 2.6
μO(3-1)	159.2 keV	4.2 ± 0.8	5.4 ± 0.9
μO(4-1)	167.9 keV	1.5 ± 0.7	0.6 ± 0.8
μO(5-1)	171.9 keV	2.1 ± 0.8	1.0 ± 0.9
μO(6-1)	174.1 keV	1.0 ± 0.7	1.9 ± 0.9
μO(7-1)	175.4 keV	1.1 ± 0.8	2.1 ± 0.9
μO(8-1)	176.3 keV	-0.7 ± 0.8	0.4 ± 0.9
μO(>9-1)	176.9 keV	0.5 ± 0.8	0.5 ± 0.9
μS(2-1)	516.0 keV	71.6 ± 4.7	72.2 ± 5.0
μS(3-1)	615.9 keV	4.3 ± 2.6	6.8 ± 2.9
μS(4-1)	650.8 keV	3.7 ± 2.5	0.3 ± 2.7
μS(5-1)	667.0 keV	4.5 ± 2.6	2.3 ± 2.9
μS(6-1)	675.8 keV	4.7 ± 2.6	4.7 ± 3.0
μS(7-1)	681.1 keV	2.2 ± 2.4	2.7 ± 2.8
μS(8-1)	684.5 keV	1.5 ± 2.5	-1.5 ± 2.7
μS(9-1)	686.9 keV	6.6 ± 2.6	5.5 ± 2.9

Table 3-7 Muonic X-ray emission rate of each transition (for COS 10 kPa, continued).

		Emission rate of muonic X-rays / s^{-1}	
Transitions	Energy [48]	det-1	det-2
Balmer series			
μC(3-2)	14.0 keV		51.1 ± 3.4
μC(4-2)	18.8 keV		4.2 ± 1.0
μC(5-2)	21.1 keV		3.7 ± 0.9
μC(6-2)	22.3 keV		1.9 ± 0.9
μC(>7-2)	23.1 keV		3.7 ± 0.9
μO(3-2)	24.9 keV		85.3 ± 3.5
μO(4-2)	33.6 keV	5.9 ± 0.6	5.8 ± 0.6
μO(5-2)	37.6 keV	2.5 ± 0.5	3.1 ± 0.5
μO(6-2)	39.8 keV	2.3 ± 0.5	2.7 ± 0.4
μO(7-2)	41.1 keV	1.4 ± 0.5	2.4 ± 0.4
μO(8-2)	42.0 keV		0.3 ± 0.4
μO(>9-2)	42.5 keV		0.3 ± 0.4
μS(3-2)	99.9 keV	68.1 ± 2.1	65.2 ± 2.1
μS(4-2)	134.8 keV	5.4 ± 0.7	7.2 ± 0.8
μS(5-2)	151.0 keV	4.1 ± 0.7	2.3 ± 0.8
μS(6-2)	159.8 keV	4.3 ± 0.8	2.2 ± 0.9
μS(7-2)	165.1 keV	2.9 ± 0.8	1.6 ± 0.9

Table 3-8 Muonic X-ray emission rate of each transition (for CS_2 20 kPa).

		Emission rate of muonic X-rays / s^{-1}		
Transitions	Energy [48]	det-2	det-4	det-5
Lyman series				
μC(2-1)	75.4 keV	31.3 ± 2.0	23.4 ± 1.7	25.4 ± 2.9
μC(3-1)	89.3 keV	2.7 ± 0.5	2.7 ± 0.5	2.7 ± 0.7
μC(4-1)	94.2 keV	1.6 ± 0.3	1.0 ± 0.5	1.5 ± 0.4
μC(5-1)	96.5 keV	1.0 ± 0.2	1.9 0.5	1.9 ± 0.4
μC(6-1)	97.7 keV	1.7 ± 0.3	2.0 0.5	2.6 ± 0.4
μC(>7-1)	98.4 keV	1.0 ± 0.2		
μS(2-1)	516.0 keV		144.8 ± 8.2	193.3 ± 10.4
μS(3-1)	615.9 keV		16.9 ± 3.0	35.3 ± 4.0
μS(4-1)	650.8 keV		8.0 ± 3.1	12.6 ± 2.5
μS(5-1)	667.0 keV		6.1 ± 3.0	10.3 ± 3.5
μS(6-1)	675.8 keV		10.1 ± 3.1	9.2 ± 3.3
μS(7-1)	681.1 keV		3.1 ± 3.0	1.5 ± 3.0
μS(8-1)	684.5 keV		-0.9 ± 3.0	2.5 ± 2.9
Balmer series				
μC(3-2)	14.0 keV	22.9 ± 1.36		36.0 ± 2.1
μC(4-2)	18.8 keV	2.8 ± 0.3		4.0 ± 0.6
μC(5-2)	21.1 keV	1.0 ± 0.2		
μC(6-2)	22.3 keV	1.4 ± 0.1		
μS(3-2)	99.9 keV	128.4 ± 6.6	88.9 ± 4.6	134.2 ± 6.9
μS(4-2)	134.8 keV	20.0 ± 1.1	12.2 ± 1.0	19.0 ± 1.2
μS(5-2)	151.0 keV	8.2 ± 0.6	6.0 ± 0.8	9.2 ± 0.8
μS(6-2)	159.8 keV	5.4 ± 0.5	4.2 ± 0.8	6.5 ± 0.7
μS(7-2)	165.1 keV	3.5 ± 0.4	3.1 ± 0.8	5.5 ± 0.7
μS(8-2)	168.5 keV	0.7 0.3	1.7 0.7	1.9 0.6

3.3-5 Muonic X-ray spectra of hydrogen mixture gases

Muonic X-ray spectra of hydrogen mixed gas samples were obtained from the experiments of 2014A0204 (H_2+CO: 99 kPa, H_2+CO: 50 kPa, H_2+CO_2: 99 kPa, and H_2+CO_2: 50 kPa), and 2015A0192 (H_2+COS: 99 kPa, and H_2+CS_2: 99 kPa). Muon irradiations for pure H_2 gases (50 kPa, and 99 kPa) were also performed for estimation of background signals.

Muonic X-ray spectrum derived from hydrogen containing system involves both events, originated from direct muon capture by atom and muon transfer from muonic hydrogen atom. The latter events can be extracted by appropriate width of timing gate on the time resolved emission spectrum. In this thesis, on the time resolved emission spectra of muonic X-ray, the beam coincident events include both muon direct capture and muon transfer events were treated as “prompt”, and delayed damping events consist of only muon transfer events were treated as “delayed”. These two regions are explained by using a time resolved emission spectrum in Fig 3-14. Setting timing gates in prompt and delayed regions on the time resolved emission spectrum for each sample, muonic X-ray energy spectra for prompt and delayed events were selectively created. As representatives, prompt and delayed muonic X-ray spectrum for H_2+CO at 99 kPa are shown in Fig. 3-15, and 3-16, respectively.

In muon transfer process, because the muon transferred to deep binding state, the muonic X-rays originated from n>5 states were not observed for carbon, and from n>6 states were not observed for oxygen. These are consistent to previous result of muon transfer for oxygen atom [49,50].

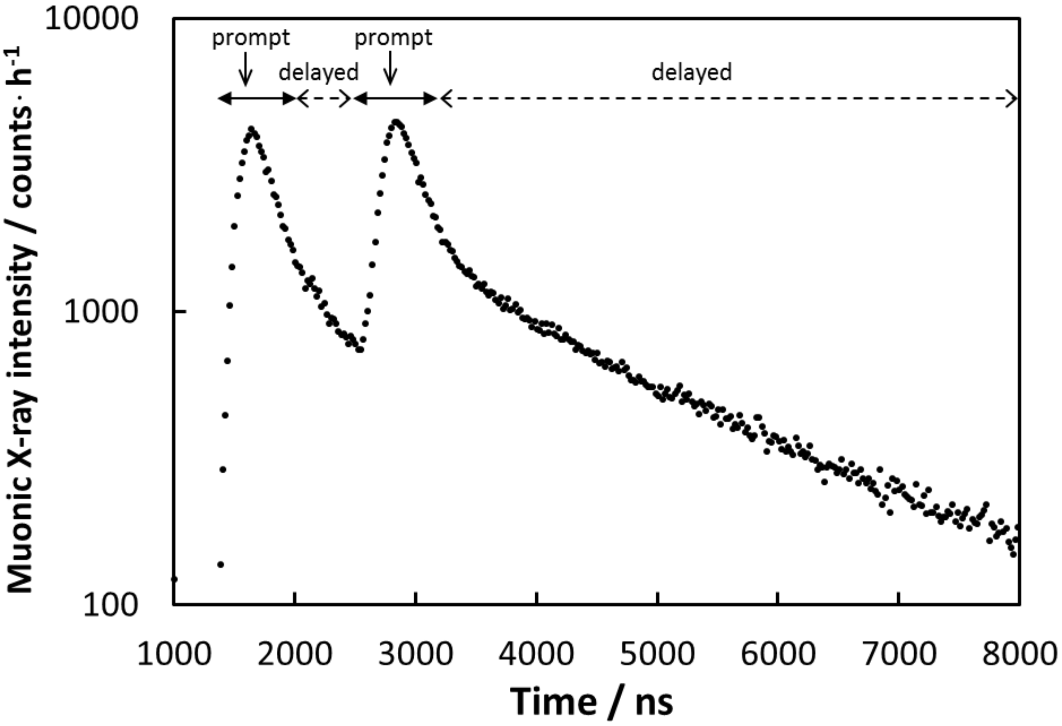

Fig. 3-14 Time resolved emission spectrum between operation signal of accelerator and muonic X-ray detection signal for H_2+CO sample (50 kPa), measured by det-2. Two large peaks mainly reflect direct muon capturing by carbon and oxygen atoms. The regions behind of the peak are attributed to muonic X-rays of carbon and oxygen atom emitted after transferring muon from muonic hydrogen. Solid arrows indicate prompt regions, dashed arrows indicate delayed regions.

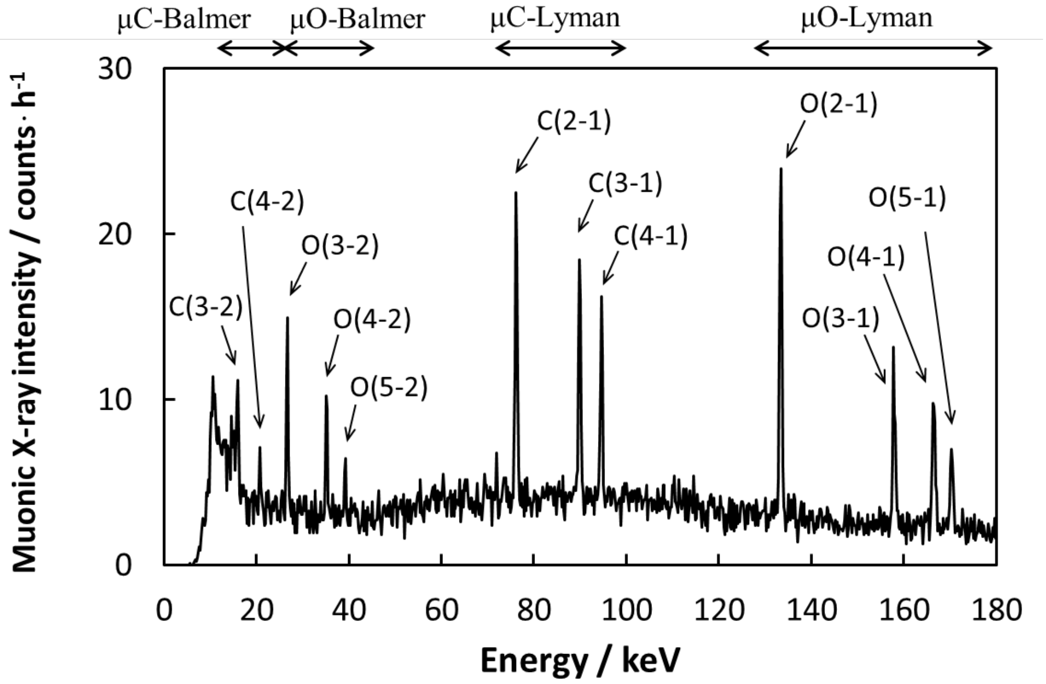

Fig. 3-15 Muonic X-ray spectrum for H_2+CO sample (99 kPa), derived from prompt region events, detector No.2 was used by measurement.

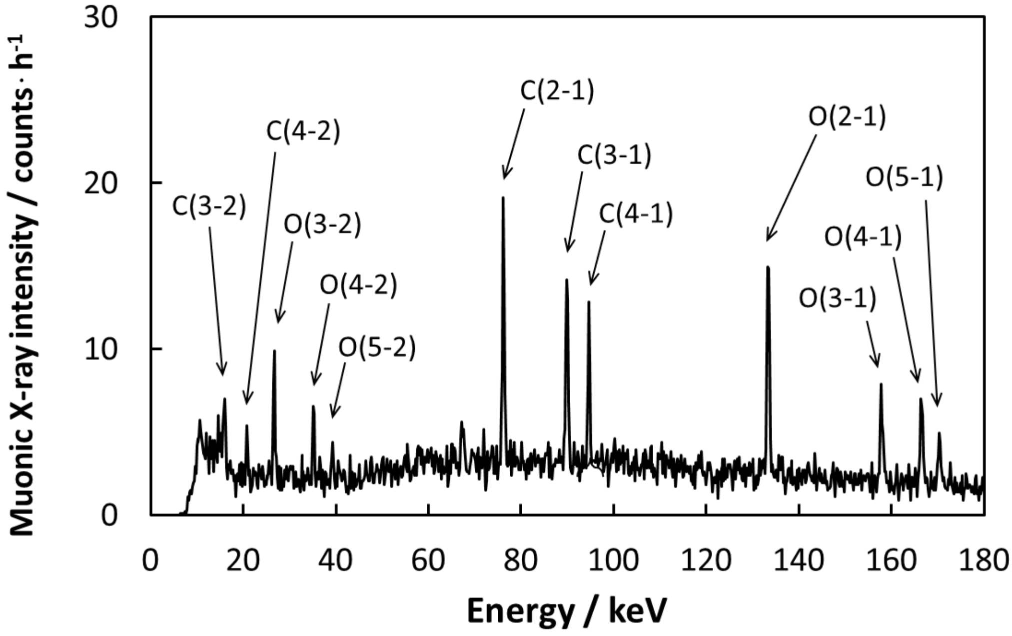

Fig. 3-16 Muonic X-ray spectrum for H_2+CO sample (99 kPa), derived from delayed region events, detector No.2 was used by measurement.

Intensities of Muonic X-rays from carbon, oxygen, and sulfur atoms were deduced from muonic X-ray specra of H_2+CO: 99 kPa, H_2+CO: 50 kPa, H_2+CO_2: 99 kPa, H_2+CO_2: 50 kPa, H_2+COS: 99 kPa, and H_2+CS_2: 99 kPa. X-ray intensities in prompt regions and delayed regions were summarized in Table 3-9 ~ 3-20.

Lyman series X-rays from carbon, oxygen, and sulfur, Balmer sereirs X-rays from carbon, oxygen, and sulfur are listed in order from the top of the tables to bottom. Columns on the table mean transitions when X-rays were emitted, X-ray energies, and X-ray intensities (per hour) of each detector, from left to right.

Peak areas for X-rays of μC(2-1): 75.4 keV, μC(3-1): 89.3 keV, μO(3-2): 24.9 keV, μO(4-2): 33.6 keV, and μS(3-2): 99.9 keV, were corrected by same procedure to pure gas samples.

Table 3-9 Muonic X-ray emission rate of each transition (for H_2+CO 99 kPa).

		Emission rate of muonic X-rays / s^{-1}		
prompt	Energy [48]	det-2	det-3	det-4
Lyman series				
μC(2-1)	75.4 keV	7.4 ± 0.7	30.5 ± 3.1	4.9 ± 0.5
μC(3-1)	89.3 keV	4.8 ± 0.5	11.5 ± 2.5	2.8 ± 0.5
μC(4-1)	94.2 keV	4.3 ± 0.4	6.2 ± 1.3	1.5 ± 0.3
μO(2-1)	133.3 keV	17.8 ± 1.2	37.2 ± 3.5	9.5 ± 0.7
μO(3-1)	159.2 keV	10.0 ± 0.9	12.1 ± 2.6	4.1 ± 0.5
μO(4-1)	167.9 keV	9.8 ± 0.9	20.5 ± 3.4	4.8 ± 0.6
μO(5-1)	171.9 keV	7.2 ± 0.8	11.8 ± 2.9	2.7 ± 0.5
Balmer series				
μC(3-2)	14.0 keV	3.4 ± 0.6	16.3 ± 2.1	1.2 ± 0.5
μC(4-2)	18.8 keV	0.7 ± 0.3	3.6 ± 1.1	0.6 ± 0.3
μO(3-2)	24.9 keV	4.3 ± 0.5	17.7 ± 3.7	0.6 ± 1.1
μO(4-2)	33.6 keV	3.3 ± 0.4	6.2 ± 1.3	1.1 ± 0.3
μO(5-2)	37.6 keV	1.5 ± 0.3	5.6 ± 1.0	0.5 ± 0.2

Table 3-10 Muonic X-ray emission rate of each transition (for H_2+CO 99 kPa).

		Emission rate of muonic X-rays / s^{-1}		
delayed	Energy [48]	det-2	det-3	det-4
Lyman series				
μC(2-1)	75.4 keV	7.8 ± 0.8	41.4 ± 3.9	14.3 ± 1.6
μC(3-1)	89.3 keV	6.0 ± 0.7	30.4 ± 2.8	9.3 ± 0.9
μC(4-1)	94.2 keV	3.9 ± 0.4	18.6 ± 2.1	7.8 ± 0.7
μO(2-1)	133.3 keV	10.8 ± 0.8	44.7 ± 4.2	21.8 ± 1.4
μO(3-1)	159.2 keV	5.8 ± 0.7	26.8 ± 3.8	13.4 ± 1.0
μO(4-1)	167.9 keV	6.4 ± 0.7	27.6 ± 4.1	14.2 ± 1.1
μO(5-1)	171.9 keV	3.9 ± 0.6	21.1 ± 3.8	9.0 ± 0.9
Balmer series				
μC(3-2)	14.0 keV	3.5 ± 0.6	13.0 ± 2.1	5.6 ± 1.1
μC(4-2)	18.8 keV	1.4 ± 0.3	6.5 ± 1.3	3.3 ± 0.6
μO(3-2)	24.9 keV	3.5 ± 0.4	18.3 ± 2.5	9.3 ± 1.7
μO(4-2)	33.6 keV	1.4 ± 0.3	15.7 ± 1.6	5.4 ± 0.6
μO(5-2)	37.6 keV	1.0 ± 0.3	6.4 ± 1.1	2.9 ± 0.4

Table 3-11 Muonic X-ray emission rate of each transition (for H_2+CO 50 kPa).

		Emission rate of muonic X-rays / s^{-1}		
prompt	Energy [48]	det-2	det-3	det-4
Lyman series				
μC(2-1)	75.4 keV	3.7 ± 0.5	12.1 ± 2.1	1.0 ± 0.4
μC(3-1)	89.3 keV	0.4 ± 0.6	2.6 ± 2.5	1.1 ± 0.5
μC(4-1)	94.2 keV	0.7 ± 0.3	3.5 ± 1.2	0.6 ± 0.2
μO(2-1)	133.3 keV	6.0 ± 0.6	13.2 ± 2.1	3.7 ± 0.4
μO(3-1)	159.2 keV	2.5 ± 0.5	5.1 ± 2.3	1.5 ± 0.4
μO(4-1)	167.9 keV	3.2 ± 0.5	2.6 ± 2.6	1.0 ± 0.4
μO(5-1)	171.9 keV	1.9 ± 0.5	2.2 ± 2.6	1.4 ± 0.4
Balmer series				
μC(3-2)	14.0 keV	2.0 ± 0.5	5.5 ± 1.5	0.5 ± 0.5
μC(4-2)	18.8 keV	0.2 ± 0.2	1.6 ± 0.9	0.6 ± 0.3
μO(3-2)	24.9 keV	1.4 ± 0.3	4.9 ± 3.4	0.4 ± 1.0
μO(4-2)	33.6 keV	0.8 ± 0.2	3.5 ± 1.4	0.0 ± 0.2
μO(5-2)	37.6 keV	0.2 ± 0.2	1.2 ± 0.7	0.3 ± 0.2

Table 3-12 Muonic X-ray emission rate of each transition (for H_2+CO 50 kPa).

		Emission rate of muonic X-rays / s^{-1}		
delayed	Energy [48]	det-2	det-3	det-4
Lyman series				
μC(2-1)	75.4 keV	2.7 ± 0.6	9.4 ± 2.2	6.6 ± 1.0
μC(3-1)	89.3 keV	2.8 ± 0.5	10.2 ± 1.7	3.2 ± 0.8
μC(4-1)	94.2 keV	1.9 ± 0.3	6.0 ± 1.3	2.1 ± 0.4
μO(2-1)	133.3 keV	4.4 ± 0.5	18.7 ± 2.4	7.6 ± 0.7
μO(3-1)	159.2 keV	2.4 ± 0.4	10.1 ± 2.5	4.8 ± 0.6
μO(4-1)	167.9 keV	3.2 ± 0.5	9.7 ± 2.6	4.8 ± 0.6
μO(5-1)	171.9 keV	2.0 ± 0.4	4.7 ± 2.3	3.7 ± 0.6
Balmer series				
μC(3-2)	14.0 keV	2.0 ± 0.5	5.9 ± 1.6	2.0 ± 0.8
μC(4-2)	18.8 keV	0.5 ± 0.3	3.1 ± 1.0	1.3 ± 0.5
μO(3-2)	24.9 keV	1.8 ± 0.3	6.7 ± 1.7	6.8 ± 1.4
μO(4-2)	33.6 keV	1.7 ± 0.3	4.3 ± 0.9	0.5 ± 0.4
μO(5-2)	37.6 keV	0.2 ± 0.2	3.6 ± 0.8	1.1 ± 0.3

Table 3-13 Muonic X-ray emission rate of each transition (for H_2+CO_2 99 kPa).

		Emission rate of muonic X-rays / s^{-1}		
prompt	Energy [48]	det-2	det-3	det-4
Lyman series				
μC(2-1)	75.4 keV	5.9 ± 0.6	23.3 ± 2.7	3.3 ± 0.5
μC(3-1)	89.3 keV	4.6 ± 0.5	12.2 ± 2.5	2.5 ± 0.5
μC(4-1)	94.2 keV	3.1 ± 0.4	5.5 ± 1.3	1.6 ± 0.3
μO(2-1)	133.3 keV	29.1 ± 1.7	58.2 ± 4.5	16.2 ± 1.0
μO(3-1)	159.2 keV	13.2 ± 1.0	22.1 ± 3.2	6.6 ± 0.6
μO(4-1)	167.9 keV	15.4 ± 1.2	28.0 ± 3.9	7.1 ± 0.7
μO(5-1)	171.9 keV	10.5 ± 0.9	15.4 ± 3.1	4.2 ± 0.5
Balmer series				
μC(3-2)	14.0 keV	3.3 ± 0.6	7.1 ± 1.6	0.8 ± 0.4
μC(4-2)	18.8 keV	1.1 ± 0.3	2.9 ± 1.0	0.9 ± 0.3
μO(3-2)	24.9 keV	6.6 ± 0.6	23.9 ± 4.1	1.7 ± 1.1
μO(4-2)	33.6 keV	4.9 ± 0.5	15.7 ± 1.7	1.8 ± 0.3
μO(5-2)	37.6 keV	1.9 ± 0.3	5.8 ± 1.0	0.7 ± 0.2

Table 3-14 Muonic X-ray emission rate of each transition (for H_2+CO_2 99 kPa).

		Emission rate of muonic X-rays / s^{-1}		
delayed	Energy [48]	det-2	det-3	det-4
Lyman series				
μC(2-1)	75.4 keV	4.8 ± 0.7	24.9 ± 3.4	8.5 ± 1.3
μC(3-1)	89.3 keV	3.9 ± 0.6	18.1 ± 2.2	6.7 ± 0.8
μC(4-1)	94.2 keV	2.6 ± 0.4	13.6 ± 1.8	4.8 ± 0.5
μO(2-1)	133.3 keV	11.8 ± 0.9	59.3 ± 4.7	29.6 ± 1.7
μO(3-1)	159.2 keV	6.5 ± 0.7	35.5 ± 4.2	16.2 ± 1.1
μO(4-1)	167.9 keV	8.3 ± 0.8	40.2 ± 4.7	16.8 ± 1.2
μO(5-1)	171.9 keV	4.6 ± 0.6	26.8 ± 4.0	10.8 ± 0.9
Balmer series				
μC(3-2)	14.0 keV	2.1 ± 0.5	9.6 ± 2.0	3.0 ± 1.0
μC(4-2)	18.8 keV	0.8 ± 0.3	6.7 ± 1.3	1.1 ± 0.5
μO(3-2)	24.9 keV	4.2 ± 0.4	26.5 ± 2.7	10.3 ± 1.8
μO(4-2)	33.6 keV	1.8 ± 0.3	21.4 ± 1.8	7.2 ± 0.7
μO(5-2)	37.6 keV	1.4 ± 0.3	8.1 ± 1.2	3.3 ± 0.4

Table 3-15 Muonic X-ray emission rate of each transition (for H_2+CO_2 50 kPa).

		Emission rate of muonic X-rays / s^{-1}		
prompt	Energy [48]	det-2	det-3	det-4
Lyman series				
μC(2-1)	75.4 keV	3.2 ± 0.4	7.6 ± 1.9	1.1 ± 0.3
μC(3-1)	89.3 keV	0.8 ± 0.3	2.4 ± 2.3	0.7 ± 0.5
μC(4-1)	94.2 keV	0.7 ± 0.2	2.4 ± 1.0	0.9 ± 0.2
μO(2-1)	133.3 keV	9.5 ± 0.7	22.7 ± 2.4	5.1 ± 0.4
μO(3-1)	159.2 keV	4.0 ± 0.5	7.5 ± 2.2	1.9 ± 0.4
μO(4-1)	167.9 keV	4.6 ± 0.5	7.2 ± 2.3	1.7 ± 0.4
μO(5-1)	171.9 keV	3.5 ± 0.5	5.1 ± 2.2	1.5 ± 0.4
Balmer series				
μC(3-2)	14.0 keV	1.4 ± 0.4	3.2 ± 1.3	1.3 ± 0.4
μC(4-2)	18.8 keV	0.8 ± 0.3	0.7 ± 0.8	0.4 ± 0.2
μO(3-2)	24.9 keV	2.4 ± 0.3	3.5 ± 3.3	0.0 ± 0.9
μO(4-2)	33.6 keV	1.2 ± 0.2	4.6 ± 1.4	0.0 ± 0.2
μO(5-2)	37.6 keV	1.0 ± 0.2	1.7 ± 0.7	0.2 ± 0.2

Table 3-16 Muonic X-ray emission rate of each transition (for H_2+CO_2 50 kPa).

		Emission rate of muonic X-rays / s^{-1}		
delayed	Energy [48]	det-2	det-3	det-4
Lyman series				
μC(2-1)	75.4 keV	1.9 ± 0.5	8.5 ± 2.0	4.9 ± 0.9
μC(3-1)	89.3 keV	1.8 ± 0.5	9.4 ± 1.5	4.1 ± 0.7
μC(4-1)	94.2 keV	1.3 ± 0.3	5.5 ± 1.1	1.5 ± 0.3
μO(2-1)	133.3 keV	6.7 ± 0.5	19.6 ± 2.3	12.4 ± 0.8
μO(3-1)	159.2 keV	4.1 ± 0.5	15.5 ± 2.6	6.7 ± 0.7
μO(4-1)	167.9 keV	4.9 ± 0.5	19.2 ± 3.0	8.1 ± 0.7
μO(5-1)	171.9 keV	3.2 ± 0.4	11.6 ± 2.6	4.8 ± 0.6
Balmer series				
μC(3-2)	14.0 keV	1.2 ± 0.4	4.3 ± 1.3	2.3 ± 0.9
μC(4-2)	18.8 keV	0.7 ± 0.2	3.0 ± 0.9	1.3 ± 0.5
μO(3-2)	24.9 keV	2.1 ± 0.3	6.8 ± 1.8	5.9 ± 1.4
μO(4-2)	33.6 keV	1.1 ± 0.3	7.9 ± 1.0	1.7 ± 0.4
μO(5-2)	37.6 keV	0.7 ± 0.2	3.7 ± 0.8	2.1 ± 0.3

Table 3-17 Muonic X-ray emission rate of each transition (for H_2+COS 99 kPa).

		Emission rate of muonic X-rays / s^{-1}		
prompt	Energy [48]	det-2	det-4	det-5
Lyman series				
μC(2-1)	75.4 keV	21.6 ± 2.0	4.2 ± 1.0	7.0 ± 0.6
μC(3-1)	89.3 keV	12.0 ± 1.9	3.2 ± 0.6	3.0 ± 0.8
μC(4-1)	94.2 keV	7.8 ± 0.8	2.9 ± 0.4	3.4 ± 0.4
μC(5-1)	96.5 keV	1.8 ± 0.6	1.5 ± 0.4	0.9 ± 0.3
μO(2-1)	133.3 keV	33.9 ± 2.0	10.9 ± 0.8	10.1 ± 0.7
μO(3-1)	159.2 keV	11.0 ± 1.0	5.1 ± 0.7	5.7 ± 0.5
μO(4-1)	167.9 keV	11.9 ± 1.1	6.1 ± 0.8	5.8 ± 0.5
μO(5-1)	171.9 keV	8.1 ± 0.9	3.9 ± 0.7	4.5 ± 0.5
μO(6-1)	174.1 keV	±	1.9 ± 0.7	2.1 ± 0.4
μS(2-1)	516.0 keV	±	18.3 ± 2.0	21.9 ± 1.9
μS(3-1)	615.9 keV	±	3.5 ± 1.5	9.8 ± 2.0
μS(4-1)	650.8 keV	±	0.8 ± 1.5	3.7 ± 1.2
μS(5-1)	667.0 keV	±	4.6 ± 1.7	5.7 ± 1.8
μS(6-1)	675.8 keV	±	6.0 ± 1.8	4.7 ± 1.7
μS(7-1)	681.1 keV	±	1.0 ± 1.5	7.0 ± 1.8
μS(8-1)	684.5 keV	±	3.0 ± 1.7	2.9 ± 1.5

Table 3-17 Muonic X-ray emission rate of each transition (for H_2+COS 99 kPa, continued).

		Emission rate of muonic X-rays / s^{-1}		
prompt	Energy [48]	det-2	det-4	det-5
Balmer series				
μC(3-2)	14.0 keV	14.9 ± 1.4		12.6 ± 1.1
μC(4-2)	18.8 keV	6.4 ± 0.7		3.6 ± 0.5
μC(5-2)	21.1 keV	2.3 ± 0.5		±
μC(6-2)	22.3 keV	1.9 ± 0.1		±
μO(3-2)	24.9 keV	22.0 ± 1.4		8.1 ± 0.6
μO(4-2)	33.6 keV	9.2 ± 1.1		1.9 ± 0.3
μO(5-2)	37.6 keV	5.8 ± 0.6		0.9 ± 0.2
μO(6-2)	39.8 keV	1.1 ± 0.4		0.03 ± 0.2
μO(7-2)	41.1 keV	0.8 ± 0.3		±
μS(3-2)	99.9 keV	24.9 ± 2.0	4.7 ± 0.6	8.9 ± 1.1
μS(4-2)	134.8 keV	6.5 ± 0.8	3.4 ± 0.6	2.4 ± 0.3
μS(5-2)	151.0 keV	7.0 ± 1.0	3.3 ± 0.6	2.5 ± 0.4
μS(6-2)	159.8 keV		3.1 ± 0.7	1.1 ± 0.3
μS(7-2)	165.1 keV		2.4 ± 0.6	0.4 ± 0.4

Table 3-18 Muonic X-ray emission rate of each transition (for H_2+COS 99 kPa).

		Emission rate of muonic X-rays / s^{-1}		
delayed	Energy [48]	det-2	det-4	det-5
Lyman series				
μC(2-1)	75.4 keV	14.6 ± 2.1	5.0 ± 0.7	8.1 ± 0.6
μC(3-1)	89.3 keV	11.7 ± 0.9	1.8 ± 0.6	4.0 ± 0.5
μC(4-1)	94.2 keV	9.3 ± 0.8	1.4 ± 0.6	2.3 ± 0.4
μC(5-1)	96.5 keV	1.0 ± 0.5		
μO(2-1)	133.3 keV	31.7 ± 2.0	5.2 ± 0.8	13.4 ± 0.9
μO(3-1)	159.2 keV	16.5 ± 1.4	3.6 ± 0.9	5.5 ± 0.6
μO(4-1)	167.9 keV	18.6 ± 1.5	3.0 ± 0.9	5.6 ± 0.7
μO(5-1)	171.9 keV	10.2 ± 1.1	1.7 ± 0.9	3.7 ± 0.6
μO(6-1)	174.1 keV		0.2 ± 0.9	
μS(2-1)	516.0 keV		20.7 ± 4.0	16.9 ± 2.5
μS(3-1)	615.9 keV		0.8 ± 4.3	11.0 ± 3.2
μS(4-1)	650.8 keV		5.7 ± 4.6	2.0 ± 2.0
μS(5-1)	667.0 keV		-4.7 ± 4.5	4.6 ± 3.1
μS(6-1)	675.8 keV		1.4 ± 4.6	6.3 ± 3.0
μS(7-1)	681.1 keV		-0.5 ± 4.7	3.1 ± 2.8
Balmer series				
μC(3-2)	14.0 keV	8.4 ± 1.2		7.7 ± 0.8
μC(4-2)	18.8 keV	2.4 ± 0.6		0.7 ± 0.4
μO(3-2)	24.9 keV	11.7 ± 0.9		7.9 ± 0.7
μO(4-2)	33.6 keV	6.0 ± 0.6		0.7 ± 0.3
μO(5-2)	37.6 keV	2.1 ± 0.4		0.6 ± 0.3
μO(6-2)	39.8 keV	0.2 ± 0.4		-0.1 ± 0.3
μS(3-2)	99.9 keV	3.0 ± 0.9	0.5 ± 0.8	-0.5 ± 0.4
μS(4-2)	134.8 keV	3.1 ± 0.7	2.8 ± 0.9	1.5 ± 0.4
μS(5-2)	151.0 keV	2.3 ± 0.8	1.0 ± 0.9	2.0 ± 0.5
μS(6-2)	159.8 keV	0.3 ± 0.8	3.4 ± 1.0	0.6 ± 0.5
μS(7-2)	165.1 keV		-0.3 ± 1.0	0.7 ± 0.5

Table 3-19 Muonic X-ray emission rate of each transition (for H_2+CS_2 99 kPa).

		Emission rate of muonic X-rays / s^{-1}		
prompt	Energy [48]	det-2	det-4	det-5
Lyman series				
μC(2-1)	75.4 keV	17.4 ± 1.9	3.5 ± 0.9	6.0 ± 0.6
μC(3-1)	89.3 keV	9.2 ± 1.7	1.6 ± 0.6	1.4 ± 0.7
μC(4-1)	94.2 keV	7.0 ± 0.8	2.0 ± 0.4	2.5 ± 0.4
μC(5-1)	96.5 keV	2.1 ± 0.7		
μS(2-1)	516.0 keV		24.5 ± 2.5	32.1 ± 2.5
μS(3-1)	615.9 keV		6.1 ± 1.7	12.6 ± 2.1
μS(4-1)	650.8 keV		7.2 ± 1.9	4.8 ± 1.3
μS(5-1)	667.0 keV		6.1 ± 1.8	8.6 ± 2.0
μS(6-1)	675.8 keV		5.8 ± 1.8	6.1 ± 1.8
μS(7-1)	681.1 keV		4.7 ± 1.8	6.2 ± 1.7
μS(8-1)	684.5 keV		4.1 ± 1.8	-1.4 ± 1.2
Balmer series				
μC(3-2)	14.0 keV	12.0 ± 1.3		
μS(3-2)	99.9 keV	41.1 ± 2.8	7.7 ± 0.8	13.2 ± 1.2
μS(4-2)	134.8 keV	10.4 ± 1.1	3.0 ± 0.7	5.9 ± 0.5
μS(5-2)	151.0 keV		1.8 ± 0.7	2.0 ± 0.4
μS(6-2)	159.8 keV		1.7 ± 0.8	2.2 ± 0.4
μS(7-2)	165.1 keV		2.3 ± 0.8	1.6 ± 0.4
μS(8-2)	168.5 keV		0.9 ± 0.8	0.2 ± 0.3

Table 3-20 Muonic X-ray emission rate of each transition (for H_2+CS_2 99 kPa).

		Emission rate of muonic X-rays / s^{-1}		
delayed	Energy [48]	det-2	det-4	det-5
Lyman series				
μC(2-1)	75.4 keV	14.4 ± 2.0	4.4 ± 0.6	6.8 ± 0.6
μC(3-1)	89.3 keV	11.1 ± 0.9	1.3 ± 0.5	3.2 ± 0.4
μC(4-1)	94.2 keV	8.4 ± 0.8	1.4 ± 0.5	2.5 ± 0.4
μS(2-1)	516.0 keV		26.1 ± 4.1	57.7 ± 4.2
μS(3-1)	615.9 keV		12.5 ± 3.9	21.5 ± 3.8
μS(4-1)	650.8 keV		2.8 ± 4.3	12.4 ± 2.6
μS(5-1)	667.0 keV		5.5 ± 4.3	23.4 ± 4.2
μS(6-1)	675.8 keV		9.2 ± 4.4	11.5 ± 3.6
μS(7-1)	681.1 keV		8.4 ± 4.5	13.6 ± 3.6
μS(8-1)	684.5 keV		5.8 ± 4.4	1.8 ± 3.2
Balmer series				
μC(3-2)	14.0 keV	8.2 ± 1.1		
μC(4-2)	18.8 keV	2.4 ± 0.6		
μS(3-2)	99.9 keV	5.3 ± 1.0	1.1 ± 0.7	1.1 ± 0.5
μS(4-2)	134.8 keV	2.9 ± 0.8	3.0 ± 0.8	1.4 ± 0.6
μS(5-2)	151.0 keV	2.8 ± 0.9	3.4 ± 0.9	1.7 ± 0.6
μS(6-2)	159.8 keV	4.1 ± 1.0	2.8 ± 0.9	0.5 ± 0.6
μS(7-2)	165.1 keV	5.1 ± 1.1	3.8 ± 0.9	-0.5 ± 0.6
μS(8-2)	168.5 keV	0.5 ± 0.9		

3.4 Result II: Muon capture ratio

3.4-1 Muon capture ratio: relative muon capture probability of constituent atoms

In muon capture for CO, CO_2, COS, and CS_2, the muon capture number of each constituent atom can be obtained from total intensity of muonic Lyman X-ray series of atoms, because the captured muon finally de-excites to muon 1s state. Taking the ratio of muon capture number of each constituent atom, relative muon capture probability (muon capture ratio) is deduced. For example, per atom muon capture ratio for carbon to oxygen: A(C/O) is described as formula (3-1).

$$A(C/O)_{sample} = \frac{I\mu C(n-1)}{I\mu O(n-1)} \times \frac{n}{m} \qquad (3\text{-}1)$$

where, $I\mu C$(n-1) is total muonic X-ray intensity of Lyman series transitions from carbon atom, $I\mu O$(n-1) is total muonic X-ray intensity of Lyman series transitions from oxygen atom, “m” and “n” mean number of atoms in the molecule C_mO_n.

As a same manner, per atom muon capture ratio for sulfur to oxygen is described as formula (3-2), and that for sulfur to carbon is described as formula (3-3).

$$A(S/O)_{sample} = \frac{I\mu S(n-1)}{I\mu O(n-1)} \times \frac{n}{m} \qquad (3\text{-}2)$$

$$A(S/C)_{sample} = \frac{I\mu S(n-1)}{I\mu C(n-1)} \times \frac{n}{m} \qquad (3\text{-}3)$$

3.4-2 Muon capture ratios of pure gas sample

In this study, following transition series were applied for determination of the muon capture numbers, the sum of transition series (2-1) to (6-1) and over (6-1) for carbon atom, the sum of (2-1) to (8-1) and over (8-1) for oxygen atom, and the sum of (2-1) to (8-1) and over (8-1) for sulfur atom. Muon capture ratio: A(C/O), A(S/O), A(S/C), for CO, CO_2, COS, and CS_2 samples are described in Table 3-21. The values of A(C/O), A(S/O), and A(S/C) for two different density conditions of COS samples (18kPa and 10 kPa) were within 1σ error. Results for CO, CO_2, and COS molecules: $A(C/O)_{CO} = 0.753 \pm 0.021$, $A(C/O)_{CO2} = 0.549 \pm 0.023$, $A(C/O)_{COS} = 0.500 \pm 0.018$ at 18 kPa were reported by the author [51].

The muon capture ratios for CO and CO_2 in high pressure sample conditions [24,27,52] are also shown in Table 3-21. In the case of CO, it is well agreement with our value though previous value was ignored some low-intensity muonic X-ray series. In the study, Sum of intensies for transition series of (2-1) to (4-1) for carbon atom, and (2-1) to (6-1) for oxygen atom, were used to conduct the muon capture ratio [27]. In the case of CO_2, both reported values conducted by muon life measurement in high pressure gas. They determined the life of muonic atom from the time emission spectrum of decay electrons from the muons in muonic atoms, and obtained the muon capture numbers from the each decay curve. The result from Kubo [52] is in agreement with our value, whereas the result from Suzuki [24] is not well in agreement with the values in this thesis.

Table 3-21 Muon capture ratio: A(C/O), A(S/O), A(S/C), for CO, CO_2, COS, and CS_2 samples.

Sample	Muon capture ratio	Sample	Muon capture ratio
CO	A(C/O)	COS , 18 kPa	A(S/O)
det-1	0.740 ± 0.032	det-1	1.140 ± 0.078
det-2	0.766 ± 0.029	det-2	1.318 ± 0.069
average	0.753 ± 0.021	average	1.229 ± 0.052
Ref.[27]	0.766 ± 0.030	COS , 10 kPa	A(S/O)
		det-1	1.262 ± 0.117
CO_2	A(C/O)	det-2	1.115 ± 0.118
det-1	0.548 ± 0.035	average	1.189 ± 0.083
det-2	0.550 ± 0.030	COS	A(S/O)
average	0.549 ± 0.023	*average	1.215 ± 0.044
Ref.[52]	0.56 ± 0.08		
Ref.[24]	0.43 ± 0.02		
			A(S/C)
COS , 18 kPa	A(C/O)	COS , 18 kPa	
det-1	0.476 ± 0.028	det-1	2.395 ± 0.187
det-2	0.524 ± 0.024	det-2	2.515 ± 0.147
average	0.500 ± 0.018	average	2.455 ± 0.119
COS , 10 kPa	A(C/O)	COS , 10 kPa	A(S/C)
det-1	0.525 ± 0.033	det-1	2.405 ± 0.230
det-2	0.552 ± 0.035	det-2	2.021 ± 0.217
average	0.538 ± 0.024	average	2.213 ± 0.158
COS	A(C/O)	COS	A(S/C)
*average	0.513 ± 0.015	*average	2.373 ± 0.095
		CS_2	A(S/C)
		det-4	3.330 ± 0.135
		det-5	3.375 ± 0.121
		average	3.352 ± 0.091

* Average value of COS, 18 kPa and COS, 10 kPa

3.4-3 Muon capture ratios of hydrogen mixture sample

Same as the experiments using pure gas samples, muon capture ratio were deduced in hydrogen containing systems. In muon capture for H_2+CO, H_2+CO_2, H_2+COS, and H_2+CS_2, the muon capture number of each constituent atom can be obtained from total intensity of muonic Lyman X-ray series of atoms. Taking the ratio of muon capture number of each constituent atom, relative muon capture probability (muon capture ratio) is deduced.

In this study, following transition series were applied for determination of the muon capture numbers, the sum of transition series (2-1) to (4-1) for carbon atom, the sum of (2-1) to (5-1) for oxygen atom, and the sum of (2-1) to (7-1) for sulfur atom. Muon capture ratio: A(C/O), A(S/O), A(S/C), for H_2+CO, H_2+CO_2, H_2+COS, and H_2+CS_2, samples are described in Table 3-22 (from prompt spectra) and Table 3-23 (from delayed spectra), respectively.

Table 3-22 Muon capture ratio: A(C/O), A(S/O), A(S/C), for H_2+CO, H_2+CO_2, H_2+COS, and H_2+CS_2 samples (derived from prompt regions of muonic X-ray spectra).

Sample	Muon capture ratio	Sample	Muon capture ratio
H_2+CO , 99 kPa	A(C/O)	H_2+COS , 99 kPa	A(C/O)
det-2	0.370 ± 0.027	det-2	0.637 ± 0.049
det-3	0.590 ± 0.068	det-4	0.396 ± 0.053
det-4	0.433 ± 0.043	det-5	0.513 ± 0.044
average	0.465 ± 0.028	average	0.515 ± 0.028
H_2+CO , 50 kPa	A(C/O)		
det-2	0.345 ± 0.062		
det-3	0.791 ± 0.222	H_2+COS , 99 kPa	A(S/O)
det-4	0.360 ± 0.101	det-4	1.318 ± 0.176
average	0.498 ± 0.084	det-5	2.020 ± 0.186
H_2+CO	A(C/O)	average	1.669 ± 0.128
†average	0.475 ± 0.027		
		H_2+COS , 99 kPa	A(S/C)
		det-4	3.329 ± 0.568
H_2+CO_2 , 99 kPa	A(C/O)	det-5	3.937 ± 0.432
det-2	0.401 ± 0.029	average	3.633 ± 0.357
det-3	0.663 ± 0.075		
det-4	0.433 ± 0.046		
average	0.499 ± 0.031		
H_2+CO_2 , 50 kPa	A(C/O)	H_2+CS_2 , 99 kPa	A(S/C)
det-2	0.434 ± 0.056	det-4	3.876 ± 0.348
det-3	0.589 ± 0.160	det-5	3.571 ± 0.210
det-4	0.546 ± 0.131	average	3.723 ± 0.203
average	0.523 ± 0.071		
H_2+CO_2	A(C/O)		
††average	0.508 ± 0.028		

† Average value of H_2+CO, 99 kPa and H_2+CO, 50 kPa

†† Average value of H_2+CO_2, 99 kPa and H_2+CO_2, 50 kPa

Table 3-23 Muon capture ratio: A(C/O), A(S/O), A(S/C), for H_2+CO, H_2+CO_2, H_2+COS, and H_2+CS_2 samples (derived from delayed regions of muonic X-ray spectra).

Sample	Muon capture ratio	Sample	Muon capture ratio
H_2+CO , 99 kPa	A(C/O)	H_2+COS , 99 kPa	A(C/O)
det-2	0.658 ± 0.055	det-2	0.464 ± 0.037
det-3	0.752 ± 0.066	det-4	0.607 ± 0.113
det-4	0.538 ± 0.039	det-5	0.512 ± 0.040
average	0.649 ± 0.032	average	0.527 ± 0.042
H_2+CO , 50 kPa	A(C/O)		
det-2	0.616 ± 0.084		
det-3	0.593 ± 0.098	H_2+COS , 99 kPa	A(S/O)
det-4	0.571 ± 0.073	det-4	1.731 ± 0.834
average	0.593 ± 0.049	det-5	1.554 ± 0.257
H_2+CO	A(C/O)	average	1.643 ± 0.436
†average	0.632 ± 0.027		
		H_2+COS , 99 kPa	A(S/C)
		det-4	2.855 ± 1.378
H_2+CO_2 , 99 kPa	A(C/O)	det-5	3.037 ± 0.512
det-2	0.724 ± 0.071	average	2.946 ± 0.735
det-3	0.699 ± 0.067		
det-4	0.546 ± 0.047		
average	0.656 ± 0.036		
H_2+CO_2 , 50 kPa	A(C/O)	H_2+CS_2 , 99 kPa	A(S/C)
det-2	0.530 ± 0.084	det-4	4.547 ± 0.480
det-3	0.710 ± 0.101	det-5	5.618 ± 0.253
det-4	0.657 ± 0.081	average	5.083 ± 0.272
average	0.632 ± 0.051		
H_2+CO_2	A(C/O)		
††average	0.647 ± 0.030		

† Average value of H_2+CO, 99 kPa and H_2+CO, 50 kPa

†† Average value of H_2+CO_2, 99 kPa and H_2+CO_2, 50 kPa

3.5 Discussion I: Descripsion of the muon capture ratio by LMM model

In this section, by using the LMM model, the number of atomic electrons affecting muon capture phenomenon were deduced from the muon capture ratios.

3.5-1 Comparison of experimental and calculation

First, the experimental muon capture ratios were compared with the model proposed by Fermi-Teller [4], Petrukhin [14] and Daniel [17] (Table.3-24). Although these models reproduce our experimental results partially, they still have not been able to explain a chemical effect generally (e.g. the difference of *A*(C/O) between CO and CO_2).

Table 3-24 Muonic X-ray intensity ratio of Z_1 to Z_2 ($A(Z_1/Z_2)$) for CO, CO_2, COS, and CS_2 samples.

	experimental			Z-low [4]	Petrukhin [14]	Daniel [17]
A(C/O)						
CO	0.753	±	0.021	0.75	0.82	0.74
CO_2	0.549	±	0.023	⋮	⋮	⋮
COS	0.513	±	0.015	⋮	⋮	⋮
A(S/C)						
COS	2.373	±	0.095	2.67	1.86	2.49
CS_2	3.352	±	0.091	⋮	⋮	⋮
A(S/O)						
COS	1.215	±	0.044	2.00	1.52	1.84

The LMM model is the most reliable semi empirical model for explaining muon capture probability [23,26]. In the LMM model, the muon capture process is considered as follows. First, the muon is interacted with the electron on a molecular orbital and forms large muon molecular orbital, and then, muon moves to individual atomic orbitals (i.e. the muon is captured by the atom). The probability of transition from molecular orbital to atomic orbital is strongly influenced by the distribution of covalent electrons on molecular orbital. Another muon capture process is also possible, muon is interacted with the atomic orbital electron directly, and forms muon atomic orbital dilectly. It is known that the LMM model with Imanishi's method which was developed for pionic atom [25,26] well reproduces an experimental result in molecules which consist of light elements. In this thesis, Imanishi's method was applied, and the electron number participating in the muon capture process were optimized.

In this model, muon capture ratio of carbon atom to oxygen atom can be expressed as formula (3-4). This is derived from the formula (1) and (2) of Imanishi's method [26]. The parameter ω is expressed by m_C and m_O. Although ionicity parameter of chemical bond (σ) is also involved in that method, this is not adopted since chemical bond between carbon and oxygen atoms can be regarded as almost pure covalent bond (σ=0) [53].

$$A(C/O) = \frac{n_C + \nu \times \dfrac{m_C}{m_C + m_O}}{n_O + \nu \times \dfrac{m_O}{m_C + m_O}} \qquad (3\text{-}4)$$

where n_C and n_O are the number of localized electrons concerning the muon capture on carbon atom and oxygen atom such as the lone pair on Lewis formula. The number of covalent electrons between carbon and oxygen atom are represented as v. The parameters n_C, n_O and v corresponds the probabilities of direct muon capture on carbon atom, direct muon capture on oxygen atom and muon capture on molecular orbital, respectively. The captured muon on molecular orbitals moves to carbon and oxygen atoms, depending on the parameters m_C and m_O. These parameters mean the number of electrons that contribute to muon de-excitation by Auger processes. Based on Imanishi's discussion, total electron number except 1s orbital electrons having large binding energy is applied the value of m_C and m_O. It was assumed that the binding energy of 1s electron was the constant regardless of the molecular structure. Also, formula (3-4) can be applied in a case of S/O and S/C. In this case, the parameter m_S is difined as the number of valence electrons on sulfur atom (except for 1s, 2s and 2p orbital electrons having large binding energy).

The estimation results of muon capture ratio: A(C/O), A(S/C), and A(S/O), which were calculated by formula (3-4) were summarized in Table 3-25. In the case of A(C/O), parameters of the LMM model can be determined from Lewis structure formula. For CO molecule, n_C is the number of the electrons which constitute the lone pair on carbon atom, n_O is that on oxygen atom, m_C is the number of total electrons belonging to L shell (2s, 2p) on carbon atom, and m_O is that on oxygen atom. v is the number of covalent electrons between carbon atom and oxygen atom. Therefore, they can be considered as n_C=2.0, n_O=2.0, m_C=4.0, m_O=6.0 and v=6.0 (first row of A(C/O) in Table 3-25). The calculation result well reproduced the experimental muon capture ratio, but slightly overestimation. Parameters for CO_2 were also estimated from Lewis structure formula as n_C=0, n_O=4.0, m_C=4.0, m_O=6.0 and v=4.0 (second row of A(C/O) in Table 3-25). In the same manner as the case of CO_2, parameters for COS were determined;

n_C=0.0, n_O=4.0, m_C=4.0, m_O=6.0 and v=4.0 from Lewis formula (third row of A(C/O) in Table 3-25). The calculation results were quite lower than the experimental results in CO_2 and COS. In the case of *A*(S/C), both COS and CS_2, it is appropriate for thinking as n_S=4.0, n_C=0, m_S=6.0, m_C=4.0 and v=4.0 from Lewis structure formula (first and second rows of *A*(S/C) in Table 3-25). The calculation results were higher than the experimental result for COS and CS_2. In the same manner as the case of *A(*C/O), parameters of the LMM model for A(S/O) were determined for COS molecule. Numbers of electrons which concern the muon capture phenomena are deduced as n_S=4.0, n_O=4.0, m_S=6.0, m_O=6.0 and v=4.0 from Lewis formula (first row of *A*(S/O) in Table 3-25). The calculation result was comparatively close to the experimental result, but didn't match completely.

Table 3-25 Comparison of muon capture ratios *A*(C/O), *A*(S/C), and *A*(S/O) between experimental and LMM model estimation (caluclation). The parameters which were estimated from Lewis structure formula are given in the row of each section.

	experimental			calculation	n_C	n_O	n_S	m_C	m_O	m_S	v
A(C/O)											
CO	0.753	±	0.021	0.79	2.0	2.0		4.0	6.0		6.0
CO_2	0.549	±	0.023	0.25	0.0	4.0		4.0	6.0		4.0
COS	0.513	±	0.014	0.25	0.0	4.0		4.0	6.0		4.0
A(S/C)											
COS	2.373	±	0.095	4.00	0.0		4.0	4.0		6.0	4.0
CS_2	3.352	±	0.091	4.00	0.0		4.0	4.0		6.0	4.0
A(S/O)											
COS	1.215	±	0.044	1.00		4.0	4.0		6.0	6.0	4.0

3-5-2 Optimization of muon capture ratio: *A*(C/O), *A*(S/C), and *A*(S/O) for CO, CO_2, COS and CS_2 by using the LMM model

In this section, the parameters of LMM model were optimized to reproduce experimental result. The experimental muon capture ratios were fitted by the LMM model, and the electron number which contributes to muon capture phenomenon were quantified.

In optimizing the parameters for LMM model (n_C, n_O, n_S, m_C, m_O, m_S, v), the following four conditions were assumed. 1) an electron lone pair on oxygen atom in CO_2, and COS doesn't contribute to muon capture (n_O=2.0), 2) an electron lone pair on sulfur atom in COS and CS_2 doesn't contribute to muon capture (n_S=2.0), 3) the contribution of oxygen atom in CO_2 and COS are same (m_O is same between CO_2 and COS), and 4) the contribution of carbon atom in CO_2, COS and CS_2 are same (m_C is same among CO_2, COS, and CS_2). The first assumption is based on the fact, that the oxygen atom in CO_2 molecule has two electron lone pairs and these binding energies are very different (-15.9 eV and -32.4 eV) [54]. Because the contribution of strongly binding electrons on the muon capture process is small in the concept of the LMM model [23], the higher binding energy electron pair may not concern muon capture process. Although the threshold value was set as -60 eV in the original theory, it was attempted to set the threshold value between the binding energy of two electron pairs. The second assumption is based on same reason as the first one. The third and forth assumptions were made to discuss the muon capture ratios in CO, CO_2, COS, and CS_2 consistently. Muonic X-ray structures of muonic oxygen in CO, CO_2, and COS, also supported the third assumption. The X-ray structures for these molecules were very similar, thus the contribution of oxygen atom for muon capture is supposed to be same among CO, CO_2, and COS. The value of m_C is set as m_C =4.0 (original condition in formula 3-4), the value of m_O is set as m_O =3.6. These values well reproduce the experimental results of A(C/O) for CO_2 and COS, and A(S/O) for COS. These assumptions were applied into calculation and n_C and m_S were adjusted as fitting parameters. The results were summarized in Table 3-26.

Remarkablelly, the calculation results reproduced the experimental muon capture ratios: A(C/O), A(S/C), and A(S/O), for all samples, under the assumption (n_O =2.0, n_S =2.0, m_C =4.0, and m_O =3.6). This result implies the number of electrons affecting the muon capture could be estimated by the LMM model in partry. The n_C value in the optimal A(C/O) for CO was not zero (n_C =0.4), whereas that for other molecules were completely zero. That means, in a case of a muon captured by carbon atom in CO molecule, muon interacts with atomic electron of carbon atom, that is, captured muon is influenced by lone pair electrons on the carbon atom. The m_S value in the optimal A(S/C) for CS_2 was 7.6; this is larger than the number of valence electrons of sulfur atom: 6. The large diameter of sulfur atom might be concerned to this fact. However, current LMM model doesn’t has correction parameter for atomic size, the contribution of size of muon capturing atom has not been estimated.

Table 3-26 Comparison of calculation results for *A*(C/O), *A*(S/O), and *A*(S/C). All calculations were performed under the assumption (n_O=2.0, n_S=2.0, m_O is same between CO, CO_2 and COS, m_C is same among CO, CO_2, COS, and CS_2).

	experimental	optimal	n_C	n_O	n_S	m_C	m_O	m_S	v
A(C/O)									
CO	0.753 ± 0.021	0.73	0.4	2.0		4.0	3.6		6.0
CO_2	0.549 ± 0.023	0.54	0.0	2.0		4.0	3.6		4.0
COS	0.513 ± 0.014	0.54	0.0	2.0		4.0	3.6		4.0
A(S/C)									
COS	2.373 ± 0.095	2.37	0.0		2.0	4.0		5.0	4.0
CS_2	3.352 ± 0.091	3.35	0.0		2.0	4.0		7.6	4.0
A(S/O)									
COS	1.215 ± 0.044	1.17		2.0	2.0		3.6	5.0	4.0

3.6 Result III: Muonic X-ray structure

3.6-1 Muonic X-ray structures of pure gas sample

The initial quantum states of captured muons influence the muon cacade paths, and are reflected in rerlative intensity ratio to K_α muonic X-ray. Muonic X-ray intensities normalized by K_α: (2-1) X-ray intensity of carbon, oxygen, and sulfur atoms are summarized in Table 3-27 ~ 3-31, for CO, CO_2, COS (10 kPa and 18 kPa), and CS_2 samples. Same as the result for capture ratio, muonic X-ray structures for COS molecules with two density conditions show the same ratios both muonic carbon, oxygen, and sulfur atoms. The rate of electron refilling is strongly influenced by the pressure of a sample gas [27,29,30], as a results, muonic X-ray structure also different by the sample pressure. In this thesis, there were no pressure dependence on muonic X-ray structure between 18 and 10 kPa conditions, that means the formed muonic atoms can be regarded as an isolated system, and no electron refilling processes occur during muonic cascade. For the following discussions in this paper, the averaged value of muonic X-ray strucutre with two density conditions is applied.

There are no obvious difference on muonic X-ray structure for oxygen in CO, CO_2 and COS molecules. Although muonic X-ray intensity ratios in μO(4-1) and μO(5-1) for COS sample with 18 kPa are slightly different from others, both Lyman and Balmer X-ray structures among these molecules are very similar each other. That means the initial quantum levels of captured muons were very similar, thus, the muon cascade process in muonic oxygen atoms among these three carbon oxides were also comparable.

On the other hand, clear difference was found in muonic X-ray structures for carbon atoms among these carbon oxides; intensities of higher transition series such as (3-1) and (4-1) in CO are much lower than these in CO_2, whereas these from CO_2 and COS well agree each other. As mentioned, muonic X-ray structure is strongly influenced by the initial quantum state of captured muon. The difference on muonic X-ray structure in muonic carbon is the evidence that the initial quantum state of muonic carbon in CO molecule is clearly different from that in CO_2 and COS molecules.

Table 3-27 Muonic X-ray structure normalized by K_α intensity (for CO 40 kPa).

	Muonic X-ray intensity: per K_α ×100					
	det-1			det-2		
Lyman series						
μC(2-1)	100	±		100	±	
μC(3-1)	7.33	±	0.58	9.05	±	0.56
μC(4-1)	2.27	±	0.38	3.07	±	0.37
μC(5-1)	1.99	±	0.36	1.12	±	0.34
μC(6-1)	1.61	±	0.30	0.76	±	0.28
μC(7-1)	1.64	±	0.31	1.24	±	0.29
μC(>8-1)	3.52	±	0.47	2.37	±	0.47
μO(2-1)	100	±		100	±	
μO(3-1)	5.69	±	0.52	6.10	±	0.46
μO(4-1)	2.16	±	0.37	1.79	±	0.33
μO(5-1)	2.03	±	0.40	1.42	±	0.33
μO(6-1)	1.99	±	0.40	1.28	±	0.28
μO(7-1)	1.77	±	0.33	1.48	±	0.30
μO(8-1)	1.55	±	0.38	1.20	±	0.32
μO(>9-1)	1.63	±	0.51	0.92	±	0.43
Balmer series						
μC(3-2)				131.54	±	6.58
μC(4-2)				8.32	±	0.73
μC(5-2)				2.24	±	0.53
μC(6-2)				1.13	±	0.51
μC(>7-2)				2.27	±	0.52
μO(3-2)	99.85	±	5.07	105.19	±	4.33
μO(4-2)	6.96	±	0.48	7.18	±	0.48
μO(5-2)	2.32	±	0.27	2.79	±	0.28
μO(6-2)	2.88	±	0.31	2.20	±	0.25
μO(7-2)	2.39	±	0.28	1.74	±	0.26
μO(>8-2)	1.71	±	0.47	0.51	±	0.42

Table 3-28 Muonic X-ray structure normalized by K_α intensity (for CO_2 20 kPa).

	Muonic X-ray intensity: per K_α ×100					
	det-1			det-2		
Lyman series						
μC(2-1)	100	±		100	±	
μC(3-1)	17.66	±	2.11	15.03	±	1.79
μC(4-1)	6.27	±	1.38	8.31	±	1.28
μC(5-1)	4.46	±	1.36	3.67	±	1.12
μC(6-1)	3.45	±	1.24	3.37	±	1.07
μC(7-1)	8.11	±	2.10	9.75	±	2.08
μO(2-1)	100	±		100	±	
μO(3-1)	7.20	±	0.70	6.54	±	0.58
μO(4-1)	2.53	±	0.50	1.78	±	0.38
μO(5-1)	1.78	±	0.50	1.98	±	0.42
μO(6-1)	1.87	±	0.50	2.48	±	0.39
μO(7-1)	1.92	±	0.51	2.46	±	0.41
μO(8-1)	1.14	±	0.46	1.28	±	0.36
μO(>9-1)	-0.53	±	0.62	0.43	±	0.52
Balmer series						
μC(3-2)				124.52	±	9.71
μC(4-2)				7.90	±	2.07
μC(5-2)				4.76	±	1.88
μC(6-2)				4.73	±	1.81
μC(>7-2)				5.93	±	6.00
μO(3-2)	98.62	±	5.18	95.06	±	4.05
μO(4-2)	9.13	±	0.67	8.36	±	0.55
μO(5-2)	3.47	±	0.40	3.56	±	0.37
μO(6-2)	4.37	±	0.44	3.51	±	0.35
μO(7-2)	2.86	±	0.36	2.52	±	0.33
μO(>8-2)	1.05	±	0.43	1.33	±	0.52

Table 3-29 Muonic X-ray structure normalized by K_α intensity (for COS 18 kPa).

	Muonic X-ray intensity: per K_α ×100					
	det-1			det-2		
Lyman series						
μC(2-1)	100	±		100	±	
μC(3-1)	13.99	±	1.54	16.90	±	1.28
μC(4-1)	5.14	±	0.98	6.02	±	0.73
μC(5-1)	4.65	±	1.00	3.81	±	0.68
μC(6-1)	4.87	±	0.85	4.33	±	0.67
μC(7-1)	3.59	±	0.83	3.02	±	0.63
μO(2-1)	100	±		100	±	
μO(3-1)	6.69	±	0.81	7.36	±	0.64
μO(4-1)	4.02	±	0.72	4.47	±	0.58
μO(5-1)	3.71	±	0.76	4.83	±	0.64
μO(6-1)	3.73	±	0.75	3.01	±	0.48
μO(7-1)	2.75	±	0.60	2.77	±	0.50
μO(8-1)	2.49	±	0.70	1.74	±	0.47
μO(>9-1)	0.45	±	0.88	0.64	±	0.60
μS(2-1)	100	±		100	±	
μS(3-1)	11.40	±	2.23	10.39	±	1.88
μS(4-1)	5.54	±	1.96	5.31	±	1.92
μS(5-1)	5.05	±	2.06	3.67	±	1.70
μS(6-1)	2.64	±	2.06	5.04	±	1.68
μS(7-1)	4.19	±	2.08	2.95	±	1.59
μS(8-1)	2.03	±	1.95	4.17	±	1.71
μS(9-1)	7.01	±	4.32	3.02	±	1.58

Table 3-29 Muonic X-ray structure normalized by K_α intensity (for COS 18 kPa, continued).

	Muonic X-ray intensity: per K_α ×100	
	det-1	det-2
Balmer series		
μC(3-2)		110.29 ± 7.09
μC(4-2)		7.46 ± 1.27
μC(5-2)		5.11 ± 1.15
μC(6-2)		2.58 ± 1.06
μC(>7-2)		6.61 ± 1.14
μO(3-2)	106.13 ± 5.47	106.45 ± 4.45
μO(4-2)	9.83 ± 0.69	9.86 ± 0.63
μO(5-2)	4.33 ± 0.51	3.45 ± 0.37
μO(6-2)	4.48 ± 0.53	2.57 ± 0.33
μO(7-2)	3.13 ± 0.45	2.61 ± 0.34
μO(>8-2)	0.45 ± 0.39	0.59 ± 0.30
	1.00 ± 0.66	0.80 ± 0.43
μS(3-2)	107.95 ± 6.28	82.71 ± 4.04
μS(4-2)	10.34 ± 0.88	8.36 ± 0.61
μS(5-2)	4.22 ± 0.65	4.40 ± 0.46
μS(6-2)	3.93 ± 0.77	3.03 ± 0.45
μS(7-2)	2.29 ± 0.63	2.99 ± 0.49

Table 3-30 Muonic X-ray structure normalized by K_α intensity (for COS 10 kPa).

	Muonic X-ray intensity: per K_α ×100					
	det-1			det-2		
Lyman series						
μC(2-1)	100	±		100	±	
μC(3-1)	15.23	±	1.77	21.86	±	2.21
μC(4-1)	3.25	±	1.37	7.39	±	1.64
μC(5-1)	4.54	±	1.26	3.82	±	1.58
μC(6-1)	4.43	±	1.18	3.94	±	1.49
μC(7-1)	0.49	±	1.11	5.30	±	1.57
μO(2-1)	100	±		100	±	
μO(3-1)	6.07	±	1.14	7.60	±	1.29
μO(4-1)	2.21	±	1.04	0.82	±	1.14
μO(5-1)	3.01	±	1.13	1.43	±	1.22
μO(6-1)	1.50	±	1.09	2.72	±	1.24
μO(7-1)	1.64	±	1.10	2.88	±	1.26
μO(8-1)	-0.98	±	1.12	0.62	±	1.29
μO(>9-1)	0.79	±	1.15	0.71	±	1.29
μS(2-1)	100	±		100	±	
μS(3-1)	5.99	±	3.59	9.39	±	4.01
μS(4-1)	5.12	±	3.54	0.37	±	3.73
μS(5-1)	6.32	±	3.72	3.17	±	3.97
μS(6-1)	6.50	±	3.70	6.54	±	4.13
μS(7-1)	3.08	±	3.38	3.69	±	3.90
μS(8-1)	2.03	±	3.43	-2.05	±	3.78
μS(9-1)	9.25	±	3.71	7.62	±	4.11

Table 3-30 Muonic X-ray structure normalized by K_α intensity (for COS 10 kPa, continued).

	Muonic X-ray intensity: per K_α ×100	
	det-1	det-2
Balmer series		
μC(3-2)		71.10 ± 5.80
μC(4-2)		5.91 ± 1.48
μC(5-2)		5.19 ± 1.31
μC(6-2)		2.71 ± 1.20
μC(>7-2)		5.15 ± 1.21
μO(3-2)		119.48 ± 6.59
μO(4-2)	8.54 ± 0.93	8.06 ± 0.85
μO(5-2)	3.70 ± 0.74	4.37 ± 0.66
μO(6-2)	3.30 ± 0.73	3.73 ± 0.64
μO(7-2)	2.11 ± 0.70	3.39 ± 0.63
μO(8-2)		0.41 ± 0.55
μO(>9-2)		0.41 ± 0.55
μS(3-2)	95.09 ± 6.93	90.23 ± 6.82
μS(4-2)	7.58 ± 1.06	10.01 ± 1.27
μS(5-2)	5.67 ± 1.11	3.25 ± 1.17
μS(6-2)	6.02 ± 1.21	3.01 ± 1.25
μS(7-2)	4.02 ± 1.11	2.15 ± 1.20

Table 3-31 Muonic X-ray structure normalized by K_α intensity (for CS_2 20 kPa).

	Muonic X-ray intensity: per Kα ×100								
	det-2			det-4			det-5		
Lyman series									
μC(2-1)	100	±		100	±		100	±	
μC(3-1)	8.72	±	1.60	11.42	±	2.46	10.70	±	2.82
μC(4-1)	5.08	±	0.87	4.24	±	2.11	6.06	±	1.75
μC(5-1)	3.04	±	0.79	8.32	±	2.25	7.51	±	1.68
μC(6-1)	5.28	±	0.87	8.73	±	2.13	10.43	±	1.92
μC(7-1)	3.05	±	0.77						
μS(2-1)				100	±		100	±	
μS(3-1)				11.64	±	2.18	18.28	±	2.31
μS(4-1)				5.54	±	2.14	6.50	±	1.32
μS(5-1)				4.19	±	2.06	5.31	±	1.83
μS(6-1)				6.97	±	2.18	4.78	±	1.73
μS(7-1)				2.15	±	2.07	0.78	±	1.54
μS(8-1)				-0.65	±	2.04	1.31	±	1.52
Balmer series									
μC(3-2)	73.01		6.19				141.7	±	18.0
μC(4-2)	8.98		1.06				15.92	±	2.94
μC(5-2)	3.32		0.69						
μC(6-2)	4.48		0.36						
μS(3-2)				61.38	±	4.72	69.43	±	5.16
μS(4-2)				8.45	±	0.82	9.82	±	0.80
μS(5-2)				4.12	±	0.61	4.76	±	0.50
μS(6-2)				2.93	±	0.59	3.37	±	0.41
μS(7-2)				2.15	±	0.58	2.86	±	0.40
μS(8-2)				1.17	±	0.51	0.97	±	0.32

3.6-2 Muonic X-ray structures of hydrogen mixture sample

Muonic X-ray intensities normalized by K_α: (2-1) X-ray intensity of carbon, oxygen, and sulfur atoms are summarized in Table 3-32 ~ 3-43, for H_2+CO, H_2+CO_2, H_2+COS, and H_2+CS_2 samples. X-ray structures from delayed spectra were described in 3.6-3 (Table 3-32~ 3-37). X-ray structures from prompt spectra were described in 3.6-4 (Table 3-38~ 3-43).

3.6-3 Muonic X-ray structures derived from delayed spectra

Muonic x-ray structures for delayed spectra were determined. The intensity ratio of (3-1), (4-1), (3-2), and (4-2), to (2-1) for carbon, (3-1), (4-1), (5-1), (3-2), (4-2), and (5-2), to (2-1) for oxygen, (3-1), (4-1), (5-1), (6-1), (7-1), (8-1), (3-2), (4-2), (5-2), (6-2), (7-2), and (8-2), to (2-1) for sulfur, were summarized in Table 3-32~ 3-37. These are reflected the events attribute to muon transfer process only.

In all X-ray structures from delayed spectra, X-ray intensities of higher transition series; (3-1), (4-1) and much higher transitions, were much larger than the X-ray structure for pure gas experiments (described in Table 3-27 ~ 3-31). This implies, the muon goes on a different path in direct capture process and muon transfer process. That is, difference in initial quantum states of captured muon between direct capture process and muon transfer process appears in the each muonic X-ray structure.

Table 3-32 Muonic X-ray structure normalized by K_α intensity (for H_2+CO 99 kPa).

	Muonic X-ray intensity: per Kα ×100		
delayed	det-2	det-3	det-4
Lyman series			
μC(2-1)	100 ±	100 ±	100 ±
μC(3-1)	77.35 ± 12.03	73.56 ± 9.67	65.01 ± 9.77
μC(4-1)	49.40 ± 7.74	44.93 ± 6.51	54.28 ± 7.66
μO(2-1)	100 ±	100 ±	100 ±
μO(3-1)	53.29 ± 7.28	59.93 ± 10.21	61.66 ± 6.14
μO(4-1)	58.56 ± 7.87	61.77 ± 10.81	65.07 ± 6.44
μO(5-1)	35.68 ± 6.01	47.25 ± 9.56	41.32 ± 4.76
Balmer series			
μC(3-2)	45.44 ± 9.26	31.50 ± 5.85	39.37 ± 8.74
μC(4-2)	17.87 ± 4.68	15.61 ± 3.47	22.77 ± 4.95
μO(3-2)	32.02 ± 4.54	40.95 ± 6.67	42.61 ± 8.14
μO(4-2)	12.95 ± 3.30	35.04 ± 4.86	24.84 ± 3.26
μO(5-2)	8.99 ± 2.46	14.35 ± 2.82	13.47 ± 2.14

Table 3-33 Muonic X-ray structure normalized by K_α intensity (for H_2+CO 50 kPa).

	Muonic X-ray intensity: per Kα ×100								
delayed	det-2			det-3			det-4		
Lyman series									
μC(2-1)	100	±		100	±		100	±	
μC(3-1)	105.54	±	30.31	109.45	±	31.57	48.40	±	13.61
μC(4-1)	69.63	±	18.46	64.04	±	20.06	31.33	±	7.65
μO(2-1)	100	±		100	±		100	±	
μO(3-1)	55.07	±	11.16	53.79	±	15.05	63.69	±	10.10
μO(4-1)	71.68	±	13.32	51.57	±	15.28	62.46	±	9.97
μO(5-1)	44.32	±	10.41	24.91	±	12.86	48.26	±	9.01
Balmer series									
μC(3-2)	76.08	±	24.41	63.33	±	22.20	30.15	±	13.06
μC(4-2)	18.68	±	10.36	33.29	±	13.06	18.96	±	8.11
μO(3-2)	41.00	±	7.74	35.63	±	10.09	89.96	±	20.02
μO(4-2)	37.59	±	8.19	23.06	±	5.80	6.71	±	5.58
μO(5-2)	3.79	±	4.44	19.14	±	5.05	13.95	±	4.56

Table 3-34 Muonic X-ray structure normalized by K_{α} intensity (for H_2+CO_2 99 kPa).

	Muonic X-ray intensity: per Kα ×100		
delayed	det-2	det-3	det-4
Lyman series			
μC(2-1)	100 ±	100 ±	100 ±
μC(3-1)	82.03 ± 16.91	72.67 ± 13.41	79.08 ± 14.83
μC(4-1)	53.88 ± 10.90	54.78 ± 10.42	56.68 ± 10.31
μO(2-1)	100 ±	100 ±	100 ±
μO(3-1)	55.19 ± 6.91	59.77 ± 8.55	54.64 ± 5.02
μO(4-1)	70.18 ± 8.41	67.70 ± 9.56	56.70 ± 5.20
μO(5-1)	39.13 ± 5.86	45.16 ± 7.69	36.44 ± 3.79
Balmer series			
μC(3-2)	44.13 ± 12.58	38.43 ± 9.45	35.61 ± 12.81
μC(4-2)	16.58 ± 6.55	27.10 ± 6.37	13.36 ± 6.41
μO(3-2)	35.80 ± 4.60	44.58 ± 5.78	34.65 ± 6.28
μO(4-2)	14.97 ± 3.15	36.10 ± 4.17	24.41 ± 2.73
μO(5-2)	11.94 ± 2.43	13.69 ± 2.25	11.12 ± 1.62

Table 3-35 Muonic X-ray structure normalized by K_α intensity (for H_2+CO_2 50 kPa).

	Muonic X-ray intensity: per Kα ×100								
delayed	det-2			det-3			det-4		
Lyman series									
μC(2-1)	100	±		100	±		100	±	
μC(3-1)	90.26	±	34.18	111.57	±	31.92	82.92	±	21.12
μC(4-1)	68.12	±	22.82	64.83	±	20.45	31.09	±	9.11
μO(2-1)	100	±		100	±		100	±	
μO(3-1)	61.80	±	8.52	78.90	±	16.00	54.48	±	6.45
μO(4-1)	72.99	±	9.79	97.59	±	18.84	65.50	±	7.32
μO(5-1)	48.13	±	7.71	59.09	±	14.96	39.18	±	5.55
Balmer series									
μC(3-2)	64.21	±	26.61	50.61	±	19.98	47.30	±	19.51
μC(4-2)	37.41	±	16.09	36.05	±	13.69	25.74	±	10.68
μO(3-2)	31.54	±	4.95	34.63	±	9.91	47.78	±	11.65
μO(4-2)	16.69	±	5.06	40.36	±	6.94	13.91	±	3.71
μO(5-2)	11.17	±	3.05	18.87	±	4.45	16.76	±	3.00

Table 3-36 Muonic X-ray structure normalized by K_α intensity (for H_2+COS 99 kPa).

	Muonic X-ray intensity: per Kα ×100		
delayed	det-2	det-4	det-5
Lyman series			
μC(2-1)	100 ±	100 ±	100 ±
μC(3-1)	80.19 ± 13.16	34.82 ± 12.71	49.88 ± 6.95
μC(4-1)	63.23 ± 10.68	28.09 ± 12.64	28.93 ± 5.62
μO(2-1)	100 ±	100 ±	100 ±
μO(3-1)	52.20 ± 5.42	68.65 ± 20.34	40.66 ± 5.47
μO(4-1)	58.62 ± 5.93	58.38 ± 19.75	41.96 ± 5.71
μO(5-1)	32.14 ± 4.13	33.22 ± 18.02	27.66 ± 5.06
μO(6-1)		4.76 ± 16.95	
μS(2-1)		100 ±	100 ±
μS(3-1)		3.89 ± 20.71	65.14 ± 21.42
μS(4-1)		27.41 ± 22.61	11.61 ± 12.05
μS(5-1)		-22.72 ± 21.96	27.39 ± 18.86
μS(6-1)		6.79 ± 22.40	37.48 ± 18.77
μS(7-1)		-2.29 ± 22.48	18.35 ± 17.07
Balmer series			
μC(3-2)	57.37 ± 11.39		
μC(4-2)	16.72 ± 4.87		
μO(3-2)	37.00 ± 3.76		58.96 ± 6.20
μO(4-2)	19.04 ± 2.32		5.22 ± 2.37
μO(5-2)	6.66 ± 1.47		4.60 ± 2.14
μO(6-2)	0.51 ± 1.19		-1.11 ± 1.89
μS(3-2)		2.44 ± 3.67	-2.88 ± 2.61
μS(4-2)		13.63 ± 5.06	8.59 ± 2.86
μS(5-2)		4.73 ± 4.40	11.57 ± 3.43
μS(6-2)		16.40 ± 5.72	3.81 ± 2.85
μS(7-2)		-1.60 ± 4.62	3.97 ± 2.81

Table 3-37 Muonic X-ray structure normalized by K_α intensity (for H_2+CS_2 50 kPa).

	Muonic X-ray intensity: per Kα ×100		
delayed	det-2	det-4	det-5
Lyman series			
μC(2-1)	100 ±	100 ±	100 ±
μC(3-1)	76.90 ± 12.44	28.96 ± 12.45	47.02 ± 6.95
μC(4-1)	58.43 ± 9.75	31.29 ± 13.00	35.98 ± 6.09
μS(2-1)		100 ±	100 ±
μS(3-1)		47.97 ± 16.58	37.25 ± 7.15
μS(4-1)		10.61 ± 16.50	21.45 ± 4.75
μS(5-1)		21.00 ± 16.71	40.54 ± 7.83
μS(6-1)		35.28 ± 17.84	20.02 ± 6.44
μS(7-1)		32.31 ± 17.82	23.63 ± 6.47
μS(8-1)		22.36 ± 17.37	3.09 ± 5.52
Balmer series			
μC(3-2)	56.48 ± 11.10		
μC(4-2)	16.33 ± 4.88		
μS(3-2)		4.16 ± 2.79	1.98 ± 0.94
μS(4-2)		11.53 ± 3.52	2.48 ± 0.99
μS(5-2)		12.90 ± 3.87	3.00 ± 1.11
μS(6-2)		10.73 ± 3.83	0.79 ± 1.05
μS(7-2)		14.46 ± 4.26	-0.91 ± 1.08

3.6-4 Muonic X-ray structures derived from prompt spectra

Muonic x-ray structures for prompt spectra were determined. The intensity ratio of (3-1), (4-1), (3-2), and (4-2), to (2-1) for carbon, (3-1), (4-1), (5-1), (3-2), (4-2), and (5-2), to (2-1) for oxygen, (3-1), (4-1), (5-1), (6-1), (7-1), (8-1), (3-2), (4-2), (5-2), (6-2), (7-2), and (8-2), to (2-1) for sulfur, were summarized in Table 3-38~ 3-43.

In comparison with X-ray structures of H_2+CO at 99 kPa (Table 3-38) and H_2+CO at 50 kPa (Table 3-39), intensities of μC(3-1) and μC(3-1) are substantially different. Prompt spectrum consists of events from muon direct capture by atom and muon transfer, the difference is reflected the content ratio of the two events. The same can be said of the X-ray structure for H_2+CO_2.

Table 3-38 Muonic X-ray structure normalized by K_α intensity (for H_2+CO 99 kPa).

	Muonic X-ray intensity: per Kα ×100								
prompt	det-2			det-3			det-4		
Lyman series									
µC(2-1)	100	±		100	±		100	±	
µC(3-1)	64.11	±	9.13	37.69	±	8.95	55.95	±	11.75
µC(4-1)	58.07	±	7.97	20.27	±	4.84	29.60	±	6.31
µO(2-1)	100	±		100	±		100	±	
µO(3-1)	56.41	±	6.18	32.50	±	7.72	43.42	±	6.22
µO(4-1)	54.96	±	6.20	55.10	±	10.45	50.53	±	6.92
µO(5-1)	40.40	±	5.09	31.60	±	8.30	28.61	±	5.36
Balmer series									
µC(3-2)	46.24	±	9.33	53.53	±	8.64	23.86	±	9.70
µC(4-2)	9.74	±	4.01	11.96	±	3.66	12.01	±	6.14
µO(3-2)	24.38	±	3.07	47.59	±	10.97	6.00	±	11.80
µO(4-2)	18.32	±	2.46	16.68	±	3.79	11.44	±	3.09
µO(5-2)	8.54	±	1.58	14.94	±	2.92	5.09	±	2.05

Table 3-39 Muonic X-ray structure normalized by K_α intensity (for H_2+CO 50 kPa).

	Muonic X-ray intensity: per Kα ×100								
prompt	det-2			det-3			det-4		
Lyman series									
μC(2-1)	100	±		100	±		100	±	
μC(3-1)	9.72	±	15.08	21.98	±	20.72	106.31	±	66.11
μC(4-1)	17.77	±	7.23	29.34	±	10.92	57.67	±	30.05
μO(2-1)	100	±		100	±		100	±	
μO(3-1)	41.79	±	8.59	38.89	±	18.76	40.82	±	11.89
μO(4-1)	53.40	±	10.18	19.71	±	19.71	27.19	±	11.46
μO(5-1)	31.33	±	8.29	16.33	±	19.79	37.99	±	12.34
Balmer series									
μC(3-2)	53.52	±	14.81	45.95	±	15.11	51.09	±	48.78
μC(4-2)	5.09	±	6.26	13.39	±	7.74	53.55	±	33.98
μO(3-2)	22.88	±	4.84	37.04	±	26.62	9.49	±	26.92
μO(4-2)	12.73	±	4.15	26.46	±	11.74	0.74	±	6.28
μO(5-2)	3.10	±	3.05	8.97	±	5.72	7.96	±	4.98

Table 3-40 Muonic X-ray structure normalized by K_α intensity (for H_2+CO_2 99 kPa).

	Muonic X-ray intensity: per Kα ×100		
prompt	det-2	det-3	det-4
Lyman series			
μC(2-1)	100 ±	100 ±	100 ±
μC(3-1)	78.15 ± 11.50	52.51 ± 12.34	74.94 ± 17.80
μC(4-1)	52.05 ± 8.12	23.57 ± 6.30	49.99 ± 10.84
μO(2-1)	100 ±	100 ±	100 ±
μO(3-1)	45.25 ± 4.40	37.90 ± 6.30	40.88 ± 4.58
μO(4-1)	52.98 ± 5.08	48.10 ± 7.66	43.85 ± 4.90
μO(5-1)	36.23 ± 3.84	26.43 ± 5.73	25.75 ± 3.66
Balmer series			
μC(3-2)	55.19 ± 11.50	30.40 ± 7.87	25.21 ± 14.02
μC(4-2)	18.96 ± 5.60	12.45 ± 4.60	25.89 ± 9.94
μO(3-2)	22.76 ± 2.39	41.15 ± 7.78	10.65 ± 6.84
μO(4-2)	16.92 ± 1.89	26.92 ± 3.62	11.21 ± 2.09
μO(5-2)	6.57 ± 1.06	10.05 ± 1.83	4.12 ± 1.28

Table 3-41 Muonic X-ray structure normalized by K_α intensity (for H_2+CO_2 50 kPa).

	Muonic X-ray intensity: per Kα ×100								
prompt	det-2			det-3			det-4		
Lyman series									
μC(2-1)	100	±		100	±		100	±	
μC(3-1)	24.22	±	10.53	32.06	±	31.02	65.41	±	47.78
μC(4-1)	23.03	±	7.18	31.88	±	15.15	81.39	±	30.79
μO(2-1)	100	±		100	±		100	±	
μO(3-1)	41.97	±	6.06	33.00	±	10.39	36.53	±	8.18
μO(4-1)	48.68	±	6.78	31.81	±	10.66	33.79	±	8.18
μO(5-1)	36.97	±	5.94	22.31	±	10.04	29.16	±	8.01
Balmer series									
μC(3-2)	42.50	±	14.57	41.71	±	19.96	117.39	±	51.81
μC(4-2)	25.69	±	8.49	9.40	±	11.10	35.30	±	24.11
μO(3-2)	25.41	±	3.71	15.52	±	14.53	-0.60	±	-18.25
μO(4-2)	13.15	±	2.73	20.32	±	6.43	-0.10	±	-4.37
μO(5-2)	10.27	±	2.32	7.30	±	3.09	3.39	±	3.25

Table 3-42 Muonic X-ray structure normalized by K_α intensity (for H_2+COS 99 kPa).

	Muonic X-ray intensity: per Kα ×100								
prompt	det-2			det-4			det-5		
Lyman series									
μC(2-1)	100	±		100	±		100	±	
μC(3-1)	55.51	±	10.00	75.93	±	23.79	42.73	±	11.68
μC(4-1)	35.95	±	4.83	69.96	±	19.76	48.19	±	6.70
μC(5-1)	8.09	±	2.80	36.76	±	12.52	13.32	±	3.82
μO(2-1)	100	±		100	±		100	±	
μO(3-1)	32.41	±	3.58	46.81	±	7.53	57.12	±	6.60
μO(4-1)	35.15	±	3.81	55.84	±	8.37	57.44	±	6.61
μO(5-1)	23.98	±	3.00	35.75	±	7.17	45.13	±	5.86
μO(6-1)				17.85	±	6.32	20.49	±	4.45
μS(2-1)				100	±		100	±	
μS(3-1)				19.31	±	8.34	44.72	±	9.88
μS(4-1)				4.23	±	8.05	16.67	±	5.76
μS(5-1)				25.23	±	9.60	26.04	±	8.55
μS(6-1)				32.80	±	10.36	21.63	±	7.89
μS(7-1)				5.23	±	8.47	31.90	±	8.56
μS(8-1)				16.53	±	9.25	13.05	±	6.96

Table 3-42 Muonic X-ray structure normalized by K_α intensity (for H_2+COS 99 kPa, continued).

	Muonic X-ray intensity: per Kα ×100		
prompt	det-2	det-4	det-5
Balmer series			
μC(3-2)	68.75 ± 8.94		
μC(4-2)	29.37 ± 4.36		
μC(5-2)	10.42 ± 2.66		
μC(6-2)	8.74 ± 0.91		
μO(3-2)	64.81 ± 5.66		80.20 ± 7.98
μO(4-2)	27.03 ± 3.65		19.12 ± 3.24
μO(5-2)	17.15 ± 1.98		8.90 ± 2.04
μO(6-2)	3.34 ± 1.09		0.34 ± 1.65
μO(7-2)	2.23 ± 1.03		
μS(3-2)		25.81 ± 4.50	40.58 ± 6.35
μS(4-2)		18.47 ± 3.73	10.85 ± 1.79
μS(5-2)		18.02 ± 3.95	11.24 ± 2.06
μS(6-2)		17.14 ± 4.03	4.83 ± 1.52
μS(7-2)		13.35 ± 3.83	1.93 ± 1.69

Table 3-43 Muonic X-ray structure normalized by K_{α} intensity (for H_2+CS_2 50 kPa).

	Muonic X-ray intensity: per Kα ×100								
prompt	det-2			det-4			det-5		
Lyman series									
μC(2-1)	100	±		100	±		100	±	
μC(3-1)	53.07	±	11.48	44.60	±	19.47	22.59	±	12.59
μC(4-1)	40.25	±	6.17	56.56	±	18.84	41.17	±	7.50
μC(5-1)	12.26	±	3.98						
μS(2-1)				100	±		100	±	
μS(3-1)				25.07	±	7.29	39.11	±	7.07
μS(4-1)				29.46	±	8.18	14.96	±	4.06
μS(5-1)				24.95	±	7.81	26.73	±	6.49
μS(6-1)				23.63	±	7.82	18.91	±	5.67
μS(7-1)				19.11	±	7.56	19.45	±	5.60
μS(8-1)				16.83	±	7.44	-4.45	±	-3.87
Balmer series									
μC(3-2)	68.92	±	10.47						
μC(4-2)									
μS(3-2)				31.23	±	4.41	41.24	±	4.90
μS(4-2)				12.04	±	3.00	18.38	±	2.22
μS(5-2)				7.29	±	3.10	6.29	±	1.43
μS(6-2)				6.94	±	3.26	6.73	±	1.30
μS(7-2)				9.37	±	3.46	4.83	±	1.24
μS(8-2)				3.62	±	3.23	0.64	±	1.01

3.7 Discussion II: Initial quantum state of captured muon

In this section, the calculation of muon cascade process was performed, to discuss the initial quantum state of captured muon quantitatively.

3.7-1 Cascade calculation for estimation of initial quantum state of captured muon

As mentioned, muons which are captured by an atom have very large principal quantum number and angular momentum quantum number. The muonic X-ray emissions depend on selection rule of Δl = ±1 (shown in Fig. 3-17), so the captured muons which have small angular momentum quantum numbers well emit X-rays of high transition series (such as K$_\delta$: (4-1), K$_\varepsilon$: (5-1) and much higher transitions), compared with the captured muons which have large angular momentum quantum numbers [5,55].

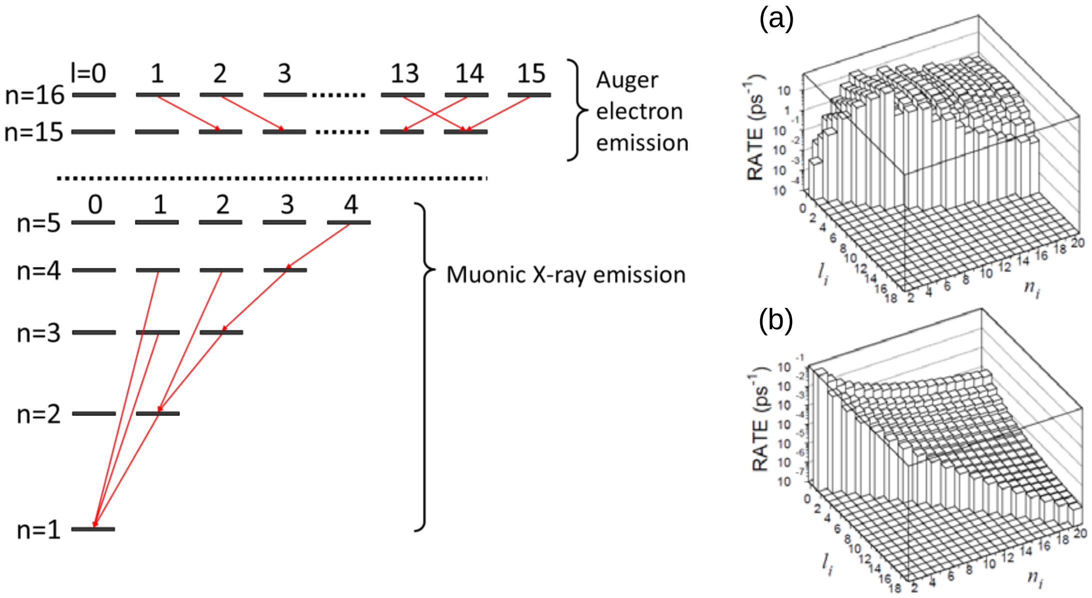

Fig.3-17 Schematic view of muon cascade, right images shows the rates of (a) radiative, and (b) Auger de-excitation in muonic hydrogen.

Muonic X-ray emission patterns can be estimated, if the initial quantum state of capture muon can be known. For this purpose, the most reliable calculation code in the research field of the muonic atom cascade [11] is applied. This calculation program simulates de-excitation rate of the captured muon based on a hydrogen type wave function. Since interaction of the muon in the cascade process is known [56], the muonic X-ray emission pattern can be reproduced by the calculation, as long as the muonic atom is isolated. In this code, principal parameters for calculation are follows.

(1) Atomic parameters

- Atomic number: Z
- Mass number: A
- Binding energies for K, L, M shell electrons: BE
- Effective charge of nucleus for Z-1 atom: ZS
- Electron refilling rate to K shell: KWD

(2) Muonic principal quantum number at the start of calculation: n

(3) Existence of electron refilling for L, and M shells.

If set the electron refilling don’t exsist, L and/or M shell electrons are dpleted by muon Auger transitions and never refilled. Set the electoron refilling exsists, L and/or M shell electrons are not dpleted.

(4) Number of orbital electrons at the start of calculation: ne

(5) Correction parameter for angular momentum distribution of captured muon: α

The angular momentum distribution of captured muon P_l is described as $P_l = (2l+1)e^{\alpha l}$. When α is equal to 0, P_l becomes statistical distribution [57-59].

3.7-2 Optimization of cascade calculation results for muon capture in carbon, oxygen and sulfur atoms.

In the section, cascade calculations were performed under various assumptions for initial state of the muon, and the muonic X-ray emission pattern (muonic X-ray structure) which the most reproduce experimental results were found. That is, the most reliable initial quantum state of captured muon was estimated.

In this thesis, muonic principal quantum number 16 (n=16) was set to the initial condition. Though, the muon may be captured in more higher principal quantum number state in the initial stage of the capture process, this condition is most reliable condition for starting calculation [33]. BE and ZS were taken from references [53,54]; energies of orbital electrons were calculated based on slater-low. Electron refilling rate to K, L, M shells were neglected, because all experiments were performed at the condition can be regarded as isolated state. At the start of calculation, the frequency of muon-electron interactions (Auger process) reflect to the number of remaining electrons, that is *ne*. It is considered that the muonic atom lost its atomic electrons at n=16 already, because the muon is captured in more highly excited state and the electrons are ejected by Auger transition. It is also expected that the electrons in muonic atom refilled from neighbor atoms in the molecule. The *ne* and α were treated as variables on this calculation. To mention other parameters, intensity of multipole transitions was set original condition.

Cascade calculation result was optimized to make the difference of between experiment and calculation muonic Lyman and Balmer X-ray structures (χ^2-value) both for muonic carbon and oxygen into the minimum. Only the result of Lyman X-ray structure was optimized for muonic sulfur. Average value of muonic X-ray structures for CO, CO_2, COS, and CS_2; summarized in Table 3-27 ~ 3-31, were applied in the optimization, and summarized in Table 3-44 ~ 3-46. The χ^2-values were calculated with the same method of previous literature [33]. Square sum of the subtraction of the experimental values and the calculated values, for CO, CO_2, COS, and CS_2, with varying *ne* and *α*, were deduced, and then determined the minimum χ^2 values (χ^2_{min}) as the optimimal condition of calculation. The summary of the calculation was shown in Table 3-47 ~ 3-49. Representative of calculation results for χ^2_{min} is shown in Fig. 3-18 (μO in CO_2). The errors of the calculation values were obtained from χ^2 contour plot in the *α*-*ne* plane, error range of the optimal *α* and *ne* values were set as 1σ ($\chi^2 = \chi^2_{\text{min}} + 1$) contour areas. Comparison of experimental and calcration results for μO in CO_2 are shown in Fig. 3-19.

Table 3-44 Muonic X-ray structure of muonic carbon (μC) for CO, CO_2, COS, and CS_2 molecules, the values are average of each detector and pressure (18 kPa nad 10 kPa for COS).

	Muonic X-ray intensity: per Kα ×100			
Transition	CO	CO_2	COS	CS_2
Lyman series				
μC(2-1)	100 ±	100 ±	100 ±	100 ±
μC(3-1)	8.19 ± 0.40	16.35 ± 1.38	16.49 ± 0.82	10.28 ± 1.36
μC(4-1)	2.67 ± 0.27	7.29 ± 0.94	5.49 ± 0.53	5.13 ± 0.96
μC(5-1)	1.56 ± 0.25	4.07 ± 0.88	4.21 ± 0.52	6.29 ± 0.97
μC(6-1)	1.18 ± 0.21	3.41 ± 0.82	4.46 ± 0.47	8.15 ± 1.00
Balmer series				
μC(3-2)	131.5 ± 6.6	124.5 ± 9.7	97.1 ± 4.5	73.0 ± 6.2
μC(4-2)	8.32 ± 0.73	7.90 ± 2.07	6.93 ± 0.96	8.98 ± 1.06
μC(5-2)	2.24 ± 0.53	4.76 ± 1.88	5.14 ± 0.86	3.32 ± 0.69
μC(6-2)	1.13 ± 0.51	4.73 ± 1.81	2.62 ± 0.80	4.48 ± 0.36

Table 3-45 Muonic X-ray structure of muonic oxygen (μO) for CO, CO_2, and COS, molecules, the values are average of each detector and pressure (18 kPa nad 10 kPa for COS).

	Muonic X-ray intensity: per Kα ×100		
Transition	CO	CO_2	COS
Lyman series			
μO(2-1)	100 ±	100 ±	100 ±
μO(3-1)	5.90 ± 0.35	6.87 ± 0.46	6.96 ± 0.44
μO(4-1)	1.97 ± 0.25	2.16 ± 0.31	3.32 ± 0.40
μO(5-1)	1.73 ± 0.26	1.88 ± 0.33	3.58 ± 0.43
μO(6-1)	1.63 ± 0.24	2.17 ± 0.32	2.94 ± 0.39
μO(7-1)	1.63 ± 0.22	2.19 ± 0.33	2.59 ± 0.36
μO(8-1)	1.37 ± 0.25	1.21 ± 0.29	1.34 ± 0.38
Balmer series			
μO(3-2)	102.5 ± 3.3	96.8 ± 3.3	110.7 ± 3.1
μO(4-2)	7.07 ± 0.34	8.75 ± 0.43	9.32 ± 0.38
μO(5-2)	2.55 ± 0.19	3.52 ± 0.27	3.94 ± 0.27
μO(6-2)	2.54 ± 0.20	3.94 ± 0.28	3.52 ± 0.26
μO(7-2)	2.06 ± 0.19	2.69 ± 0.24	2.83 ± 0.24
μO(8-2)	1.11 ± 0.31	1.19 ± 0.34	0.41 ± 0.18

Table 3-46 Muonic X-ray structure of muonic sulfur (μS) for COS, and CS_2, molecules, the values are average of each detector and pressure (18 kPa nad 10 kPa for COS).

	Muonic X-ray intensity: per Kα ×100	
Transition	COS	CS_2
Lyman series		
μS(2-1)	100 ±	100 ±
μS(3-1)	9.81 ± 1.28	14.96 ± 1.59
μS(4-1)	4.52 ± 1.21	6.02 ± 1.25
μS(5-1)	4.49 ± 1.20	4.75 ± 1.38
μS(6-1)	4.75 ± 1.20	5.88 ± 1.39
μS(7-1)	3.51 ± 1.17	1.47 ± 1.29

Table 3-47 Optimimal values of *ne* and *α* at *n*=16, case of muon captured by carbon atom. Results of COS are derived from average of 18 kPa and 10 kPa conditions.

	ne	α
CO	2.1 ± 0.0	$-0.12^{+0.01}_{-0.00}$
CO_2	$3.0^{+0.3}_{-0.8}$	$-0.25^{+0.06}_{-0.04}$
COS	$2.4^{+0.6}_{-0.1}$	$-0.31^{+0.03}_{-0.01}$
CS_2	$5.0^{+0}_{-0.2}$	-0.16 ± 0.2

Table 3-48 Optimimal values of *ne* and *α* at *n*=16, case of muon captured by oxygen atom. Results of COS are derived from average of 18 kPa and 10 kPa conditions.

	ne	α
CO	$6.1^{+0.5}_{-0.3}$	0.10 ± 0.01
CO_2	$6.8^{+0.6}_{-0.2}$	$0.06^{+0.01}_{-0.00}$
COS	$8.5^{+0.8}_{-0.9}$	0.08 ± 0.01

Table 3-49 Optimimal values of *ne* and *α* at *n*=16, case of muon captured by sulfur atom. Results of COS are derived from average of 18 kPa and 10 kPa conditions.

	ne	α
COS	$10.0^{+0}_{-4.3}$	$-0.06^{+0.01}_{-0.00}$
CS_2	$10.0^{+0}_{-5.0}$	$-0.11^{+0.01}_{-0.00}$

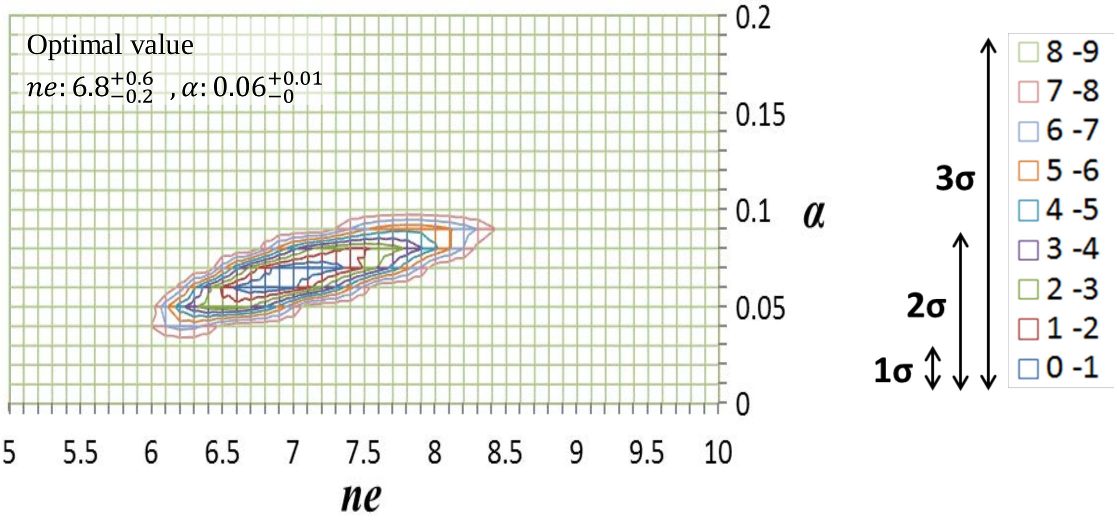

Fig. 3-18 χ^2 contour plot in the a-*ne* plane for μO in CO_2, The starting point of the calculation is at *n*=16. Right figure represents error ranges of the contour area.

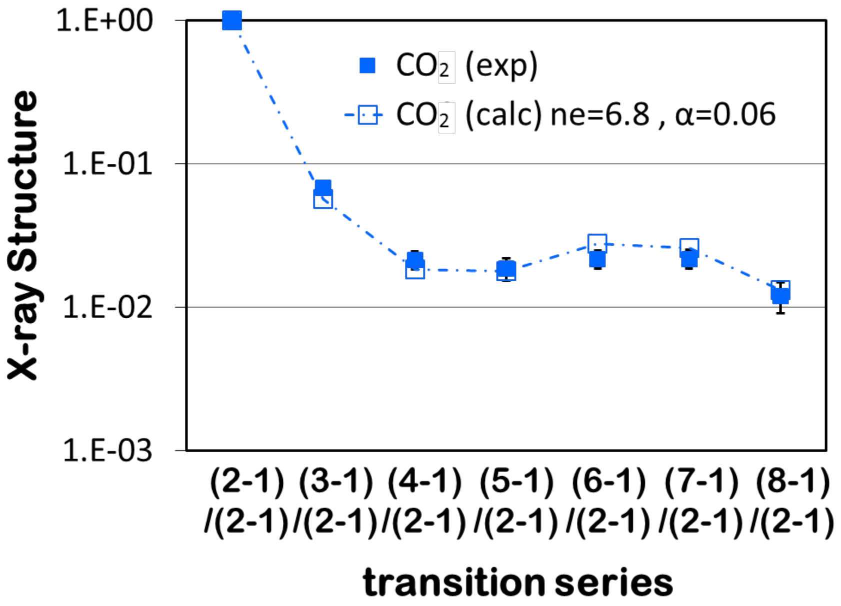

Fig. 3-19 Comparison of experimental and calcration results for μO in CO_2, Optimal value of ne and α is 6.8 and 0.06 respectively.

3.7-3 Distribution of initial angular momentum quantum number of the muons

Focusing on the table 3-47, the experimental muonic X-ray structures for muonic carbon atoms were well reproduced by the small *ne* and negative α conditions. That means the muonic atom has already lost its atomic electrons by muon-electron Auger process and remains only few electrons when the muon reach to n=16 state. That means the muon has captured on large principal quantum number state than n=16 state. From negative α conditions, the muon has small angular momentum quantum numbers. Angular momentum quantum number distribution of the muon captured by a carbon atom in CO, CO_2, COS, and CS_2 molecules at n=16 are shown in Fig.3-20. In the muon which is captured by a carbon atom, angular momentum quantum number of the muon in CO was similar to CS_2, but quite different from that in CO_2, and COS.

On the other hand, the muon cascade processes in muonic oxygen are completely different from these in muonic carbon. The experimental muonic X-ray structures were well reproduced by the large *ne* and large α conditions (see Table 3-48). When a muon reaches to muonic n=16 state in a oxygen atom, many electrons still remains in the atom though muon-electron Auger process should also occur in the muonic oxygen atom. As a possible reason of this result, the initial principal quantum number of muon is very close to n=16, case of the muon is captured by a oxygen atom. Another reason is also considered, electron refilling in the muonic oxygen atom occurs before the coulomb explosion of molecule [27,60]. From large α conditions, the muon exists relatively large angular momentum quantum state. Angular momentum quantum number distribution of muon captured by a carbon atom in CO, CO_2, and COS molecules at n=16 are shown in Fig.3-21. In a muon which is captured by an oxygen atom, the distributions of angular momentum quantum number of the muon are very similar among three samples, in contrast to the case of a muon is captured by a carbon atom.

The experimental muonic X-ray structures for muonic sulfur atoms were well reproduced by the large *ne* and small α conditions (see Table 3-49). Same as the muon which is captured by oxygen atom, many electrons might still remain in the muonic sulfur atom at *n*=16, or electron refilling in muonic sulfur atom might occur before the coulomb explosion. From negative α conditions, the muon which was captured by a sulfur atom in COS, and CS_2, had small angular momentum quantum numbers, but slightly larger than the muon which was captured by a carbon atom. This is shown in Fig.3-22.

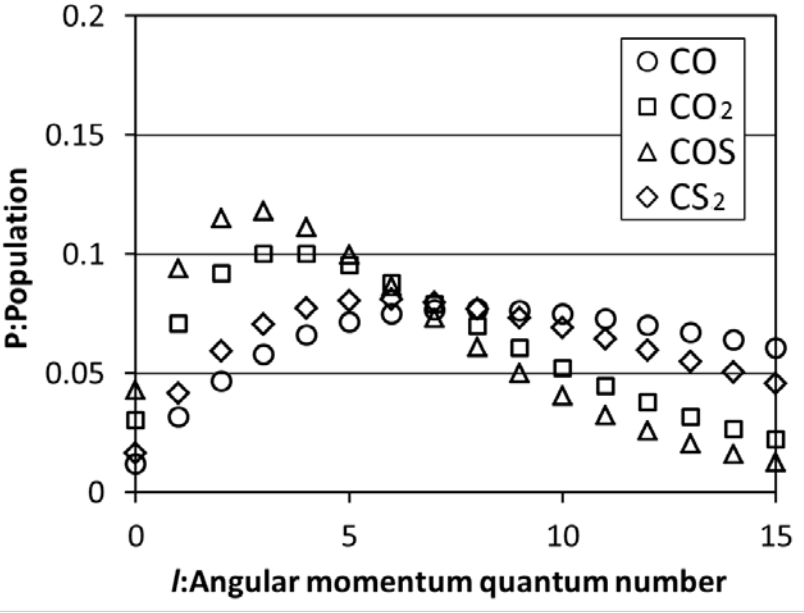

Fig.3-20 Angular momentum quantum number distribution of the muon which is captured by a carbon atom, at *n*=16.

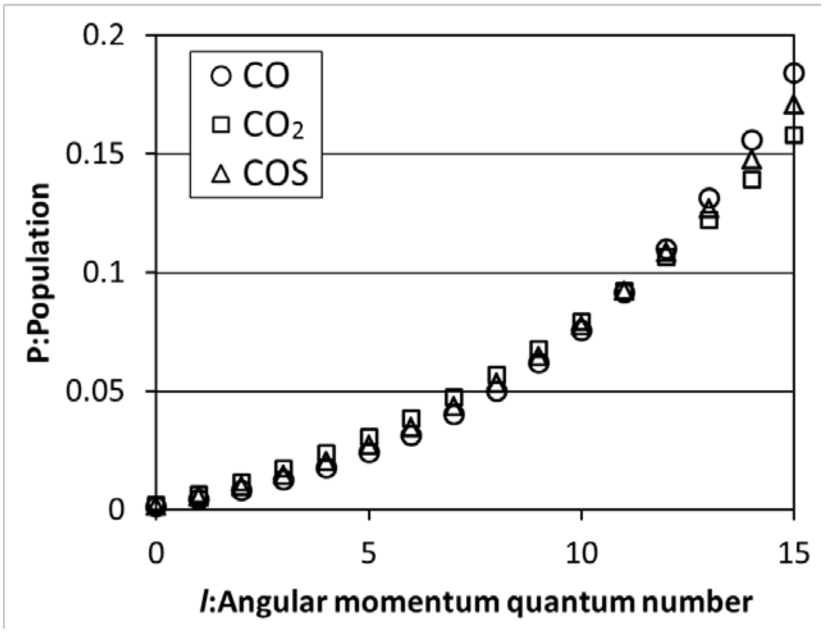

Fig.3-21 Angular momentum quantum number distribution of the muon which is captured by an oxygen atom, at *n*=16.

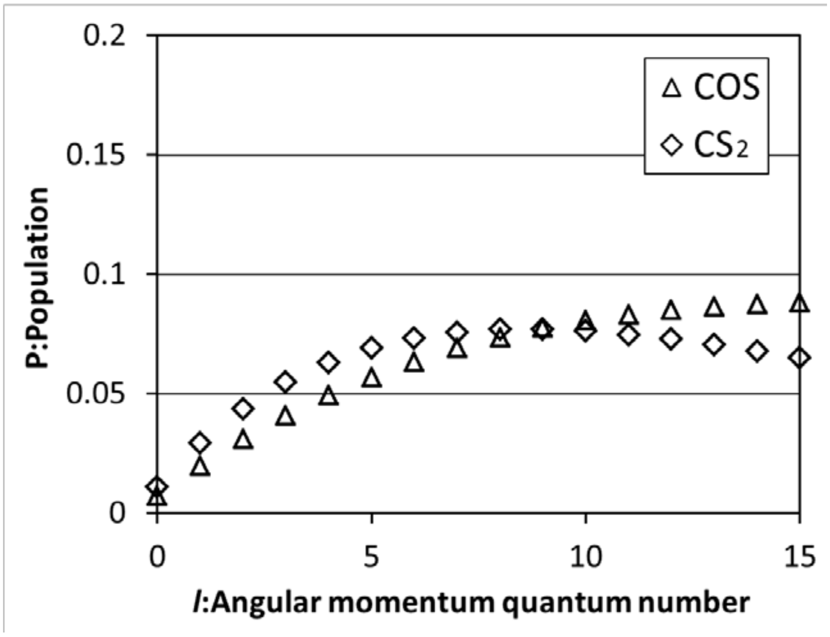

Fig.3-22 Angular momentum quantum number distribution of the muon which is captured by a sulfur atom, at *n*=16.

From above results, it can be concluded that the muon capture processes in a carbon atom among these molecules are strongly influenced by the electron state on the carbon atom, whereas these in an oxygen atom are hardly influenced by molecular structure.

Same as the result of muon capture ratio, there are very small difference on muon captured process by carbon and oxygen atom in CO_2 and COS molecules though sulfur atom is existed in COS molecule. From these results, it can be concluded that the contribution of sulfur atom in muon capture process in COS molecule is very small.

3.8 Discussion III: Estimation of electrons contributing muon capture on carbon atom in CO molecule

In this section, focusing on the muon capture ratio and the muonic X-ray structures for CO, CO_2, and COS, and discussed the chemical environmental effect on muon capture. When a muon was captured by a carbon atom in a CO molecule, both the muon capture probability and the initial angular momentum quantum number distribution of captured muon became quite different from other two molecules.

Muon capture ratio: A(C/O) for CO is 0.753, this is larger than that of CO_2 (0.549) and COS (0.513) [52] . If the relative number of muon which is captured by oxygen atom is same among CO, CO_2 and COS molecule, the number of muon which is captured by carbon atom in CO is larger than that in CO_2 by 0.271 (= 1 - 0.549/0.753), and that in COS by 0.319 (= 1 - 0.513/0.753). It is suggested that the carbon atom in CO molecule captures muon additional 30% more than carbon atom in CO_2 and COS molecules. This discussion doesn’t cover absolute number of captured muon but relative number of captured muon.

Strange behaviors on muon capture for CO molecule are also shown in initial angular momentum distribution (Fig. 3-20). Muons captured by carbon atom in CO molecule have quite large angular momentum than that in CO_2 and COS. These results may originate from the difference of atomic electron arrangement of carbon atom. While CO has an electron lone pair on the carbon atom, but CO_2 and COS have no lone pair. It is considered that the lone pair electrons on carbon atom in CO molecule strongly contribute to muon capture.

According to Guillarmod, final state of captured muon changes whether the muon interacts with s-orbital electron or p-orbital electron [61]. This report mentioned, muon tend to have large angular momentum when the muon interacts with p-orbital electron. Focus on molecular structure of samples, carbon atom in CO molecule has an electron lone pair and this consists of 2s and 2p electron hybrid, but carbon atom in CO_2 and COS molecules has no localized p-orbital electrons, just 1s electrons. Existence probability of p-orbital electrons on carbon atom in CO molecule was quite larger than that in CO_2 and COS, therefore, muons captured by carbon atom in CO molecule had large angular momentum quantum number. Also, in this report, initial angular momentum quantum number distribution of captured muon was calculated when the muon interacts with pure p-orbital electrons, the optimized α value at this condition was 0.056.

It is considered that the initial angular momentum of muon captured by carbon atom in CO molecule can be reproduced from that in CO_2 and COS molecules by using Guillarmod's estimation [61]. The contribution of p-orbital electrons appears in muon capture for carbon atom in CO molecule were defined as equation (3-5) and (3-6): added angular momentum quantum number distribution when the muon interacts with pure p-orbital electrons (α = 0.056, $\Sigma P_{l\ p\text{-}orbital}$ in Fig.3-22) to angular momentum quantum number distribution of muon captured by carbon atom in CO_2 and COS molecules. $\Sigma P_{l\ p\text{-}orbital}$ is multiplied by 0.271 for CO_2, 0.319 for COS. This hypothesis is based on the assumption that muons captured by carbon atom in CO_2 and COS molecules were not influenced by p-orbital electrons.

$$\sum P_{l\,CO2+p}^{\,C} = (1-0.271)\sum P_{l\,CO2}^{\,C} + 0.271\sum P_{l\,p-orbital} \qquad (3\text{-}5)$$

$$\sum P_{l\,COS+p}^{\,C} = (1-0.319)\sum P_{l\,COS}^{\,C} + 0.319\sum P_{l\,p-orbital} \qquad (3\text{-}6)$$

Where, $\Sigma P_l{}^C{}_{CO2}$ is initial angular momentum quantum number of muon captured by carbon atom in CO_2 molecule, $\Sigma P_l{}^C{}_{COS}$ is initial angular momentum quantum number of muon captured by carbon atom in COS molecule, $\Sigma P_{l\,p\text{-}orbital}$ is angular momentum quantum number distribution when a muon interacts with pure p-orbital electrons, respectively. $\Sigma P_l{}^C{}_{CO2+p}$ and $\Sigma P_l{}^C{}_{COS+p}$ are modified angular momentum quantum number distribution of muon captured by carbon atom in CO_2 and COS molecules, these include the influence of p-orbital electrons partially. Comparison of $\Sigma P_l{}^C{}_{CO2+p}$ and $\Sigma P_l{}^C{}_{COS+p}$ with $\Sigma P_l{}^C{}_{CO}$: angular momentum quantum number distribution of muon captured by carbon atom in CO molecule; are shown in Fig.3-23. The error is 1σ.

$\Sigma P_l{}^C{}_{CO2+p}$ (■) and $\Sigma P_l{}^C{}_{COS+p}$ (▲) were equal within 1σ error. For the following discussions, average value of $\Sigma P_l{}^C{}_{CO2+p}$ and $\Sigma P_l{}^C{}_{COS+p}$ is applied in this paper, it is written as $P_l{}^C{}_{Average}$ (♦) in Fig.4. $P_l{}^C{}_{Average}$ (♦) did not correspond to $\Sigma P_l{}^C{}_{CO}$ (○) within 1σ error, but almost corresponded within 3σ error, except for few components. These imply that our estimation is partially consistent with experimental result. In a case of muon captured by CO, CO_2 and COS molecules, oxygen atom captures same amount of muons among three molecules, on the other hand, the carbon atom in CO molecule captures muon additional 30% more than carbon atom in CO_2 and COS molecules. It could be concluded that the excess 30% attributes to the influence of lone pair electrons on carbon atom in CO molecule which have p-electron property.

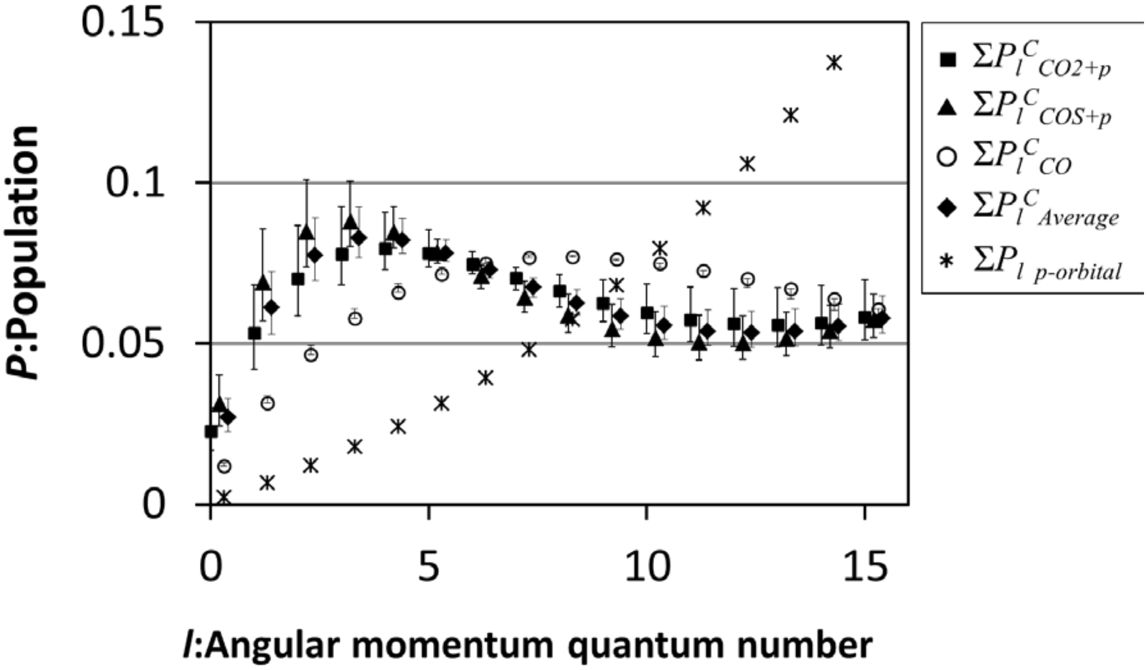

Fig.3-23 Modified angular momentum quantum number distribution of muon captured by carbon atom in CO_2 and COS (■:$\Sigma P_l{}^C{}_{CO2+p}$ and ▲:$\Sigma P_l{}^C{}_{COS+p}$); including the influence of p-orbital electrons partially. Angular momentum quantum number distribution of muon captured by carbon atom in CO molecule (○:$\Sigma P_l{}^C{}_{CO}$); average value of $\Sigma P_l{}^C{}_{CO2+p}$ and $\Sigma P_l{}^C{}_{COS+p}$ (♦: $P_l{}^C{}_{Average}$); angular momentum quantum number distribution when a muon interacts with pure p-orbital electrons (*:$\Sigma P_{l\ p\text{-}orbital}$) are also written in this figure.

As a different approach to this discussion, there is a possibility that the lone pair electrons directly give own angular momenta to captured muon during interaction among muon and electrons, because lone pair electrons on carbon atom in CO molecule is located in the outside of C-O axis and electrons are given large angular momenta. However, further discussion could not be conducted from our experimental results.

In conclusion, it has still been partly, but, the contribution of lone pair electrons on carbon atom in CO molecule to muon capture could be explained from two discussions: one is muon capture probability and the other is angular momentum quantum number distribution of captured muon, first time.

3.9 Discussion IV: Chemical environmental effect for muon capture in H_2+CO, H_2+CO_2 samples

As mentioned, muon capture processes are strongly influenced by the structure of the muon capturing molecule. In the case of the muon is directly captured by an atom, the muon capture probability of each atom (muon capture ratios) and the initial quantum state of the captured muon are strongly influenced by the chemical environment around muon capturing atom (molecular structure). Although there are many studies related to muon and/or pion capture process, the detail of chemical environmental effect on muon transfer process still have not been investigated enough.

In this section, focused on experiments in H_2+CO and H_2+CO_2 systems at different two density conditions (99 kPa and 50 kPa), the chemical environmental effect in muon transfer process was discussed by comparison of the muon capture ratio and muonic X-ray structure. Such low density conditions, muon transfer from excited state of muonic hydrogen atom ware completely suppressed and events of muon transfer from 1s state of muonic hydrogen atom can only be observed. Measurements for muonic X-rays from 50 kPa of hydrogen mixture gas samples had never been performed before in this work, and succeeded to determine muon capture ratio and muonic X-ray structure for these samples.

The muon capture ratios of carbon to oxygen: *A*(C/O), derived from delayed X-ray spectra were summarized in Table 3-50. In a case of H_2+CO, muon capture ratios: *A(C/O)* were 0.649 and 0.593 with 99 kPa and 50 kPa conditions respectively. The capture ratios agreed within statistical error and there were not sample density dependence on muon capture probability in muon transfer process. The average value of

99 kPa and 50 kPa conditions were adopted in following discussion. In case of H_2+CO_2 pressure dependence on muon capture ratios was also not observed. The averaged muon capture ratio of $A(\mathrm{C/O})_{CO2}$ were very similar to that of CO. From these result, when the muon transfers to CO and CO_2, the chemical environmental effect on muon capture ratio is quite small, though, more than 30% difference of muon capture ratio is observed between CO and CO_2 in direct capture [52].

Table 3-50 Muon capture ratio per atom:A(C/O) of H_2+CO (50 kPa, 99 kPa) and H_2+CO_2 (50 kPa, 99 kPa).

Sample	A(C/O)
H_2+CO , 99 kPa	0.649 ± 0.032
H_2+CO , 50 kPa	0.593 ± 0.049
Average (50 kPa and 99 kPa)	0.632 ± 0.027
Pure CO 40 kPa [52]	0.753 ± 0.021
H_2+CO_2 , 99 kPa	0.656 ± 0.036
H_2+CO_2 , 50 kPa	0.632 ± 0.051
Average (50 kPa and 99 kPa)	0.647 ± 0.030
Pure CO_2 20 kPa [52]	0.549 ± 0.023

Muonic X-ray structures of delayed spectra were summarized in Table 3-51. In this table, average of det-2, det-3, and det-4, results were described. Same as muon capture probability, the differences in muonic X-ray structure were not observed between two densities; 50 kPa and 99 kPa, in both experimental results of H_2+CO and H_2+CO_2. This mean, the muon transfer process and following muon cascading processes can be regarded as the same in these two density conditions, that is, muonic atom was isolated during de-excitation and electron refilling to muonic carbon and muonic oxygen negligible. The muonic X-ray structures for H_2+CO and H_2+CO_2 were also similar. This suggests that the molecular structure doesn't contribute to the initial quantum state of muons captured by carbon and oxygen atoms via the muon transfer process. There are previous reports of muonic X-ray structure for Lyman series of muonic oxygen in the high sample density condition for 15 bar of H_2+0.4%O_2 [49] and 10-15 bar of H_2+0.1-0.6%SO_2 [50], and these corresponded to the results of this work. In conclusion, chemical environmental effect in muon transfer process was considered as much smaller than that in muon direct capture process.

Table 3-51 Muonic X-ray structure (per K_α X-ray intensity ×100) of H_2+CO (99 kPa, 50 kPa), H_2+CO_2 (99 kPa, 50 kPa), H_2+O_2 [49] and H_2+SO_2 [50].

Transition	H_2+CO , 99 kPa	H_2+CO , 50 kPa	H_2+CO_2 , 99 kPa	H_2+CO_2 , 50 kPa	15 bar of H_2+0.4%O_2 [49]	10-15 bar of H_2+0.1-0.6% SO_2 [50]
μC(2-1)	100	100	100	100		
μC(3-1)	70 ± 6	85 ± 15	76 ± 9	92 ± 17		
μC(4-1)	48 ± 4	53 ± 9	53 ± 6	53 ± 10		
μC(3-2)	44 ± 5	68 ± 15	46 ± 8	63 ± 15		
μC(4-2)	21 ± 3	29 ± 8	24 ± 4	39 ± 9		
μO(2-1)	100	100	100	100	100	100
μO(3-1)	57 ± 4	56 ± 7	55 ± 4	63 ± 6	57 ± 1	55 ± 6
μO(4-1)	60 ± 5	60 ± 7	63 ± 4	75 ± 7	68 ± 1	66 ± 6
μO(5-1)	40 ± 4	38 ± 6	39 ± 3	47 ± 5	43 ± 1	42 ± 6
μO(3-2)	52 ± 5	67 ± 8	53 ± 5	49 ± 8		
μO(4-2)	34 ± 3	29 ± 5	36 ± 3	35 ± 5		
μO(5-2)	16 ± 2	17 ± 4	16 ± 2	20 ± 3		

Chapter4. Development of charge separation system for muonic atom

In this chapter, development process of muonic atom beam extraction system, and muon beam experiment using the system in J-PARC are described. General plot for the muonic atom beam extraction is described in 4-1. TOF-MS like system was designed to create muonic atom beam. Development of the experimental system for extraction muonic fluorin atom ion from PTFE film is described in 4-2. Pre-examination for optimization of the experimental system by laser ablation is described in section 4-3. Results from whole examination and determination method for mass to charge ratio (*m/z*) of ion species are also discussed. Muon beam experiments were performed twice in total (June and December in 2016). The improvement for the system is described in 4-4. Section 4-5 describes about the muon beam experiments at J-PARC.

4.1 General plot for the muonic atom beam extraction

In this study, to verify valence distribution of muonic atoms immediately after their formation, a method to extract muonic atoms as particle beams was focused. When a muonic atom is formed, captured muon de-excites with emitting Auger electrons, thus, multivalent positively charged ion are generated. Especially, the case of muon capturing in light elements, bare muonic atom ion without any electrons is formed [63]. Such ions whose bonds are broken are considered to be accelerated by Coulomb's repulsion (Coulomb explosion [60]), and partially escaped from the substance. Escaped ions are considered to be able to attracted and accelerated by electric field. In this thesis, experimental plot for detection muonic atom ions based on the principle of a double acceleration time of flight mass spectrometer [64] was established. PTFE film was chosen as muonic atom production target for the below reasons.

i. Handling of muonic fluorine atom beam is considered to be easy. Fluorine is one of light element (atomic number 9 in second period) and single isotope with only ^{19}F. Because fluorine is light nucleus, muonic fluorine atom has relatively long life, 1.5 μs.

ii. PTFE molecule consists of only carbon and fluorine, and side chains are all fluorine atoms. Therefore, it is considered that C - F bonds are preferentially destroyed by coulomb explosion, and muonic fluorine atom ions form easily after capturing muon.

iii. PTFE is easy to handle and has good availability.

4.1-1 principle of the muonic atom beam production and measurement

Schematic view of experimental system which generates and detects muonic atom beam is shown in Fig. 4-1. When muons are irradiated to the PTFE target, muonic fluorine atoms are formed and they take on highly positive charge. Some muonic atoms formed very close to the surface of target can escape from the target by coulomb explosion. Escaped muonic atoms are accelerated by electric fields and directed. This system is just like a time of fright mass spectrometer (TOF-MS).

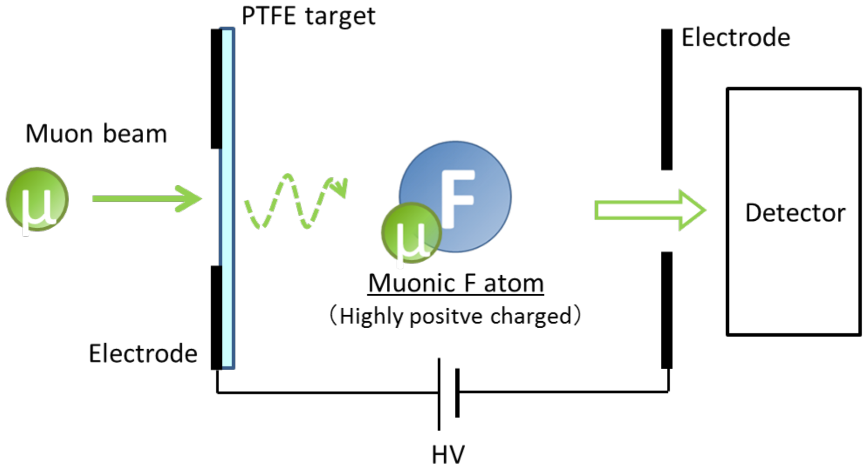

Fig. 4-1 Schematic view of muonic atom extraction and detection.

Some studies about fluorine atom ion extraction and detection by TOF-MS technique were already reported; bombardment with pulsed lasar [65], Synchrotron Radiation [66], and electron beam [67]. But any experiments by using muon beam irradiation have never been reported.

4.1-2 TOF detection system

Resolving power of ions: Δm is required less than 0.1, to distinguish muonic fluorine atom: μF^{n+} (19.1u) and normal fluorine atom: F^{n+} (19.0u). Δm is the width of the peak at a half of the maximum peak height (FWHM). Mass resolution is determined by formula 4-1, where R is mass resolution of TOF-MS and m is mass of the ion.

$$R = \frac{m}{\Delta m} = \frac{19.1\,u}{0.1\,u} = 191 \qquad (4\text{-}1)$$

Specifications of the TOF measurement system were determined as described in Table 4-1. Flight length of muonic fluorine atom was determined around 1 m considering the scalability and practicality. Considering the lifetime of muonic fluorine atom of 1.5 μs, time resolution of the detection system is desired 4 ns or less. Acceleration voltage of 5 kV is required to fly a μF^{8+} ion for 1 m during 1.5 μs.

Table 4-1 Rough estimation of the required specifications for muonic fluorine atom (μF^{8+}) extraction.

Flight time of ion	T	1.5	μs
Flight distance	D	0.955	m
Charge of ion	Z	8	e
Acceleration voltage	V	5000	V
Rest mass of ion	m	19.1	u

To design details of the TOF measurement system, specifications such as dimension, resolution and flight time were re-estimated based on the principle of Wiley and Mclaren's double acceleration type TOF-MS [64]. The specifications of the device when μF^{8+} and μC^{5+} are detected are shown in Table 4-2, and the flight time and mass resolution under the same conditions are shown in Table 4-3.

Here, explanation of Wiley-Mclaren type double acceleration TOF-MS is conducted. This is one of time of flight mass spectrometers, made focusing easier by two stages of electric field gradients using three acceleration electrodes. Two variables “d” and “E_d/E_s” are introduced newly, and these enable focusing finely compared to single electric field acceleration. As a result, the mass resolution was significantly improved (R~20 → R>100 in the 1950s). From upstream (ion source) side, the distance between the first electrode and second electrode is defined as “s”, the distance between second electrode and third electrode is defined as “d”, the distance between third electrode and the detector is defined as “D”. Electric field between first to second electrodes is defined as “E_s”, between second to third electrodes is defined as “E_d”.

However, the resolution strongly depends on deviation of initial ion position Δs and deviation of initial ion kinetic energy U_θ, so unless they can be reduced, the resolution cannot be improved, even if other parameters are changed anywhere. The overall resolution $R_{s,\theta}$ is described as the below equations (formula 4-2). R_s and R_θ correspond the resolutions of position and energy, respectively.

$$\frac{1}{R_{s,\theta}} = \frac{1}{R_s} + \frac{1}{R_\theta} \qquad (4\text{-}2)$$

Table 4-2 Specification of TOF system when assuming detection of μF^{8+} and μC^{5+} ion.

			μF^{8+}	F^{8+}	μC^{5+}	C^{5+}
Ion property	m	/ u	19.1	19.0	12.1	12.0
	q	/ e	8	8	5	5
Electrode	E_d	/ V·cm^{-1}	4640	4640	3710	3710
	E_s	/ V·cm^{-1}	360	360	290	290
	D	/ cm	95	95	95	95
	d	/ cm	1	1	1	1
	s_0	/ cm	1	1	1	1
	Δs	/ cm	0.2	0.2	0.2	0.2

Table 4-3 Mass resolution and flight length for μF^{8+} and μC^{5+} ions estimated by Wiley-Mclaren's principle [64].

			μF^{8+}	F^{8+}	μC^{5+}	C^{5+}
Flight time	$T(U_0,s_0)$	/ns	1639	1635	1845	1837
Space resolution	M_S	/ u	5556	5556	5517	5517
Energy resolution	M_θ	/ u	1191	1191	839	839
Over-All resolution	$M_{s,\theta}$	/ u	981	981	729	729
focusing distance	L	/ cm	97.64	97.64	96.60	96.60

In the case of detection for μF^{8+} ion by Wiley-Mclaren type TOF-MS, overall resolution is estimated as $R_{s,\theta}=981$, under the assumption for deviation of the initial position of muonic atom ions is $\Delta s=0.2$ mm, and the deviation of initial energy of muonic atom is $\Delta E=0.026$ eV (at RT). However, energies of μF^{8+} ions emitted from the surface of the target by Coulomb explosion are not uniform and difficult to control. It is necessary to suppress the deviation of μF^{8+} ions energy: ΔE set 1 eV or less, to accomplish the required resolution $R_{s,\theta}=191$ (the peak and the just neighbor peak overlapping with range of half width of the peak). It is estimated that the energy of μF^{8+} just after Coulomb explosion is 100 eV orders [60], and necessary to confirm it can be detectable experimentally.

4.2 Development of the experimental system

4.2-1 Outline of the system

TOF measurement systems for muonic atom beam observation were developed as shown in Fig. 4-2. The Wiley and Mclaren system with double acceleration electrode [64] was used as reference. The system consists of vacuum chambers, electrodes for muonic atom ion acceleration, target for muonic atom ion production (200 μm thickness film of poly tetra fluoro ethylene: PTFE), and micro channel plate (MCP) for muonic atom ion detection. Muonic atoms generated in the very close to surface of the target are escaped from the target as muonic fluorine and/or carbon atom ions by coulomb explosion, the ions are accelerated by the electric field, finally, reach the detector located at 1 m away.

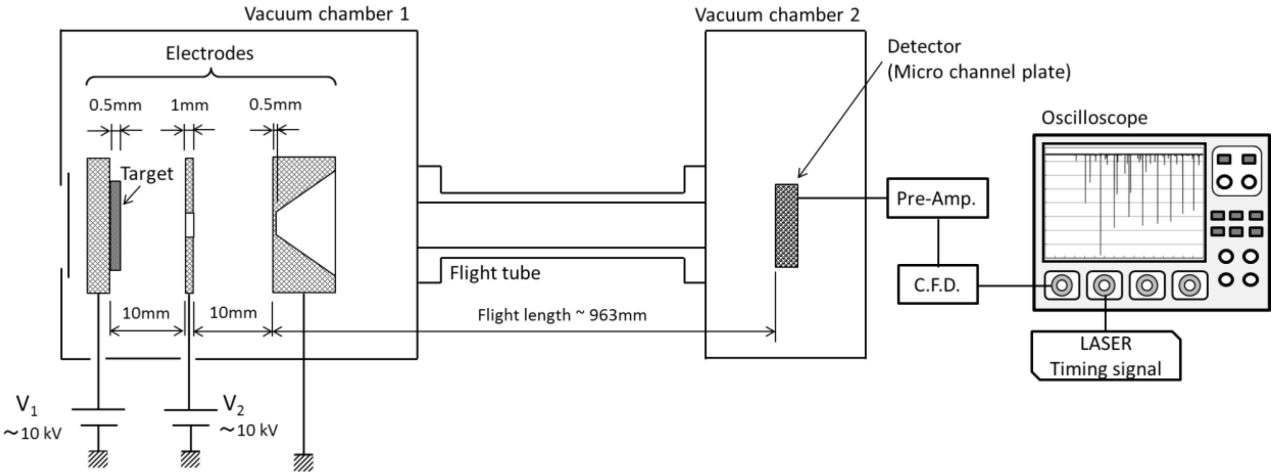

Fig. 4-2 Schematic view of muonic atom extraction system.

4.2-2 Components of experimental system

Main components of the experimental system were described in this section; vacuum chamber, target for muonic atom generation, electrode for muonic atom ion acceleration, and detector for determination of signals from muonic atom, are described. Also, Laser oscillator used in optimization for the system by laser ablation experiment, and surrounded devices are described.

· Vacuum chamber

Two size of vacuum chamber were manufactured. One is 20L of inner volume (chamber 1) and the other is 6 L of inner volume (chamber 2), both chambers are made from A5052: aluminum alloy. The side walls of chamber, various flange (JIS, NW) can be assembled. Overview of vacuum chamber is shown in Fig. 4-3. Drowing of chamber 1 is described in Fig. 4-4.

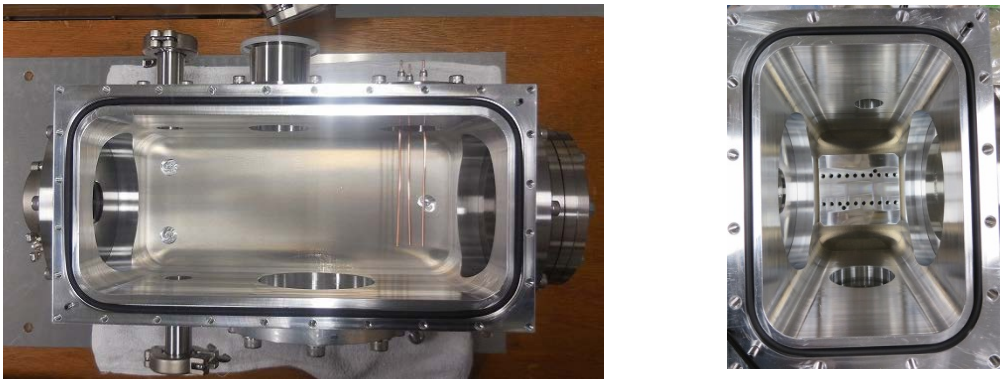

Fig. 4-3 Overview of vacuum chambers (left: chamber 1, right: chamber 2).

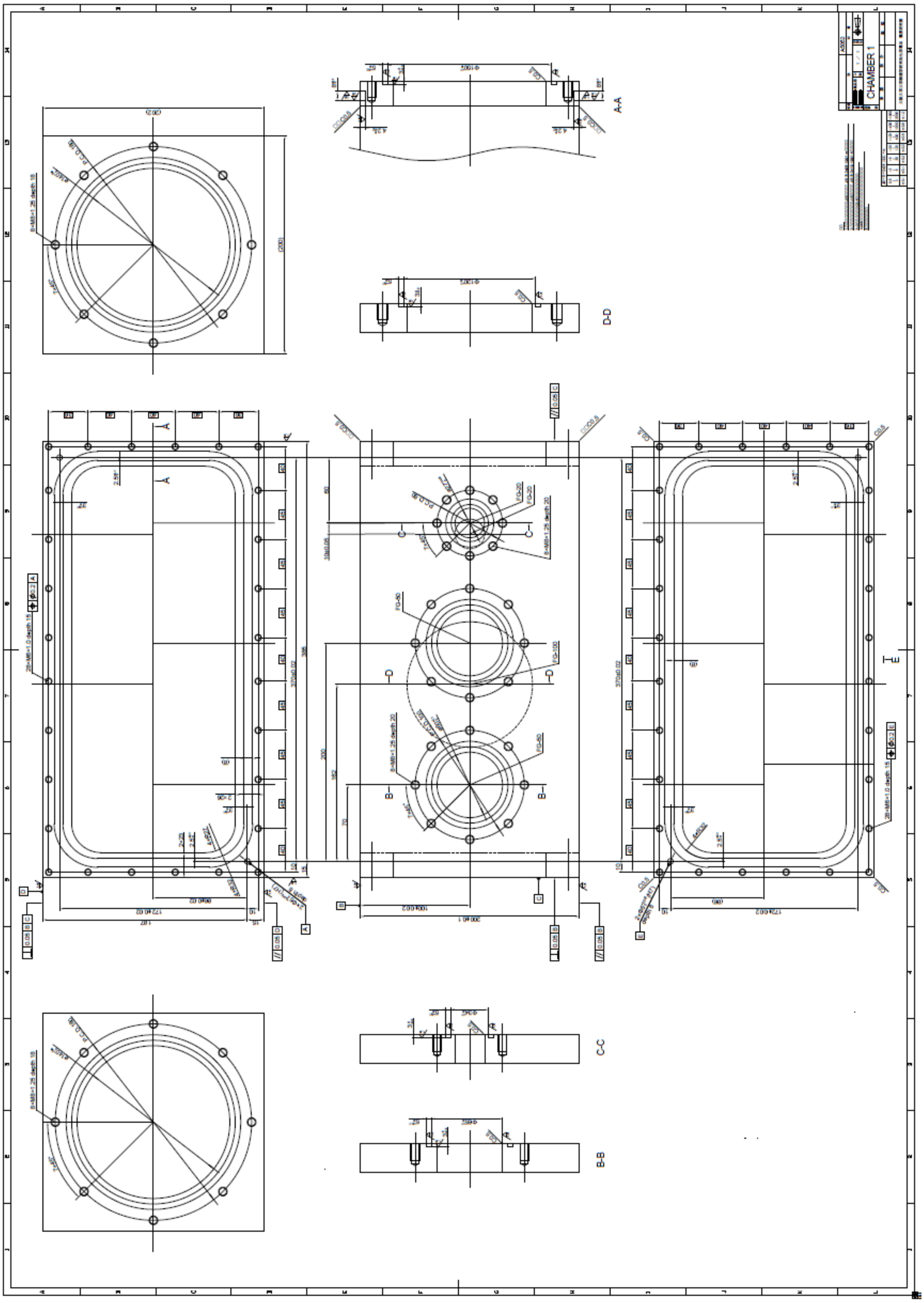

Fig. 4-4 The drawing of vacuum chamber1 (one portion of two sheets).

· Target

200 μm thickness of poly tetra fluoro ethylene: PTFE, film was used as muonic atom production target. It is considered that the muonic fluorine atom ions can be generated very close to surface of the target, lattice pattern (depth 20 μm, width 20 μm, pitch 20μm) were curved on the target surface by laser as shown in Fig.4-5, and surface area of target increased 4~5 times from original condition. In addition, PTFE filters were also used as a target in the muon beam experiment at J-PARC. Pure copper foil (t = 200μm), pure aluminum foil (t = 50μm), A5052 aluminum alloy plate (t = 200μm), and graphite plate (t = 200μm) were used as a target in optimization for the system by laser ablation.

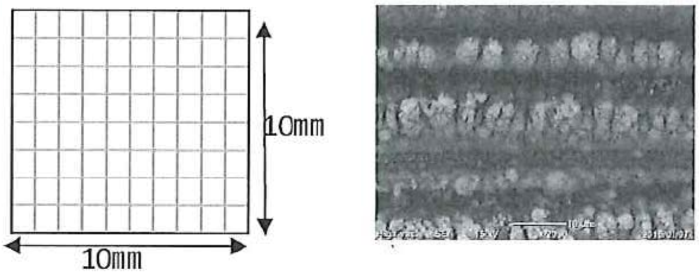

Fig. 4-5 Surface condition of the PTFE target (t=200μm). Lattice pattern (depth 20 μm, width 20 μm, pitch 20μm) were curved by laser, and surface area of target increased 4~5 times from original condition.

· Acceleration electrode

Acceleration electrode consists of three aluminum electrode plates (2.5 mm, 1.0mm, and 10.0 mm thicknesses from upstream side), as shown in Fig.4-6. There is a target holder on the first plate from the upstream side (direction of muon beam coming), and a PTFE target was installed here. In the 2nd and 3rd plates, 10 mm diameter holes for path of muonic atom beam are opened. The third plate was fixed to the vacuum chamber as ground (zero voltage). Both first and second plates were fixed to the third plate with insulators made from PTFE. Two high-voltage power supplies: HMBR-10P0.7 (10 kV positive electrode) manufactured by Matsusada Precision, Japan, were connected to the first and second plates.

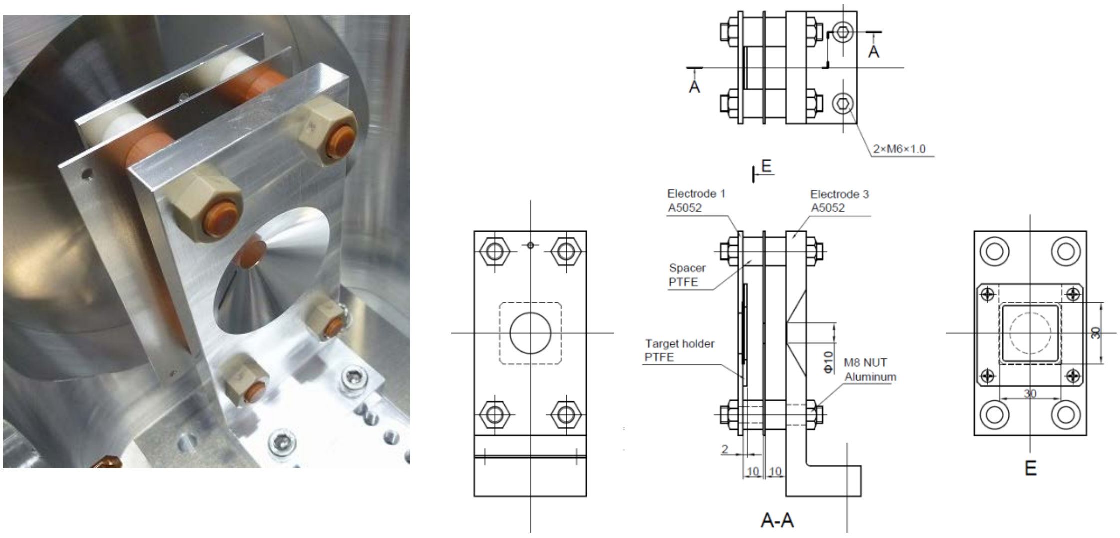

Fig. 4-6 Overview of electrode (left) and drawing of electrode (right).

· Detector

Micro channel plate (F12334-11, available diameter for detection is 20 mm, time resolution is 1.5 ns) manufactured by Hamamatsu Photonics, Japan, was used. Because, MCP body has to be floated electrically from the ground, a holder for MCP was made of poly-acetal (POM). Overview of MCP and MCP holder are shown in Fig. 4-7. Vacuum of 1.3×10^{-4} Pa or less is required for MCP operation.

Fig. 4-7 Overview of micro channel plate (MCP) and holder

· Vacuum pump

Two turbo molecular pumps were installed in the system. As a main vacuuming system, nEXT 300 (pumping speed 300 L/s) manufactured by Edwards, U.K. was used. In addition, as an auxiliary vacuuming system, X3580-64025 (pumping speed 180 L/s) manufactured by Agilent technologies, U.S. was used. This pump was supplied as vacuuming pump assembly: TPS-compact. The main vacuuming system was directly connected to the vacuum chamber 2, and the auxiliary vacuuming system was connected to the vacuum chamber 1 by using a flexible tube (NW50, 500 mm of length). These two pumps can vacuum the chambers from atomospher to 1.3×10^{-4} Pa within 1hour.

· Laser oscillator and surrounded optical equipments

The ND-YAG (neodymium-doped yttrium aluminum garnet; $Nd\text{-}Y_3A_{l5}O_{12}$) laser oscillator, FTSS-355-50-A; wave length: 355 nm, output: 150 μJ, pulse width: 1.0 ns, shown in Fig. 4-8 was used in optimization of the system (described in next section). This is manufactured by Crylas, Germany. In order to match the target surface to the laser focus, a convex lens (Edmond optics: # 48292, synthetic quartz plano-convex lens, focal point λ is 250 mm) and a mirror (Edmond optics: # 88527 refraction angle 0 - 45 °), shown in Fig. 4-8, was installed.

Fig. 4-8 Overview of LASER oscillator (left) and optical equipment (right).

· Data acquisition system (DAQ)

Oscilloscope: LT364 manufactured by Teledyne LeCroy, U.S., was used as a data acquisition tool for pre-examination. The signals from the detector (MCP) were amplified by the preamplifier: VT120C manufactured by ORTEC, U.S., and PM amplifier: 814-012 manufactured by KEK, Japan, then sent to constant fraction discriminator (CFD): 473A manufactured by ORTEC, U.S., and sent to the oscilloscope.

In the Optimization of the system, TAC and MCA system which was described in Fig. 4-9 was applied to conduct long run measurement. In the beam experiments, DAQ system in MLF J-PARC was used.

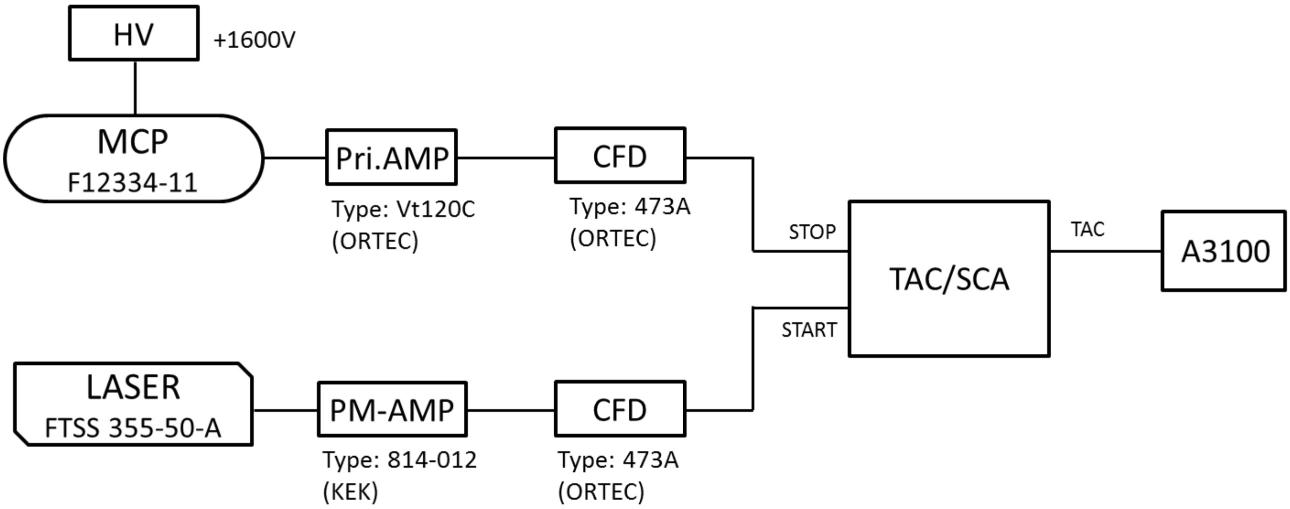

Fig. 4-9 Schematic view of data acquisition circuit for long run measurement.

4.2-3 Pre-estimation for background noises

Various background noises; such as secondary electrons (scattering and/or muon decay), photons, attributed to muon beam irradiation are suggested, at the experiment in J-PARC. So, Background noises were estimated by using particle transport simulation. Phits code (Ver. 2.76); general-purpose particle transport simulation code based on monte-carlo method developed by Japan atomic eneagy agency: JAEA [68] was used in the estimation. Muon beam were irradiated to PTFE target in vacuum chamber, then, a lot of high energy electrons and photons were generated. The number of noise components arrive at the detector were estimated quantitatively. Muon beam energy was determined as 2.4 MeV; borderline of muons stop in the 200 μm PTFE film. Iteration count of calculation was 100,000 (1000 muons × 100 times). Particle tracks calculated by phits code are shown in Fig. 4-10. The particle fulx of the electrons and photons passing through the detector was found to be almost zero, as shown in Fig 4-11. In this system, contaminations from secondary particles per 100,000 muons were estimated to be almost zero.

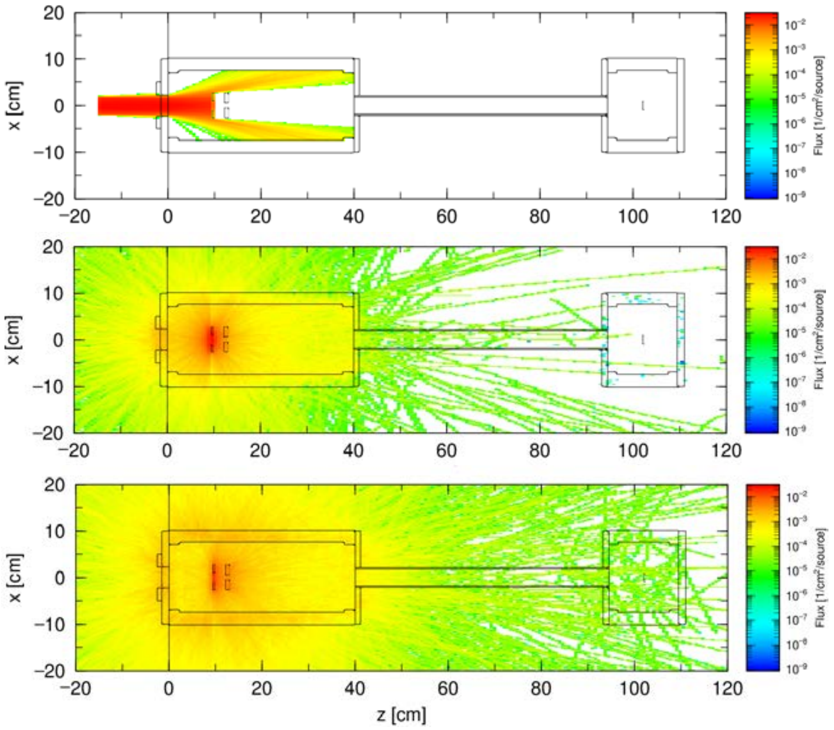

Fig. 4-10 Estimation of background noises attribute to muon irradiation. Particle tracks of secondary particles (scattered muon, electron, and photon) are calculated by phits code. Energy of irradiated muon is 2.4 MeV, number of repetition: n = 100,000. Top: muon, middle: electron (10keV< Ee<50MeV), bottom: photon (10keV< hν <100MeV).

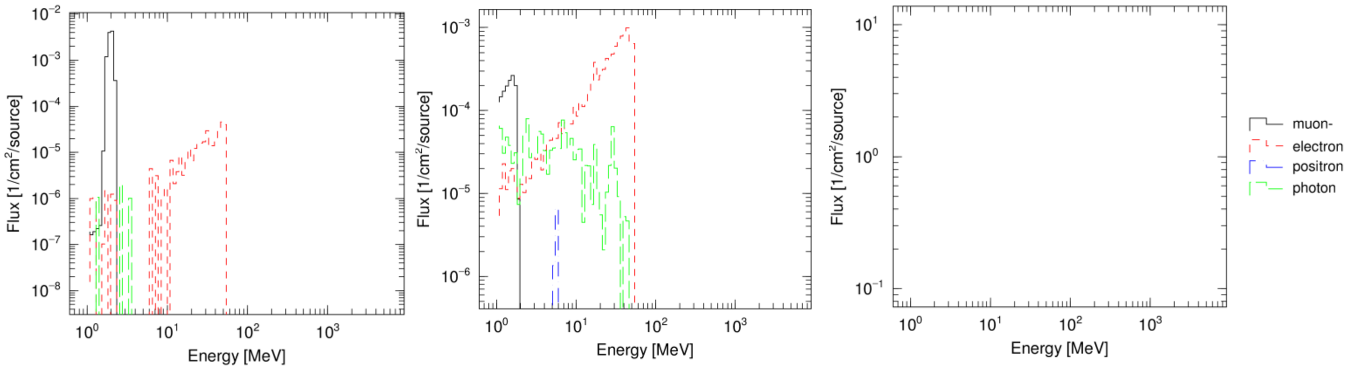

Fig. 4-11 Estimation of background noises attribute to muon irradiation. Particles penetrated poly-imide foil, target material, and detector are calculated by phits code. Calculation conditions are same as Fig.4-10. Left: muon, middle: electron, right: photon.

4.3 Optimization of the system

For pilot study, various ions acceleration and detection examinations using LASER ablation method were performed, and optimized ion beam yield and mass resolution of the sytem. In examination, Nd-YAG pulsed LASER (λ= 355 nm) described in previous section was used. One of the examination setup (overview of chamber 1) is shown in Fig. 4-12, as a representative. laser light comes from upside of the picture, it is focused and refracted then hits the surface of target and various ions are generated, ions are accelerated by electrode and finally measured by MCP detector.

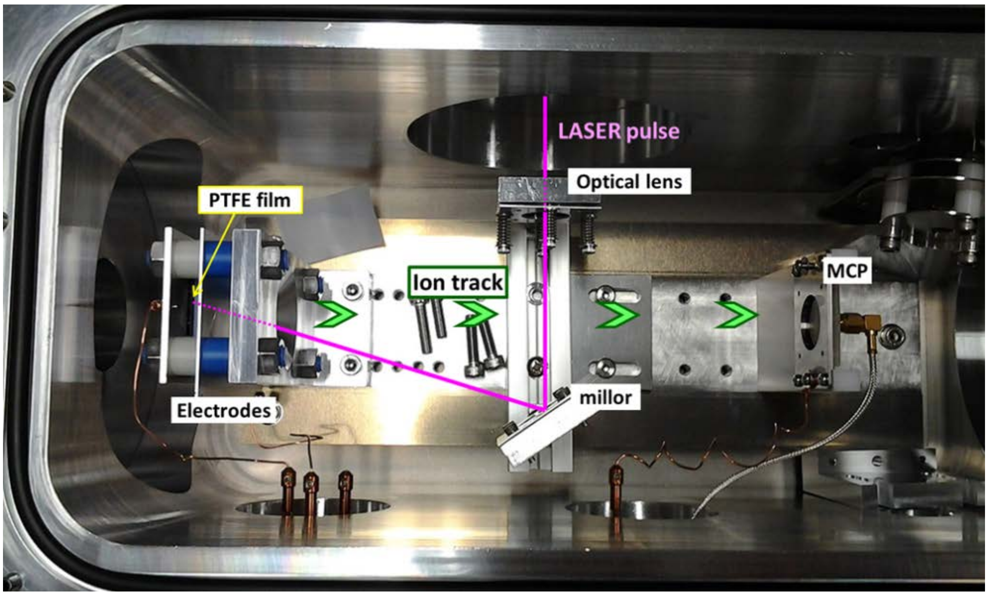

Fig. 4-12 Setup of the laser ablation experiment (overview of chamber 1), laser light comes from upside of the picture, it is focused and refracted then hits the surface of target and various ions are generated, ions are accelerated by electrode and finally measured by MCP detector.

4.3-1 Specifications for examination

To confirm whether the experimental system was properly designed, ion acceleration and detection experiments were performed in different flight length conditions (D = 223 mm, 612mm, and 963mm). Schematic overview of specification in D=223 is shown in Fig. 4-13, D=612 and 963 is shown in Fig.4-14. Overview of whole experimental system are shown in Fig. 4-15 (D=612), and Fig. 4-16 (D=963). In convenience, these three flight length conditions (D = 223 mm, 612mm, and 963mm) were defined as “Short”, “Middle”, and “Long” respectively.

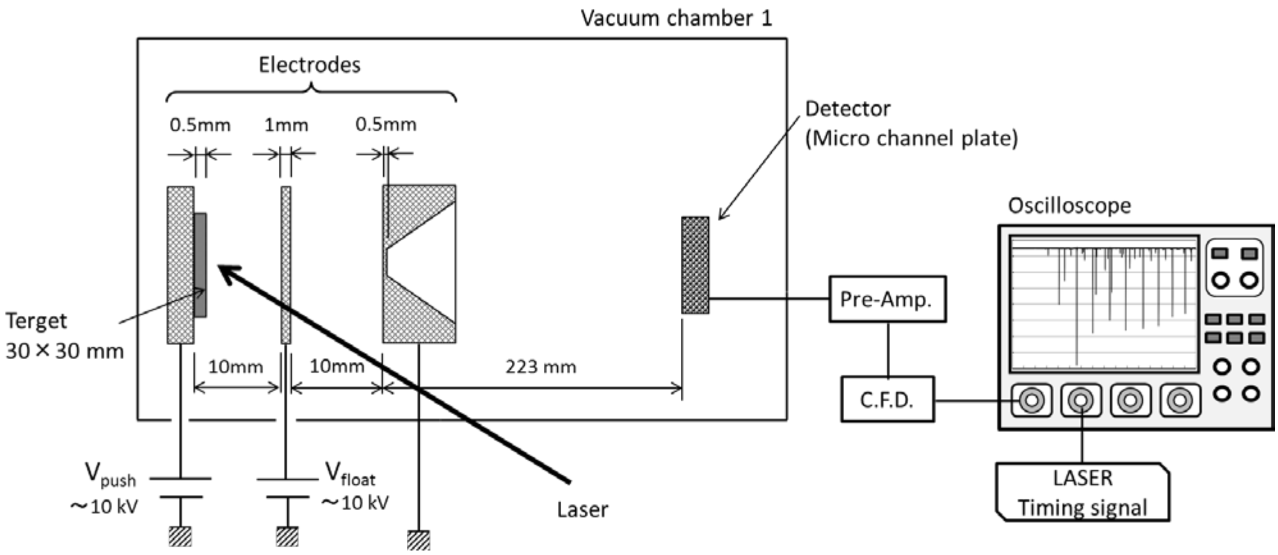

Fig. 4-13 Schematic view of laser ablation experiment for optimization of the system, this figure show the condition of ion flight length: D is 223mm (Short).

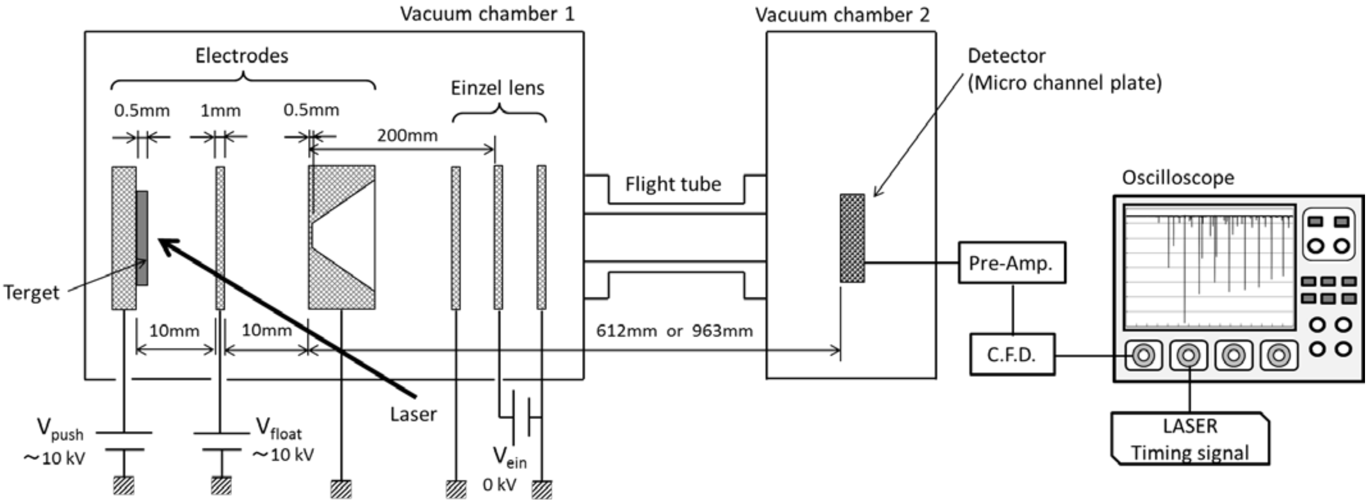

Fig. 4-14 Schematic view of laser ablation experiment for optimization of the system, this figure show the condition of ion flight length: D is 612mm (Middle) and 963 mm (Long).

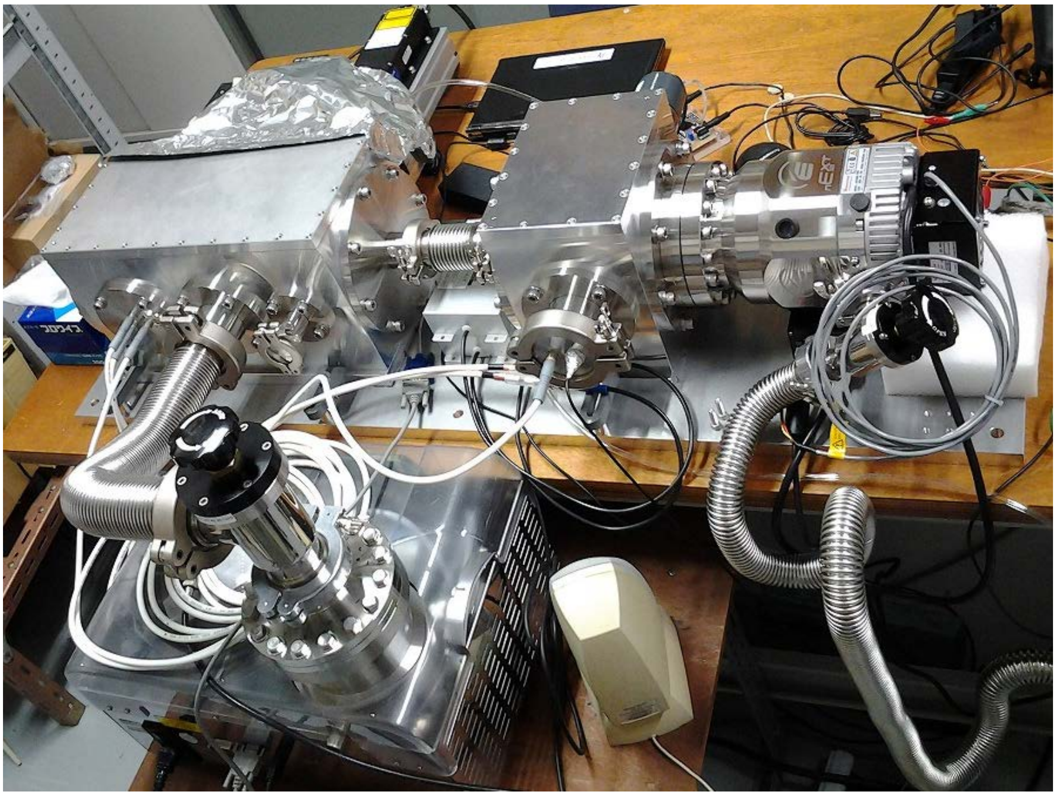

Fig. 4-15 Overview of laser ablation experiment; D is 612mm (Middle).

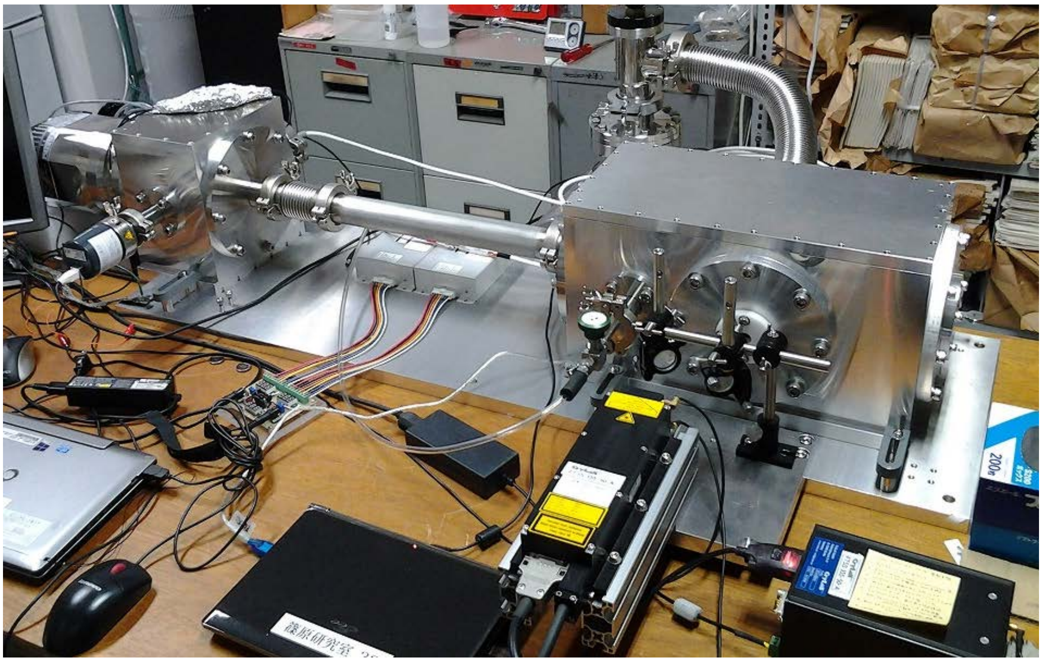

Fig. 4-16 Overview of laser ablation experiment; D is 963mm (Long).

In the examinations, PTFE was could not be used as a target, because PTFE does not have the absorption edge for 355 nm wavelength light. Instead of PTFE, 200μm thickness of graphite, 200μm of Aluminum alloy plate (Alloy-Al), 50μm of Pure Aluminum foil (Pure-Al), and 200μm of copper plate (Cu), were used as the target in the examination. Each target and used experimental conditions are summarized in Table 4-4.

Table 4-4 Target materials and applied conditions.

Target	Applied condition (flight length)		
Graphite (t 200 μm)	"Short"	"Middle"	"Long"
Aluminum alloy plate (t 200 μm)	"Middle"	"Long"	
Aluminum foil (t 50 μm)	"Long"		
Pure copper plate (t 200 μm)	"Middle"	"Long"	

Electrode voltages and laser output were varied as described in Table 4-5, for searching optimal condition. Laser output (SW) shows the output in 65536 (= 2^{16}) steps up to maximum output: 150 μJ, that is, SW5000 means 150×5000/65536 = 11.5 μJ. Iteration for the laser pulse was set to 25 Hz, and the measurement was repeated until 3000 times of statistics were collected (required 120 seconds) in all conditions.

Table 4-5 Range of electrode voltage and laser output.

	Range of value
Voltage of electrode 1 (V_{push})	1100 to 9000 V (mainly in 100 V increments)
Voltage of electrode 2 (V_{float})	1000 to 6000 V (mainly in 1000 V increments)
Laser output (SW)	5000 to 60000 max. (mainly in 10000 increments)

The Aim of each examination are follows, “Examination I” is performed to confirm relation between electrode voltage and TOF spectrum, “Examination II” is performed to confirm relation between ion flight length and TOF spectrum, “Examination III” is performed to confirm relation between target material and TOF spectrum. After three examinations were performed, determination method for mass to charge ratio (m/z) of ion species was established and ion species in TOF spectrum were identified. Finally, optimization for ion yield and mass resolution were performed using Micro channel analyzer (Examination IV). Specifications in each examination are summarized in Table 4-6.

Table 4-6 Specifications in each examination.

Contents of examination	Applied condition (flight length)	
Examination I	"Short"	"Middle"
Examination II	"Short"	"Middle"
Examination III	"Middle"	"Long"
m/z determination	"Middle"	"Long"
Identification of ion species	"Middle"	"Long"
Examination IV	"Long"	

4.3-2 Examination I: Relation between electrode voltage and TOF spectrum

Aim of this examination was to assure whether the ions can be detected properly by the system, and observed behavior of ions depending on the acceleration electrode voltage. Examinations were performed at the conditions of flight length "Short" (D=223 mm). 200 μm thickness of graphite plate was chosen as the target, and laser output was set to SW10000. The voltage of electrode 2: (V_{float}) was assigned to 8 conditions (1500 V, 2000 V, 2500 V, 2910 V, 3100 V, 3500 V, 4500 V, 5500 V), and TOF spectra were obtained while changing the voltage of electrode 1: (V_{push}) 100 V at a time, at each V_{float} condition. As a representative, the result of V_{float} = 5500 V is shown in Figure 4-17. The zero of horizontal axis was reflected the laser timing signal (zero point for time of flight). In the spectra, V_{push} and V_{float} are described as V_p and V_f respectively.

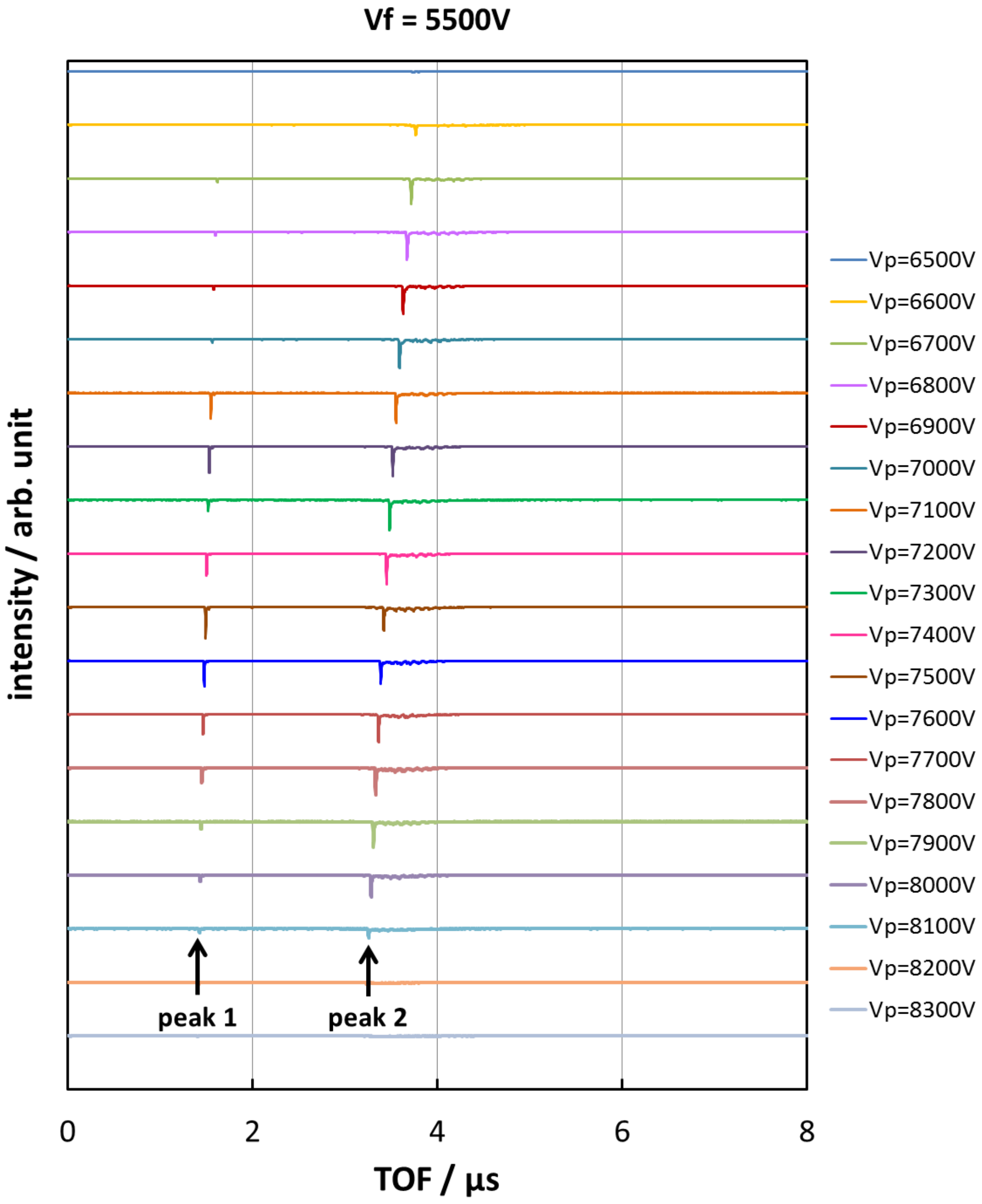

Fig. 4-17 TOF spectra; relation between acceleration voltage and spectrum, (Target: graphite, V_{float} is set 5500V, V_{push} is varied 6500V~8300V).

In all conditions, two significant peaks were detected. In convenience, left one (light component) was defined as peak 1, and right one (heavy component) was defined as peak 2. It is considered that same ions were detected in all conditions, because the shape of each spectrum was quite similar. Detection time for two peaks linearly changed depending on the acceleration voltage.

To confirm the relationship between acceleration voltage and TOF spectrum, peak height for the two peaks (peak 1 and peak 2) were plotted for each acceleration voltage, as shown in Fig. 4-18. Here, acceleration voltage was described as the ratio for V_{push} to V_{float} (V_p/V_f). It was found that the peak 1 and peak 2 were detected in the same region that V_p/V_f is 1.2 to 1.5, in all acceleration voltage conditions.

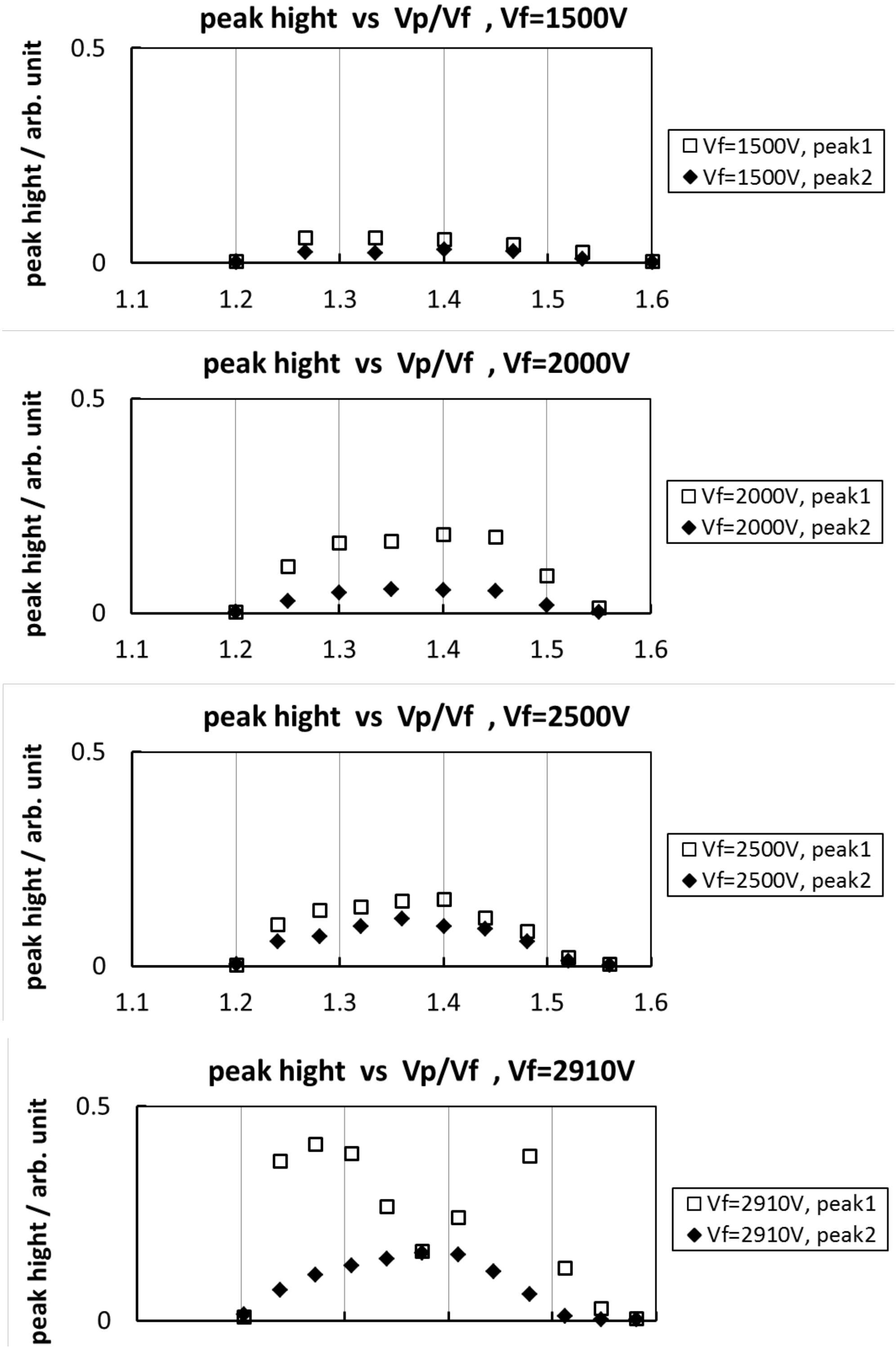

Fig. 4-18-(1) Relation between acceleration voltage ratio (Vp/Vf) and peak height, (V_{float} 1500V, 2000V, 2500V, 2910V) at D=223 mm condition.

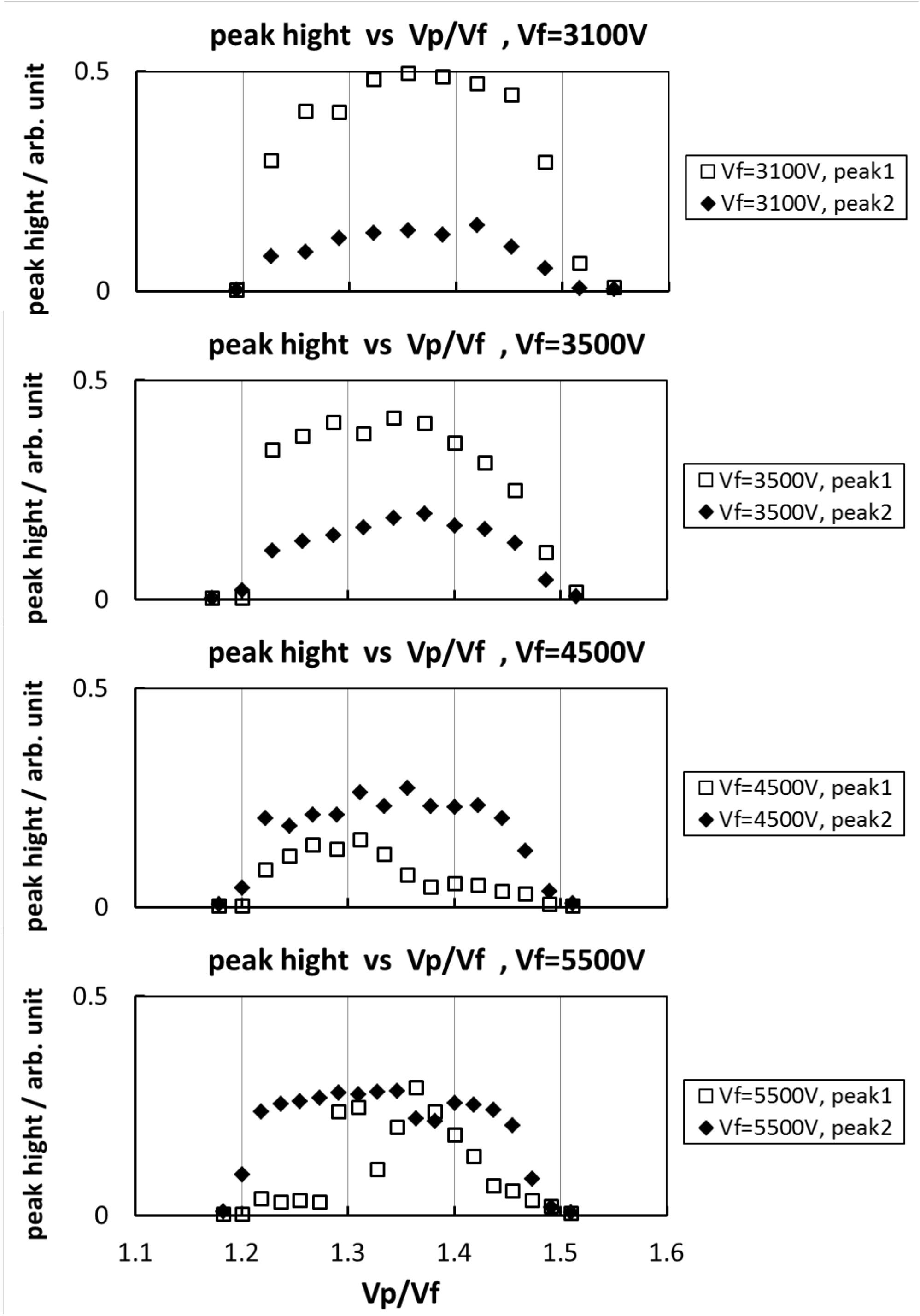

Fig. 4-18-(2) Relation between acceleration voltage ratio (Vp/Vf) and peak height, (V_{float} 3100V, 3500V, 4500V, 5500V) at D=223 mm condition.

4.3-3 Examination II: Relation between ion flight length and TOF spectrum

Aim of this examination was to assure whether the relationship between the acceleration voltage and TOF spectrum revealed in previous section was conserved even if the ion flight length is changed. Examinations were performed at the conditions of flight length "Middle" (D=612 mm). Same as previous examinations, 200 μm of graphite plate was used as the target, and laser output was set to SW10000. The V_{float} was assigned to 3 conditions (3000 V, 4500 V, 6000 V), and TOF spectra were obtained while changing the V_{push} so that V_p/V_f become in range of 1.2 to 1.5, at each V_{float} condition. As a representative, the result of V_{float} = 6000 V is shown in Figure 4-19.

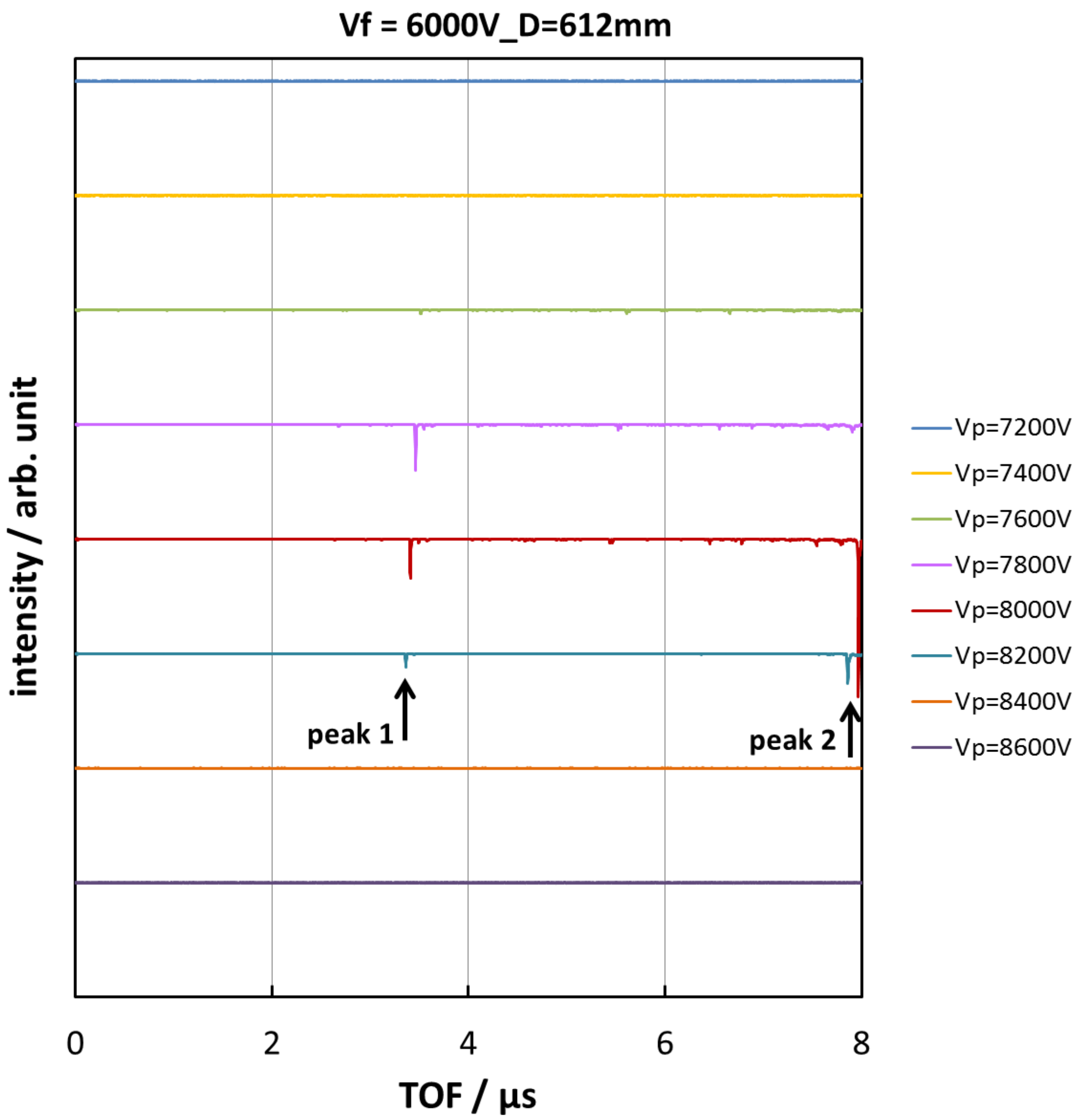

Fig. 4-19 TOF spectra; relation between acceleration voltage and spectrum, (Target: graphite, V_{float} is set 6000V, V_{push} is varied 7200V~8600V).

Same as previous examination, two peaks were confirmed, and detection time for two peaks linearly changed depending on the acceleration voltage. Also in this spectra, left one (light component) was defined as peak 1, and right one (heavy component) was defined as peak 2, and peak height for the two peaks were plotted for each acceleration voltage, as shown in Fig. 4-20. In all acceleration voltage conditions, peak 1 and peak 2 were detected in the same region that V_p/V_f is 1.2 to 1.5, this result corresponded to preivious examination.

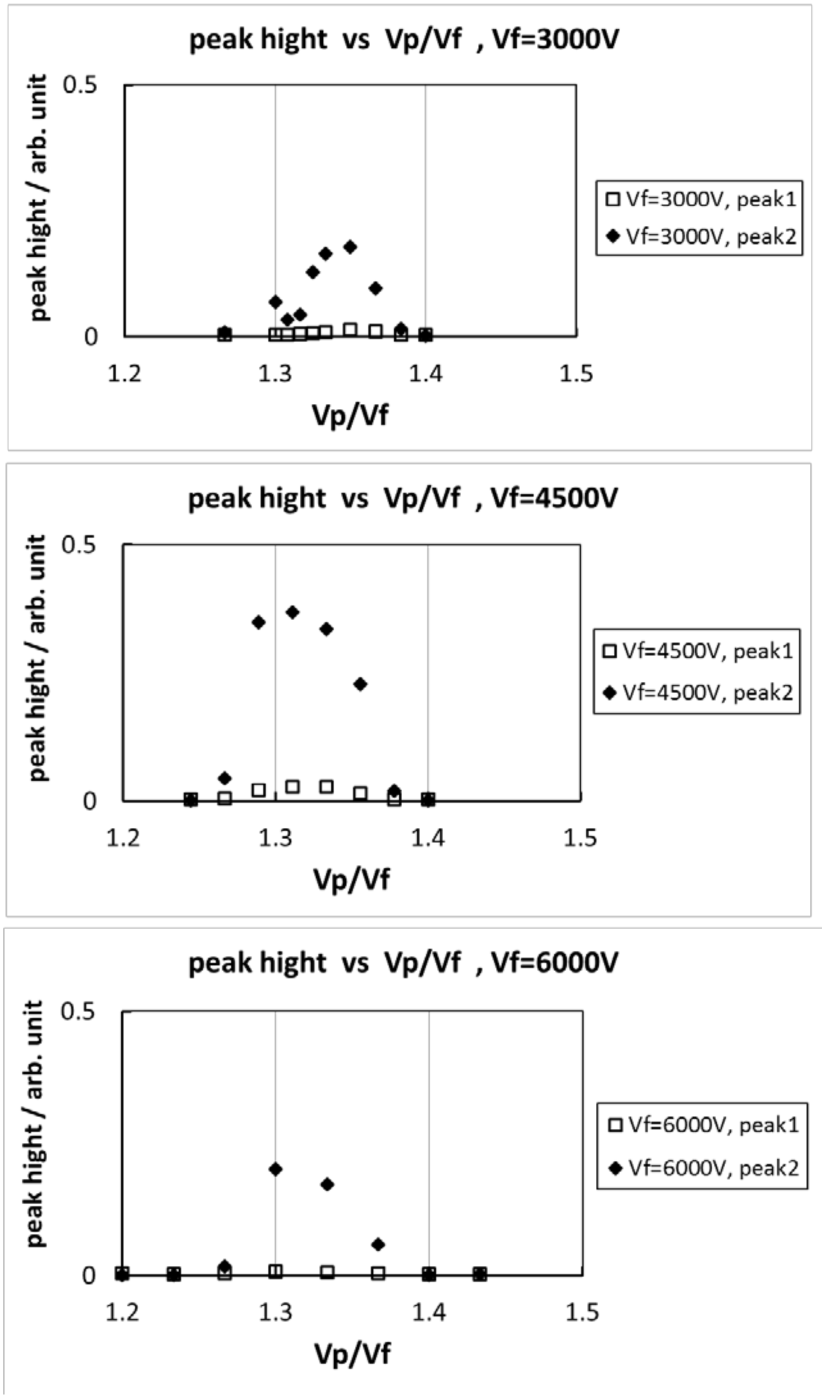

Fig. 4-20 Relation between acceleration voltage ratio (Vp/Vf) and peak height, (V_{float} 3000V, 4500V, 6000V) at D=612 mm condition.

In above experimental results, TOF spectrum depends on the ratio of acceleration voltage: V_p/V_f. This phenomenon is considered to be a feature of the double acceleration TOF-MS (Wiley-Mclaren type), based on the experimental system. In the Wiley-Mclaren type TOF-MS, accelerated ions are focused resonantly by two different electric field gradients. The focal length is determined by ratio of V_p/V_f and does not depend on individual values of V_p and V_f. This focusing effect is derived from shape of electric field, that is, the structure of electrode. The circular hole on electrode used in this experimental system has the function like optical lens in varying degree. Ions generated from the target pass through two kinds of combination lenses (holes on electrode 2 and 3), and bent into a trajectory depended on the refractive index. It is considered that the ratio of $V_p/V_f \sim 1.3$ became optimal refractive index in this experiment.

4.3-4 Examination III: Relation between target material and TOF spectrum

Aim of this examination was to observe what the spectrum changes when changing the target material. Examinations were performed at the conditions of flight length "Middle" (D=612 mm) and “Long” (D=963 mm). As a target material, copper plate (Cu), pure aluminum foil (pure-Al), aluminum alloy: A5052 plate (alloy-Al), and graphite plate were used. Laser output has been changed from SW10000 toSW40000 to increase the ion yield and species. The V_{float} and V_{push} were fixed 3000 V and 4000 V respectively ($V_p/V_f = 1.33$). TOF spectra are shown in Fig.4-21 to 4-25. Peaks which were marked “circle 1” to “circle 4”were used for determination of *m/z*. These peaks were high intensity and might be attributed to light sepecies same as fluorine. In each spectrum, peak marking (circle 1 to 4) didn’t correspond ion species.

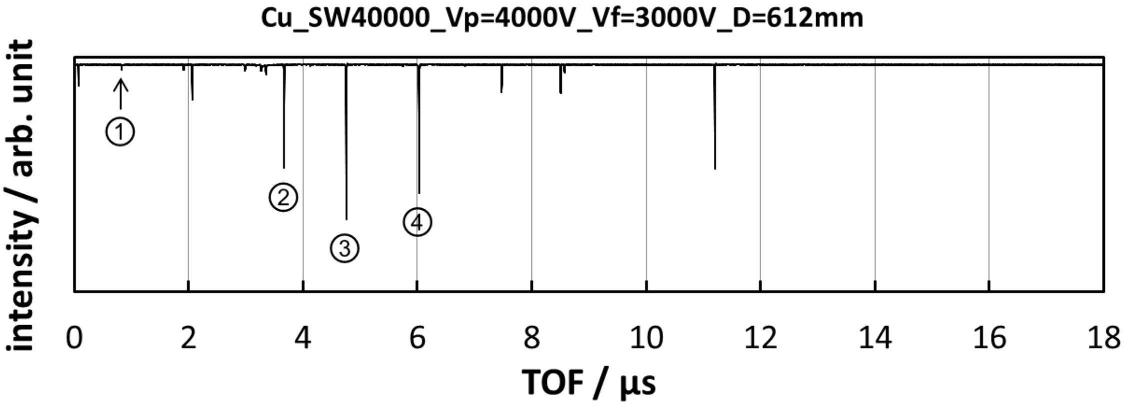

Fig. 4-21 TOF spectrum (Target: Cu, V_{float} =3000V, V_{push} = 4000V, D=612mm).

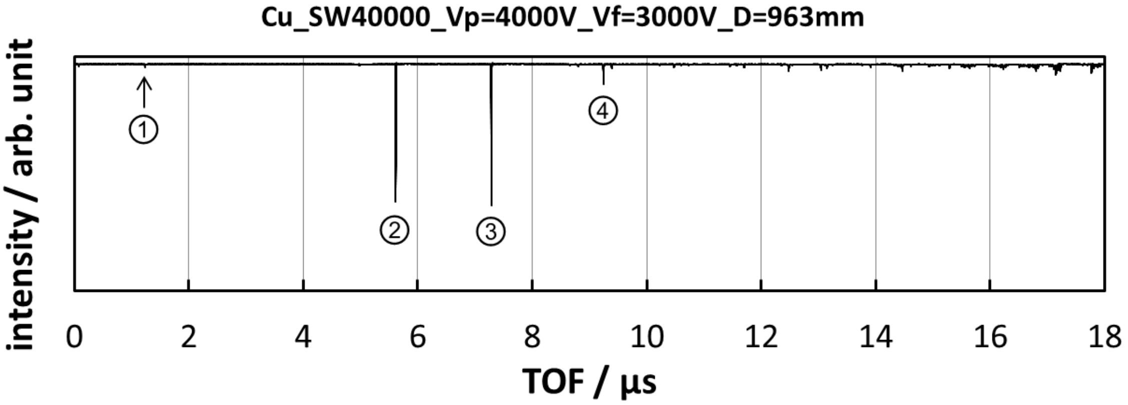

Fig. 4-22 TOF spectrum (Target: Cu, V_{float} = 3000V, V_{push} = 4000V, D=963mm).

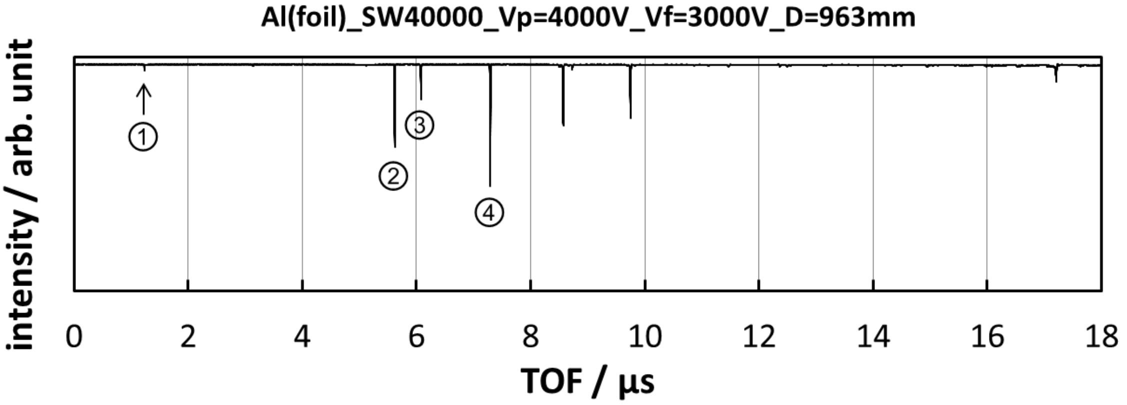

Fig. 4-23 TOF spectrum (Target: pure-Al, V_{float} = 3000V, V_{push} = 4000V, D=963mm).

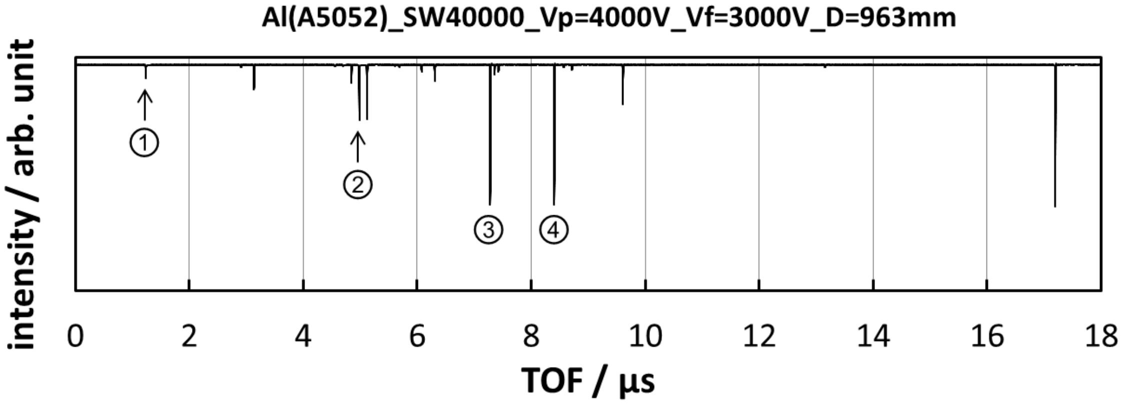

Fig. 4-24 TOF spectrum (Target: alloy-Al, V_{float} = 3000V, V_{push} = 4000V, D=963mm).

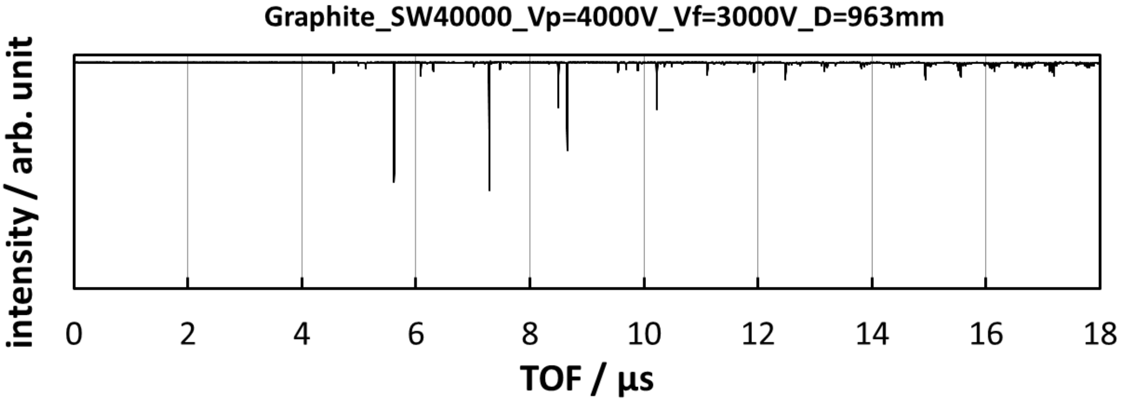

Fig. 4-25 TOF spectrum (Target: Graphite, V_{float} = 3000V, V_{push} = 4000V, D=963mm).

Since there were too many peaks, TOF spectrum of graphite target shown in Fig. 4-25, was excluded from the candidate for peak assignment described later. In this examination, peaks could be detected at long flight length (D=963 mm) condition, same as previous examinations. No peaks were detected when the acceleration voltages were shut down.

4.3-5 Determination method for mass to charge ratio (*m/z*) of ion species

The method for determination of mass to charge ratio (*m/z*) of ion species in the obtained TOF spectrum was established, and it is explained in this section. Parameters used in the determination process are listed below.

m : rest mass of ion [kg]

z : electrical charge of ion [C]

V_{push} : voltage of electrode 1 [V] (= 1.1×V_{float})

V_{float} : voltage of electrode 2 [V] (= 1000V~5000V)

d_1 : distance between electrode 1 and 2 [m] (= 0.01m)

b : thickness of electrode 2 [m] (= 0.001m)

d_2 : distance between electrode 2 and 3 [m] (= 0.01m)

L : distance between electrode 3 and detector [m] (= 0.173m)

First, the time requires to accelerate an ion from speed 0 to v_1 by the electric field between electrode 1 and 2 was determined. Here, voltage between electrode 1 to 2 was defined as V_1, that is, $V_1 = V_{push} - V_{float}$. The ion has a mass "*m*" and a charge "*z*" obtains acceleration "α_1" when passes through the electrode 1 and 2, and this relation can be described as below equation (formula 4-3).

$$\alpha_1 = \frac{z}{m}\frac{V_1}{d_1} \qquad (4\text{-}3)$$

Therefore, time required the ion passes thorough between the electrode 1 and 2 (t_1), and the arrival speed of the ion at the entrance of electrode 2 (v_1) can be described as below (formula 4-4 and 4-5).

$$t_1 = \sqrt{\frac{2d_1}{\alpha_1}} \qquad (4\text{-}4)$$

$$v_1 = \sqrt{\frac{2zV_1}{m}} \qquad (4\text{-}5)$$

The electrode 2 has finite thickness: 1 mm. If considered this section as equipotential, the ion is not accelerated (constant velocity), time required the ion passes thorough electrode 2 (t_1'), can be described as below (formula 4-6).

$$t_1{}' = \frac{b}{v_1} \qquad (4\text{-}6)$$

Next, the time requires to accelerate the ion from speed v_1 to v_2 by the electric field between electrode 2 and 3 was determined. Here, voltage between electrode 2 to 3 (ground) was defined as V_2, that is, $V_2 = V_{\mathrm{float}}$. The ion obtains acceleration "α_2" when passes through the electrode 2 and 3, and this relation can be described as below (formula 4-7).

$$\alpha_2 = \frac{z}{m}\frac{V_2}{d_2} \qquad (4\text{-}7)$$

Time required the ion passes thorough between the electrode 2 and 3 (t_2), and the arrival speed of the ion at the entrance of electrode 3 (v_2) can be described as below equation (formula 4-8 and 4-9). (From the relationship: $d_2 = v_1 t_2 + \frac{1}{2} a_2 t_2^2$)

$$t_2 = \frac{\sqrt{v_1^2 + 2\alpha_2 d_2} - v_1}{\alpha_2} \qquad (4\text{-}8)$$

$$v_2 = v_1 + \alpha_2 t_2 \qquad (4\text{-}9)$$

After the ion passes through electrode 3, ion is not accelerated and flies at constant velocity until it reaches the detector. Flight time of ion from electrode 3 to the detector (t_3) can be described as below (formula 4-10).

$$t_3 = \frac{L}{v_2} \qquad (4\text{-}10)$$

Therefore, the total time from the ion acceleration to the arrival at the detector (t) can be described as below equation (formula 4-11).

$$t = t_1 + {t_1}' + t_2 + t_3 \qquad (4\text{-}11)$$

Parameters "t_1" to" t_3" can be rewritten as below equations.

$$\begin{cases} t_1 = \sqrt{\dfrac{2d_1^2}{V_1}} \cdot \sqrt{\dfrac{m}{z}} & \text{(4-4')} \\ t_1{}' = \dfrac{b}{\sqrt{2V_1}} \cdot \sqrt{\dfrac{m}{z}} & \text{(4-6')} \\ t_2 = \dfrac{\left\{\sqrt{2V_1 + 2V_2} - \sqrt{2V_1}\right\} d_2}{V_2} \cdot \sqrt{\dfrac{m}{z}} & \text{(4-8')} \\ t_3 = \dfrac{D}{\sqrt{2V_1 + 2V_2}} \cdot \sqrt{\dfrac{m}{z}} & \text{(4-10')} \end{cases}$$

The total flight time "t" can be described as below equation (formula 4-11').

$$t = \left\{ \sqrt{\frac{2d_1^2}{V_1}} + \frac{b}{\sqrt{2V_1}} + \frac{\left\{\sqrt{2V_1 + 2V_2} - \sqrt{2V_1}\right\} d_2}{V_2} + \frac{D}{\sqrt{2V_1 + 2V_2}} \right\} \cdot \sqrt{\frac{m}{z}} \tag{4-11'}$$

Organizing this relationship into the form of "*m/z* ="

$$\frac{m}{z} = \left\{ \sqrt{\frac{2d_1^2}{V_1}} + \frac{b}{\sqrt{2V_1}} + \frac{\left\{\sqrt{2V_1 + 2V_2} - \sqrt{2V_1}\right\} d_2}{V_2} + \frac{D}{\sqrt{2V_1 + 2V_2}} \right\}^{-2} \cdot t^2 \tag{4-12}$$

That is, time of flight of ion (*t*) is properly obtained in an experiment, *m/z* can be determined as a quadratic function of "*t*" (formula 4-12).

Here, formula 4-12 was modified as formula 4-13, and fitting with experimental results of TOF spectra were performed. Peaks marked “circle 1” to “circle 4” in Fig.4-19 to 4-22 were used for determination of *m/z*.

$$\frac{m}{Z} = a(t+b)^c \qquad (4\text{-}13)$$

Where, “a” is a parameter relates to the acceleration voltage and geometry of system (components in the braces in formula 4-12), “b” is a delayed (or progressed) time from ideal time, and "c" is a correction factor for square calculation. If the initial kinetic energy of ion is small, *m/z* should correspond to quadratic function of t, theoretically, so “c” is fixed at 2. To determine the optimal solution for *m/z*, the equation described in formula (4-14) was established. Varying the parameters “a” and “b”, and the optimal solution that minimizes σ was determined. Where, “t_n” and “m_n” are TOF and rest mass for the ions attributed to “circle 1” to “circle 4” in Fig.4-20 to 4-23, respectively.

$$\sigma = \sqrt{\sum_{n=1}^{4} \left\{1 - \frac{a(t_n+b)^c}{m_n}\right\}^2} \qquad (4\text{-}14)$$

One of calculation results for determination minimum σ was shown in Fig.4-26. In this calculation, m/z value reproduces the four peaks (circle 1 to 4) in Fig. 4-22 (Cu, D = 963 mm “long”) was determined by varying “a” and “b”. As a result of calculation, 4 peaks were identified as follows, peak1 (TOF=1.231μs): ^{1}H (m/z=1.001), peak2 (TOF=5.615): ^{23}Na (m/z=23.01), peak3 (TOF=7.287): ^{39}K (m/z=39.00), and peak4 (TOF=9.245): ^{63}Cu (m/z=63.05).

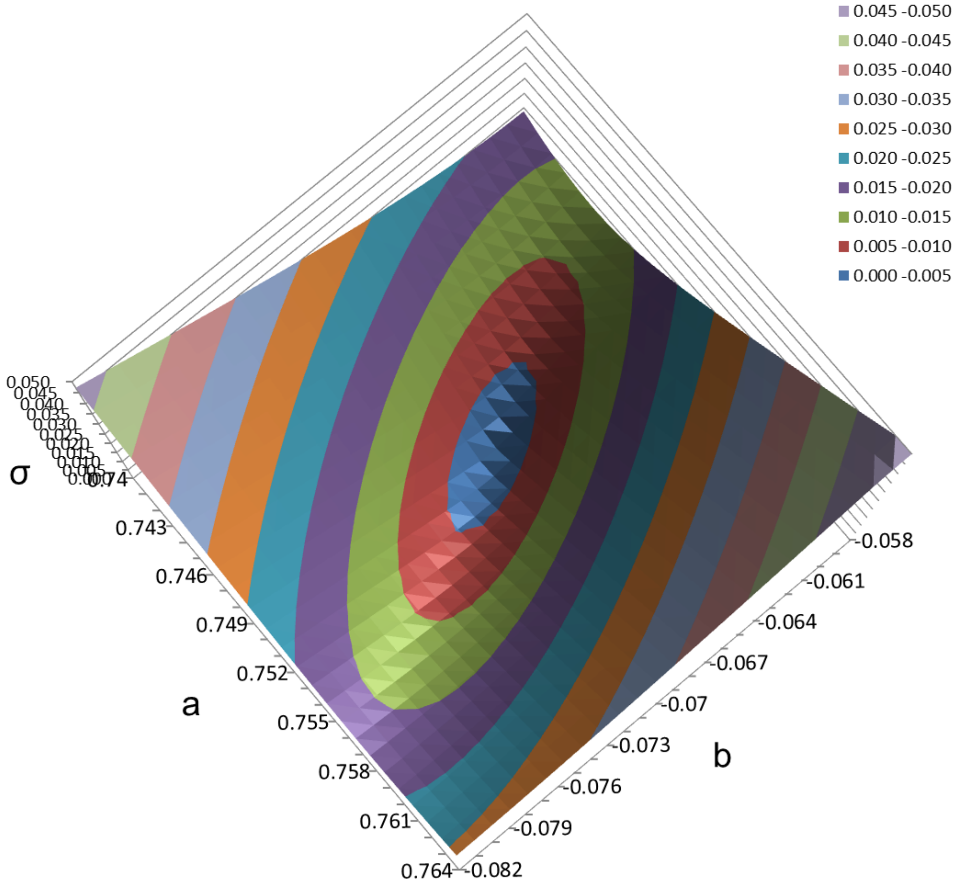

Fig. 4-26 Fitting result of parameter “a” and “b” (Cu, D=963mm “Long”).

The calculation results for the 4 conditions “Cu, D = 612 mm (middle)”, “Cu, D = 963 mm (long)”, “Pure-Al, D = 963 mm (long)”, and “Alloy-Al, D = 963 mm (long)” are summarized in Tables 4-7 to 4-10. From the left of the table, identified ion species for 4 peaks, atomic number of ion species (Z), measurement TOF values, and *m/z* values determined by the calculation are described. The theoretical value of “a” is estimated as 1.753 (at D = 612) and 0.750 (at D = 963), respectively.

Table 4-7 Result for determination of *m/z* and identification of ion species in Cu, D=612mm (middle) condition. Optimized value of parameter “a” and “b” are described bottom of the table.

Ion species		*m/z* (reference)[69]	t (TOF) /μs	*m/z* (fitting)*
1	$^{1}H^{+}$	1.008	0.827	0.999
2	$^{23}Na^{+}$	22.99	3.669	22.97
3	$^{39}K^{+}$	38.97	4.755	38.96
4	$^{63}Cu^{+}$	62.93	6.031	63.12

* optimized "a" is 1.781 ,"b" is -0.078

Table 4-8 Result for determination of *m/z* and identification of ion species in Cu, D=963mm (long) condition. Optimized value of parameter “a” and “b” are described bottom of the table.

Ion species		*m/z* (reference)[69]	t (TOF) /μs	*m/z* (fitting)*
1	$^{1}H^{+}$	1.008	1.231	**1.007**
2	$^{23}Na^{+}$	22.99	5.615	**22.99**
3	$^{39}K^{+}$	38.97	7.287	**38.95**
4	$^{63}Cu^{+}$	62.93	9.245	**62.95**

* optimized "a" is 0.748 ,"b" is -0.071

Table 4-9 Result for determination of *m/z* and identification of ion species in pure-Al, D=963mm (long) condition. Optimized value of parameter "a" and "b" are described bottom of the table.

Ion species		*m/z* (reference)[69]	t (TOF) /μs	*m/z* (fitting)*
1	$^{1}H^{+}$	1.008	1.231	**1.006**
2	$^{23}Na^{+}$	22.99	5.619	**23.01**
3	$^{27}Al^{+}$	26.98	6.079	**26.98**
4	$^{39}K^{+}$	38.97	7.293	**38.99**

* optimized "a" is 0.748 ,"b" is -0.071

Table 4-10 Result for determination of *m/z* and identification of ion species in alloy-Al, D=963mm (long) condition. Optimized value of parameter "a" and "b" are described bottom of the table.

Ion species		*m/z* (reference)[69]	t (TOF) /μs	*m/z* (fitting)*
1	$^{1}H^{+}$	1.008	1.233	**1.008**
2	$^{1}H_2{}^{16}O^{+}$	18.01	4.983	**18.06**
3	$^{39}K^{+}$	38.97	7.281	**38.91**
4	$^{1}H_4{}^{16}O_3{}^{+}$	52.02	8.403	**51.97**

* optimized "a" is 0.749 ,"b" is -0.073

As a result of calculation, *m/z* and ion species of 4 peaks could be determined in all condition. Estimated *m/z* values were corresponded to Z within Δm/m<0.001, with a few exceptions. In the condition of Cu, D=612, slight difference between *m/z* and Z were observed in 4 peaks, but in the condition of Cu, D=963, *m/z* corresponded to Z very well. Also, in this condition, estimated "a (= 0.748)" completely corresponded to theoretical "a". It is considered that the ion flight distance was extended (the contribution of D in formula 4-11' increased) and the mass resolution was improved.

4.3-6 Peak assignment in TOF spectrum; identification of ion species

All observed peaks were identified, by the method for determination of m/z described in previous section, in the following 5 conditions “Cu, D = 612 mm (middle)”, “Cu, D = 963 mm (long)”, “Pure-Al, D = 963 mm (long)”, “Alloy-Al, D = 963 mm (long)”, and “Graphite, D = 963 mm (long)”. The results are shown in Table 4-11 ~ 4-15.

Table 4-11 Peak assignment for “Cu, D = 612 mm (middle)”.

t (TOF) /μs	*m/z*	candidate
0.827	1.00	H^+
1.915	6.01	$^{6}Li^+$
2.063	7.02	$^{7}Li^+$
2.987	15.07	NH^+
3.267	18.11	H_2O^+
3.353	19.10	H_3O^+
3.669	22.97	$^{23}Na^+$
4.755	38.96	$^{39}K^+$
6.031	63.12	$^{63}Cu^+$
7.473	97.40	$(Cu+H_2O_2)^+$
8.505	126.48	$^{63}Cu_2{}^+$
8.571	128.47	$^{63}Cu^{65}Cu^+$

Table 4-12 Peak assignment for “Cu, D = 963 mm (long)”.

t (TOF) /μs	*m/z*	candidate
1.231	1.00	H^+
5.615	23.01	$^{23}Na^+$
7.287	39.00	$^{39}K^+$
9.245	63.05	$^{63}Cu^+$
9.389	65.05	$^{65}Cu^+$
10.475	81.10	$(Cu+H_2O)^+$

Table 4-13 Peak assignment for “Pure-Al, D = 963 mm (long)”.

t (TOF) /μs	*m/z*	candidate
1.231	1.00	H^+
5.619	23.01	$^{23}Na^+$
6.079	26.99	$^{27}Al^+$
7.293	39.01	$^{39}K^+$
8.571	54.05	Al_2^+ , $(H_2O)_3^+$
8.727	56.06	$Al_2H_2^+$
9.749	70.08	Al_2O^+

Table 4-14 Peak assignment for “Alloy-Al, D = 963 mm (long)”.

t (TOF) /μs	*m/z*	candidate
1.233	1.00	H^+
3.137	7.02	$^{7}Li^+$
4.845	17.04	OH^+
4.983	18.04	H_2O^+
5.119	19.06	H_3O^+
6.077	26.99	Al^+
6.309	29.12	AlH_2^+
7.281	38.91	K^+
7.355	39.72	$^{24}MgO^+$
7.359	39.76	$^{25}MgO^+$
7.425	40.48	$^{26}MgO^+$
8.403	51.98	$H_4O_3^+$
8.715	55.95	$Al_2H_2^+$
9.607	68.10	$MgAlO^+$

Table 4-15 Peak assignment for “Graphite, D = 963 mm (long)”.

t (TOF) /μs	*m/z*	candidate
5.617	23.01	Na^+
7.285	38.96	K^+
8.497	53.16	$C_4H_5^+$
8.653	55.15	$C_4H_7^+$
10.225	77.22	$C_6H_5^+$

Focusing on results of Cu (both middle and long) and Pure-Al, the calculation could identify all peaks as reasonable ion species. On the other hand, but the results of Alloy-Al and Graphite, there were many peaks difficult to identify. Alloy-Al (A5052) contains various isotopes such as ^{24}Mg, ^{25}Mg, ^{26}Mg and ^{28}Si, and its surface are covered by oxide, so, it is difficult to obtain accurate TOF of emitted ions. Likewise, since graphite generates many kinds of fragment ions by laser ionization, it is considered difficult to obtain an accurate TOF with a small amount of statistics.

In the results of Cu (long) and Pure-Al, for elements have stable isotopes such as potassium (^{39}K and ^{41}K) and copper (^{63}Cu and ^{65}Cu), experimental peak yield were compared with natural abundance. Mass resolutions were also estimated from FWHM of each peak. Figures 4-27 and 4-28 show magnified view of around the peaks of potassium and copper isotopes. The spectrum shows square root of squared raw-signals.

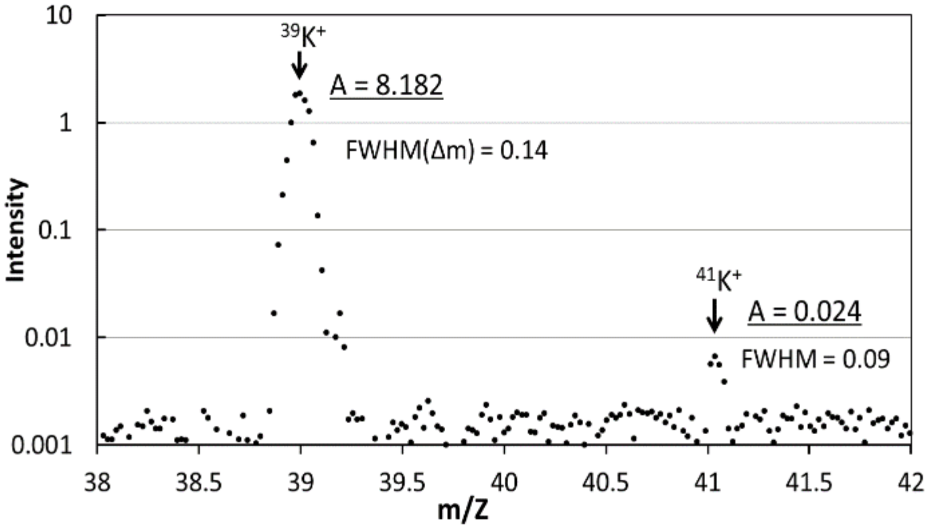

Fig. 4-27 peaks of ^{39}K$^+$ and ^{41}K$^+$ in TOF spectrum (Cu, D=963mm).

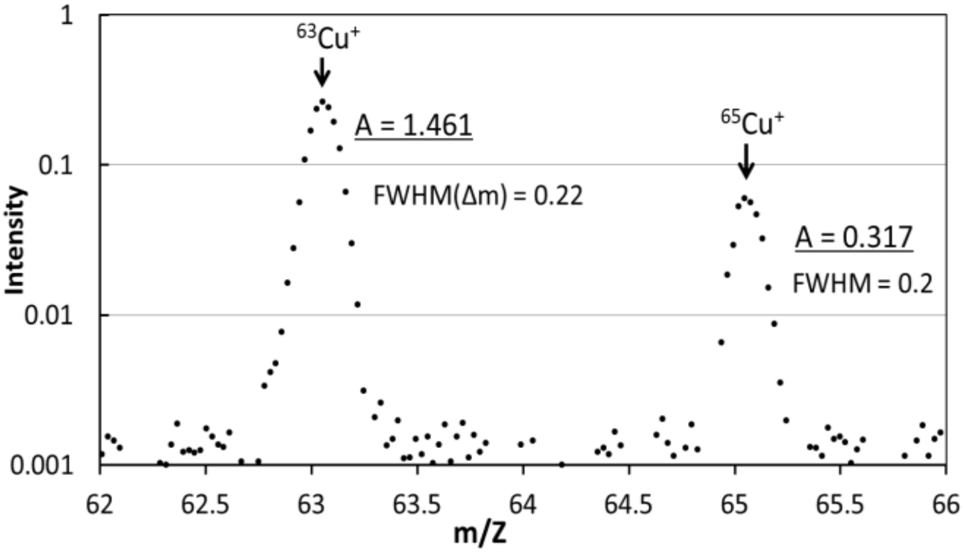

Fig. 4-28 peaks of ^{63}Cu$^+$ and ^{65}Cu$^+$ in TOF spectrum (Cu, D=963mm).

For elements have stable isotopes such as potassium (^{39}K and ^{41}K) and copper, (^{63}Cu and ^{65}Cu) experimental peak yield were compared with natural abundance. The natural abundances of ^{39}K and ^{41}K are 93.258% and 6.730% [69], respectively, but the experimental yields were ^{39}K: 99.7% and ^{41}K: 0.3%. Similarly, the natural abundances of ^{63}Cu and ^{65}Cu are 69.17% and 30.83% [69] respectively, but the experimental yields were ^{63}Cu: 82.2% and ^{65}Cu: 17.8%. In both cases, difference from natural abundance were confirmed, especially, potassium yields is significantly out from the natural abundance. Possible reason, ions were coming at the rate exceeds resolving time of the detector, thus the detector could not count the heavier isotopes. Laser output was decreased from 40000 to 25000 and 20000, and compared the yield of two peaks in the same way. The results are shown in Fig.4-29. When the laser power decreased, copper peaks became disappeared (too small to obtain the yield), copper yield was excluded from the discussion.

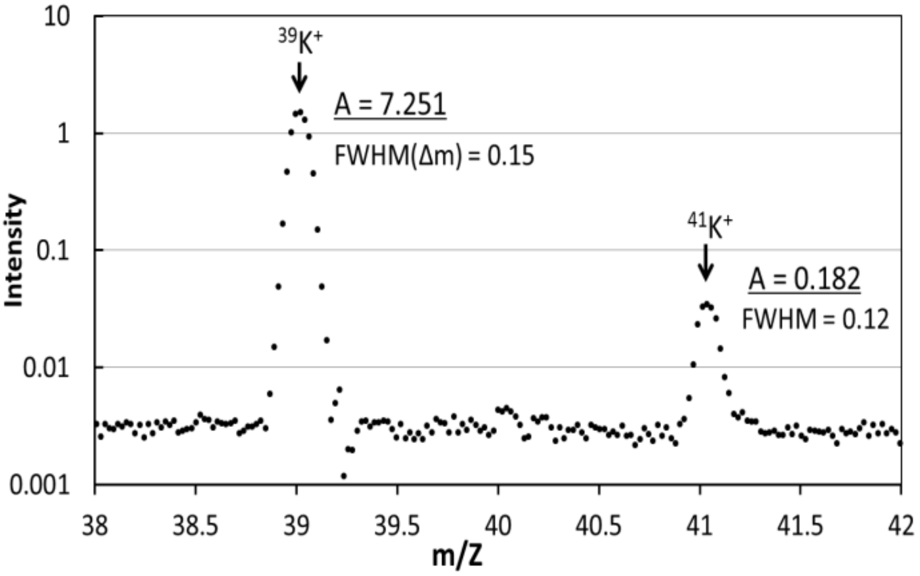

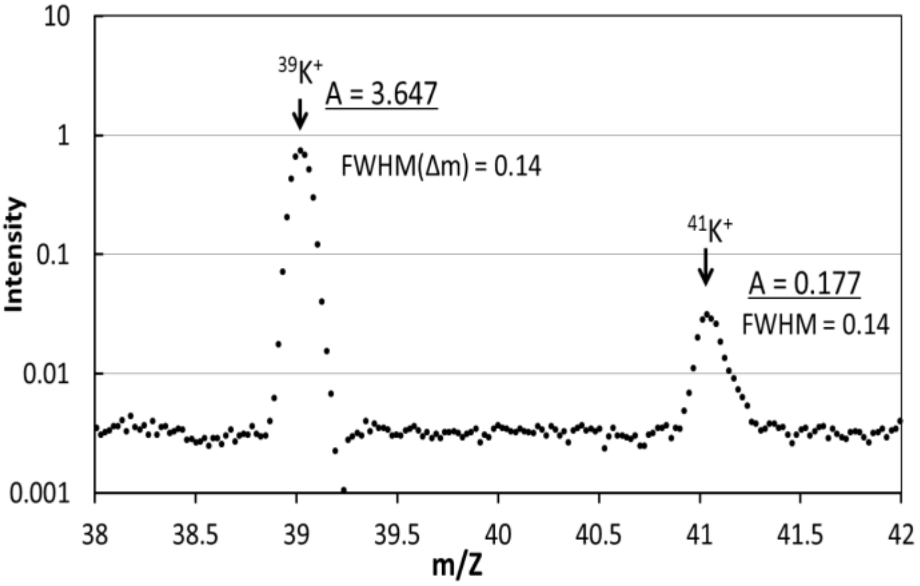

Fig. 4-29 peaks of $^{39}K^+$ and $^{41}K^+$ in TOF spectrum (Cu, D=963mm), top spectrum shows the result at laser power of SW25000, bottom spectrum shows the result at laser power of SW20000.

When the laser output decreased to 25000 and 20000, the peak of ^{39}K became smaller but the peak of ^{41}K became larger. Under the condition of laser power at SW20000, experimental yield rate of ^{39}K and ^{41}K were 95.14 % and 4.86 %, respectively. Although there was a slight difference from natural abundance, the results supporting the assumption attributed to high count rate were obtained.

In the case of potassium and copper, since lighter isotopes account for large part, heavier isotopes were hardly counted when the beam intensity was large. On the other hand, case of the element which heavier isotopes account for large part such as lithium, the beam intensity is considered to be less likely to affect counting loss for the isotopes. Therefore, the yield rates for ^{6}Li and ^{7}Li were obtained from the spectra of “Cu, D = 612 mm, (middle)" where both ^{6}Li and ^{7}Li were observed. Magnified view of around ^{6}Li and ^{7}Li peaks is shown in Fig.4-30.

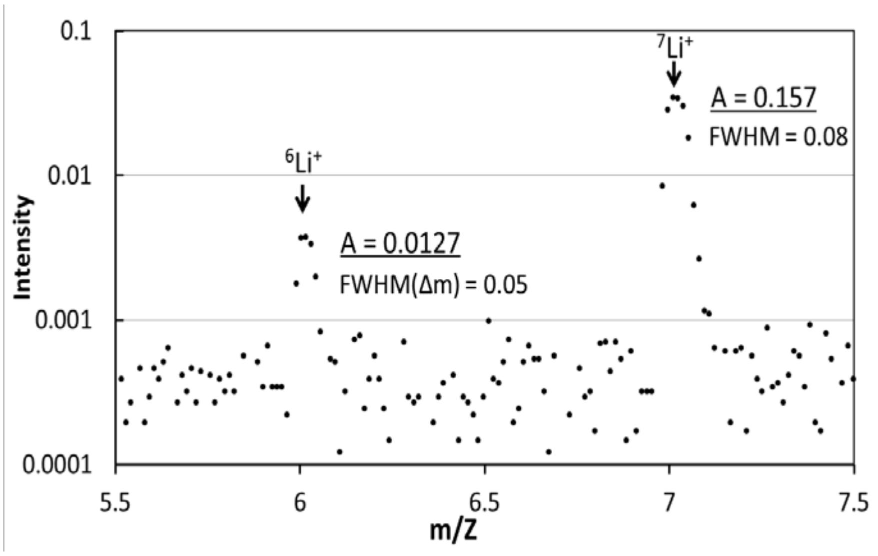

Fig. 4-30 peaks of ^{6}Li^{+} and ^{7}Li^{+} in TOF spectrum (Cu, D=612mm, SW40000).

The yield rates of ^{6}Li and ^{7}Li were 7.48% and 92.52%, respectively, and these values well corresponded to the natural abundance ^{6}Li: 7.5% and ^{7}Li: 92.5% [69]. As expected, when a laser output is large, too much ions are generated, ions were coming at the rate exceeds resolving time of the detector, thus the detector could not count the heavier isotopes.

In this examination, mass resolution: R, were determined in some conditions, and these were approximately R = 300, was above required resolution of R = 191. Optimization for mass resolution is described in next section.

4.3-7 Examination IV: Optimization for ion yield and mass resolution

In order to investigate the relationship between the acceleration voltage and ion yield and mass resolution in more detail, long run measurement were performed. In performing experiments, data acquisition system was changed from oscilloscope (shown in Fig 4-13 and 4-14) to TAC and MCA system (shown in Fig.4-10).

Examinations were performed at the conditions of flight length "Long" (D=963 mm). 200 μm thickness of copper plate was chosen as the target, and laser output was set to SW40000. The V_{float} was assigned to 4 conditions (3000 V, 4000 V, 5000 V, 6000 V), and TOF spectra were obtained while changing the V_{push} so that V_p/V_f become in range of 1.2 to 1.5, at each V_{float} condition. Each spectrum was measured in 30 minutes to 2 hours. In this examination, focused on $^1H^+$ and observed what the yield and the resolution change when changing the accelerating voltages, results are summarized in Fig.4-31.

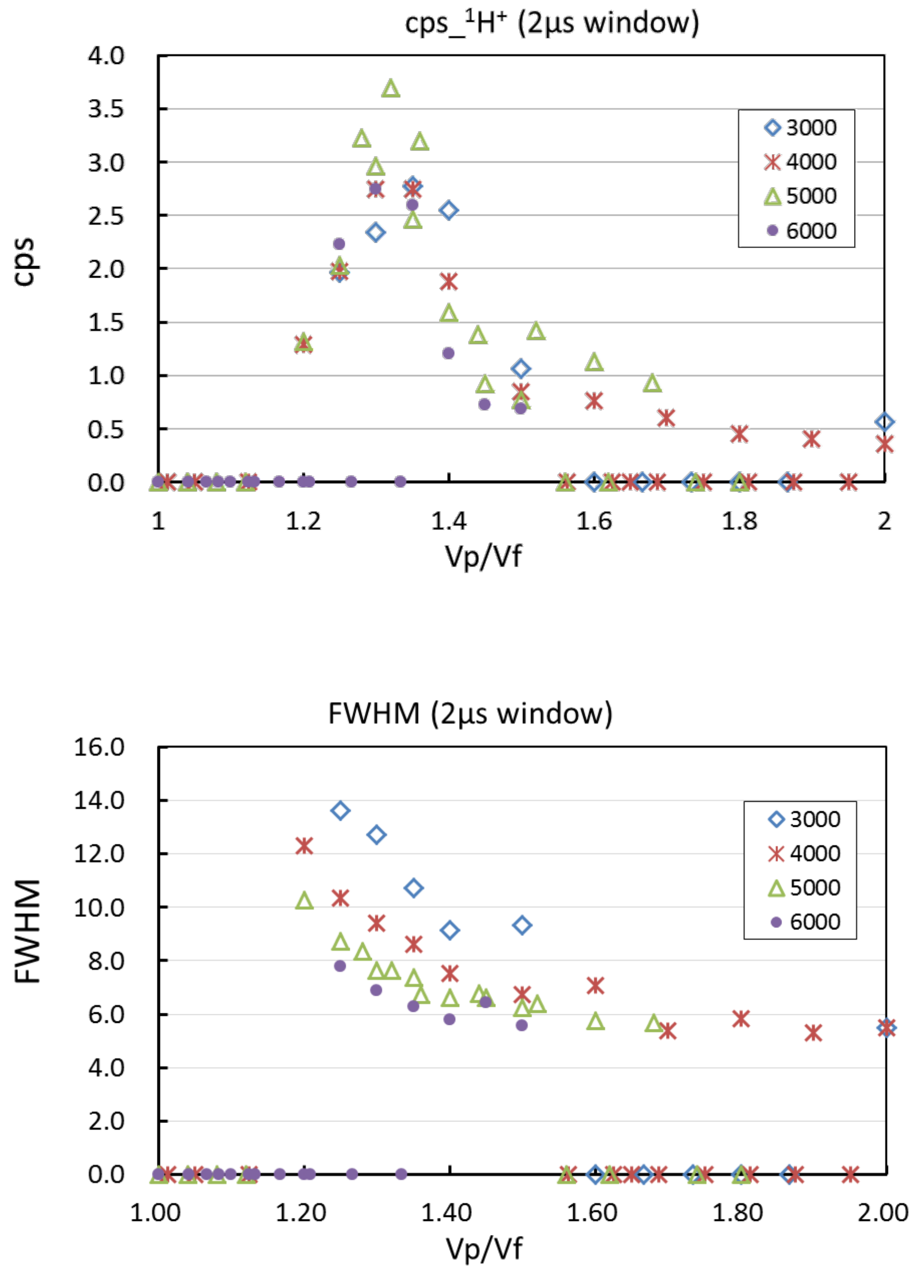

Fig. 4-31 Relation between acceleration voltage ratio (Vp/Vf) and ion yield of ^{1}H$^+$ (top), FWHM (bottom), (Vfloat 3000V, 4000V, 5000V, 6000V, D=963 mm).

The results showed that the yield (cps) of $^1H^+$ depends on V_p/V_f ratio regardless of absolute value of the acceleration voltages (V_p, V_f). It was consistent with results of Examination I to III. Although it was not remarkable, the resolution (FWHM) results also depended on the V_p/V_f ratio.

Resolution of $^1H^+$ peak was determined as Δm, in the 4 V_f conditions (3000 V, 4000 V, 5000 V, 6000 V). V_p was set so that V_p/V_f becomes 1.25, 1.30, and 1.35, at each V_f condition. That is, there were total 12 conditions. Results are summarized in Table 4-13 and 4-14, and magnified views of around $^1H^+$ peak is shown in Fig.4-31.

Table 4-13 Relation between acceleration voltage ratio (Vp/Vf) and resolution (Δm: FWHM) of $^1H^+$.

	Vp/Vf		
	1.25	1.3	1.35
Vf=3000	0.0056	0.0053	0.0046
Vf=4000	0.0049	0.0044	0.0042
Vf=5000	0.0046	0.0041	0.0041
Vf=6000	0.0045	0.0041	0.0038

Table 4-14 Relation between acceleration voltage ratio (Vp/Vf) and resolution (Δm/m = R) of $^1H^+$.

	Vp/Vf		
	1.25	1.3	1.35
Vf=3000	180.0	188.4	219.2
Vf=4000	204.8	229.0	235.7
Vf=5000	216.4	242.3	244.5
Vf=6000	221.2	243.8	262.3

While the acceleration voltage (both V_p and V_f) was increased, the resolution was gradually improved. In the conditions of $V_f \geq 4000$ V, resolutions (Δ m/m) became over 191, accomplished the required resolution. It is considered to be reasonable result was obtained, for the beam experiment in J-PARC.

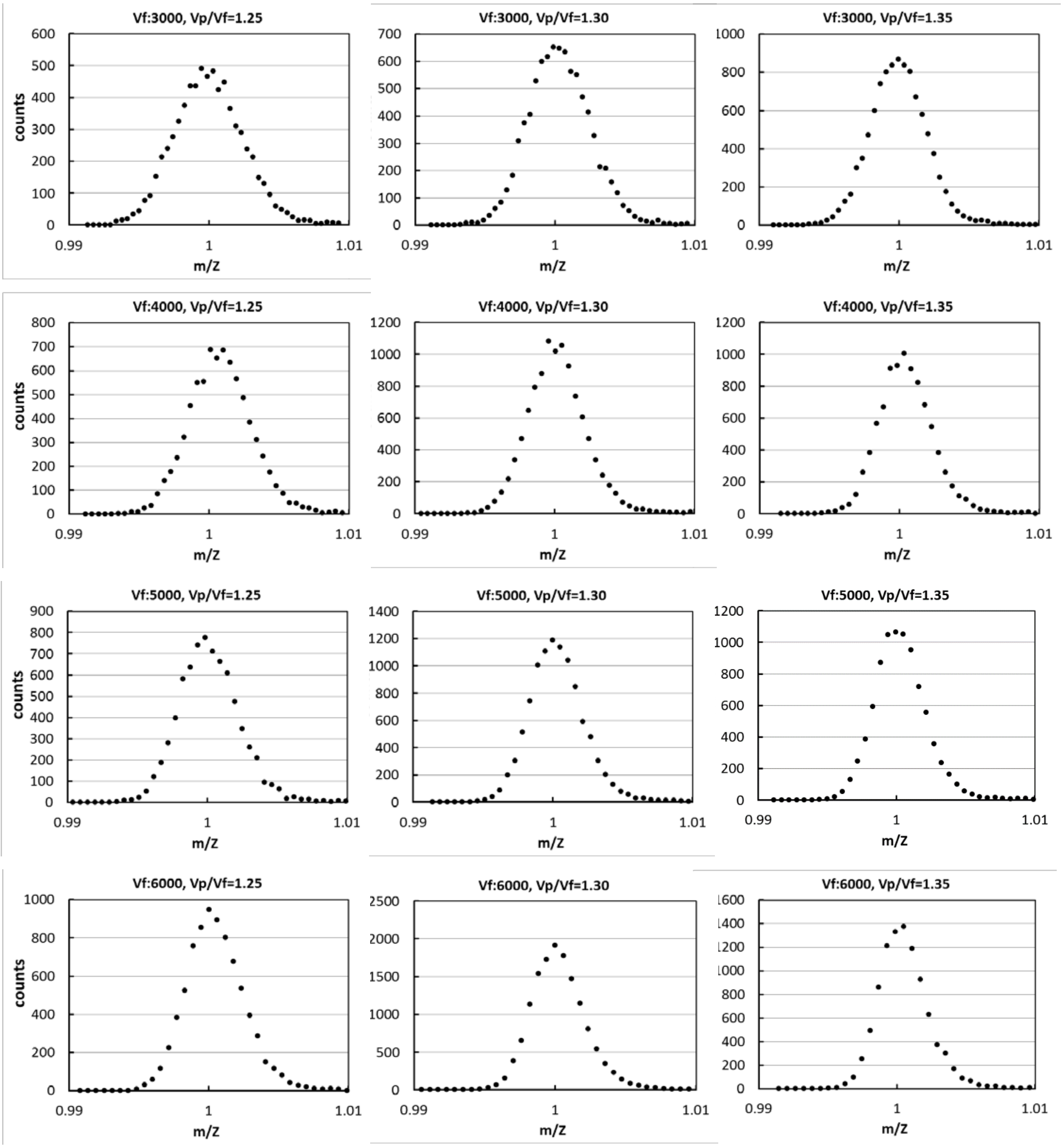

Fig. 4-31 Peaks of $^1H^+$ at various acceleration voltage conditions.

4.4 Improvement of the experimental system

It was found there were many background noises attributed to muon beam irradiation, in the muon beam experiment. In this section, muonic atom beam bending function by static electric field was developed and installed in the experimental system to reduce the noises. There are two ways to bend electrically charged particles, one is a method by electric field, the other is using magnetic field. The method using electric field has simpler structure than that of magnetic field, and bending trajectory of particles do not depend on particle mass as long as particle charge is same. Therefore, beam bending by electric field is not only a way to reduce background noises, but an optimal way to verify the charge of the generated particles.

4.4-1 Pre-estimation for bending electrode

For rough estimation for bending electrode shape and particle tracks, simulation for charged particle transportation by SIMION ver. 8.1 (purchased by Scientific Instrument service, U.S.) was performed. Fig. 4-32 shows the estimated particle tracks of 1H+ (initial kinetic energy is 4 keV) bended by facing plate electrodes (distance between electrode is 5cm, +3000 V is applied on the upside plate). It was found that particles have objective energy can be bent easily, even with such a simple structure electrode.

Fig. 4-32 Calculation result of particle tracks by SIMION, $^{1}H^{+}$ comes from left side of picture and bend by electric field of facing electrodes.

4.4-2 Development for muonic atom bending system

From the result of pre-estimation for shape of bending electrode, whole components for muoonic atom beam bending were developed and installed in the experimental system, component layout drawing is shown in Fig. 4-32. Bending electrode consists of two electrode plates made of aluminum and insulators made of PTFE, as shown in Fig. 4-33. High voltage power supply: HMBR-10P0.7, same as used for acceleration electrodes, was connected to one side of the electrode plates.

The bend angle of beam was determined as 30° so that emitted particles from the target material cannot get into detector directly. So the noise particles (accompanied electrons with muon beam, muon decay electrons, and photons) have very high energy (around 10^6 MeV), that heavy and thick materials are required to shield them. According to the estimation for shielding noise particles by phits, it was found that over 100 mm of lead is required to shield them completely (Fig. 4-34). A space between chamber 1 and 2 in Fig. 4-32, lead blocks are installed to shield noise particles, when a beam experiment.

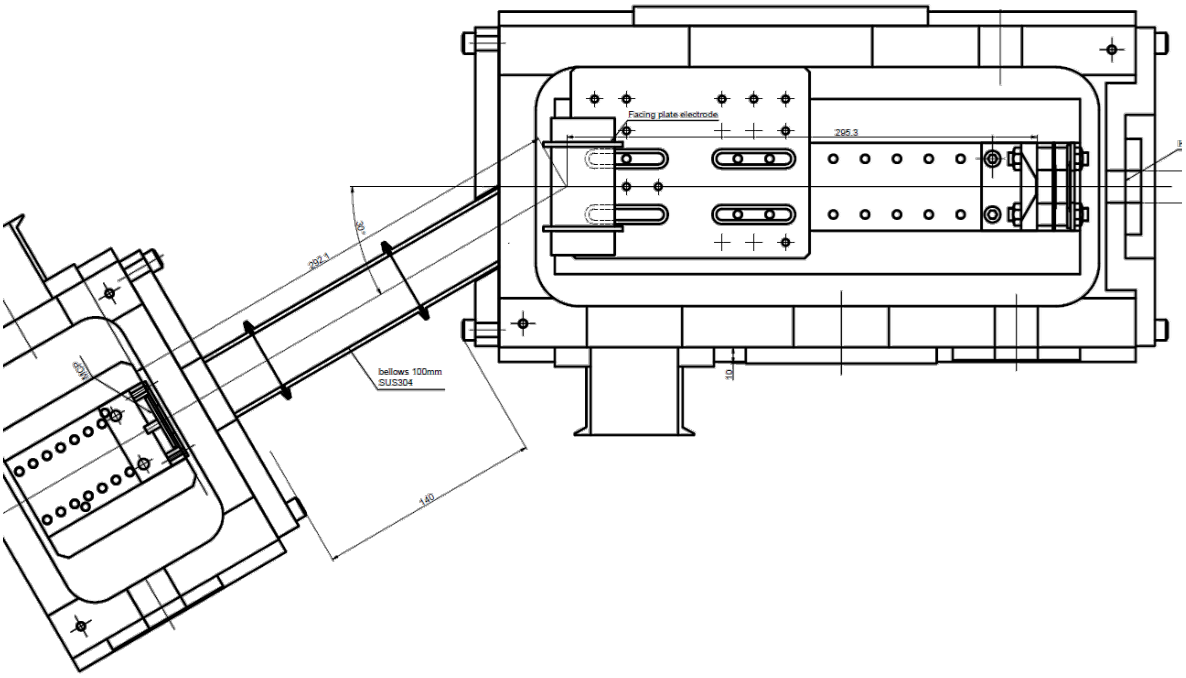

Fig. 4-32 component layout drawing for muonic atom beam bending system

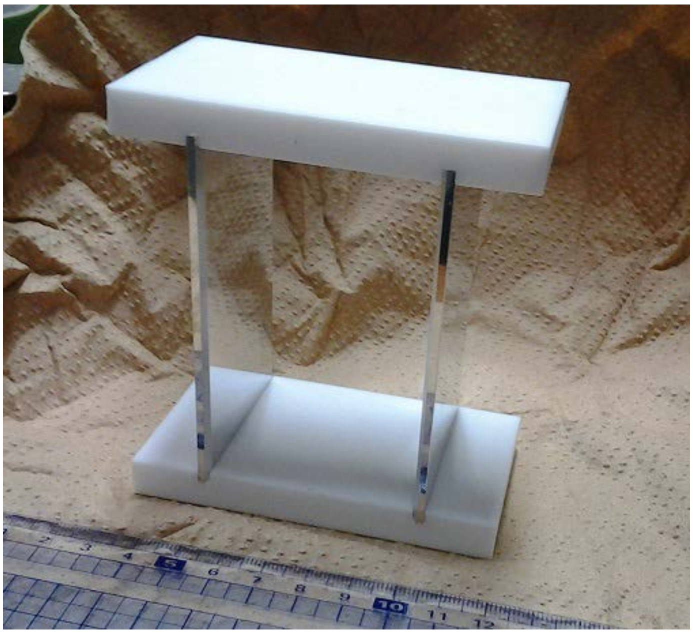

Fig. 4-33 Bending electrodes for muon beam deflection.

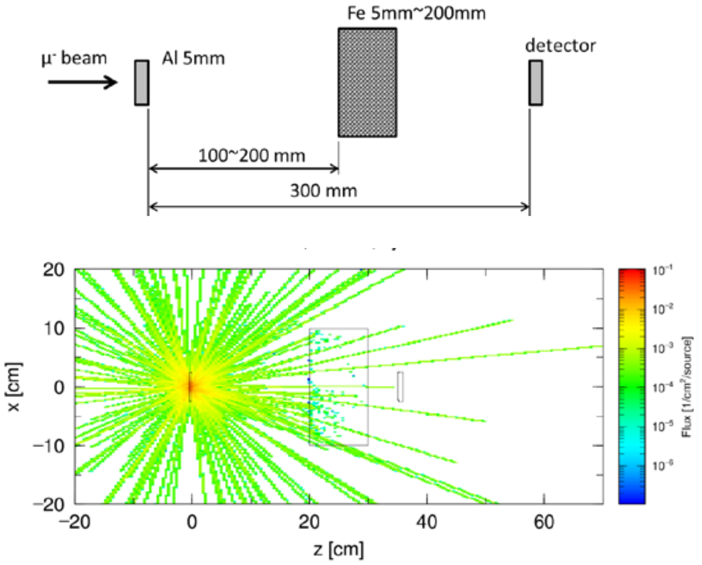

Fig. 4-34 Estimation of background noises attributed to muon decay electrons by Phits code.

Similarly to the pre-examinations, laser ablation experiments were performed to optimize the bending voltage system. Data acquisition system was same as the pre-examination I~III (data taking by oscilloscope). 200 μm thickness of copper plate was used as the target, and laser output was fixed to SW40000. The V_{float} was assigned to 4 conditions (750 V, 1500 V, 3000 V, 4500 V), and TOF spectra were obtained while changing the V_{push} so that V_p/V_f become 1.33, at each V_{float} condition.

Relationship between bending electrode voltage and peak height was investigated for $^{39}K^+$ (the largest peak) in all TOF spectra. As representative, the result from Vf = 3000 V is shown in Fig 4-35, and it showed the maximum value for ion yield at 3150 V of bending electrode voltage. This result corresponded to estimated value by SIMION, and it suggested the bending electrode manufactured properly.

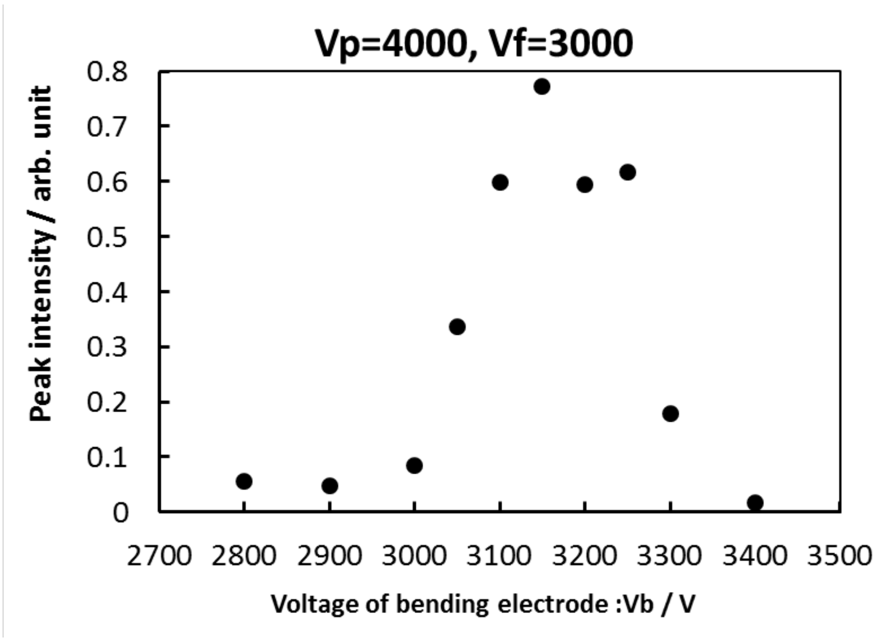

Fig. 4-35 Relation between bending voltage (Vb) and peak height, (V_{push} 400V, V_{float} 3000V).

4.5 Muon beam experiment

In this section, experimental setup and results of the beam experiments at J-PARC in June 2016 (2015A0237), and December 2016 (2016A0295) were described. The experiments were performed at 18/June/2016 to 20/June/2016, and 3/December/2016 to 5/December/2016, respectively. Aims of this experiment were to observe the signals attributed to the muonic atom, and to verify charge distribution of muonic fluorine atoms.

4.5-1 Experimental setup

The experimental setup was established as shown in Fig.4-36, and overview of setup in J-PARC is shown in Fig.4-37. The muon beam comes from the upside of Fig 4-36, and entered vacuum chamber, stops in the target material. In the target, muons are captured by target material and muonic atoms were formed. Muonic atoms formed very close to the target are considered to be escaped out from the target surface by Coulomb explosions. The muonic atoms which are created by the target are accelerated by electric fields of acceleration electrode, and deflected to 30° by electric field of bending electrode, and finally reach the detector (MCP).

Muon beam intensity strongly depends on momentum (energy) of muonic atom beam. Beam degrader made of aluminum plates which modify muon beam momentum were used so that muons can stop in the target properly, when the muon beam momentum was large.

Two germanium detectors shown in Fig. 4-36 were used to detect photon signal attributed to muonic atom beam generation. One which directs to the target was used to observe muonic K_α X-ray from muonic fluorine (168 keV), and estimate the stop position of muon within the target. The other one which directs to the MCP was used to observe prompt gamma rays emitted from excited oxygen atom ($^{19}O^*$) generated by orbital muon absorption by the fluorine nucleus. Some muonic fluorine atom arrived at MCP transforms to $^{19}O^*$, and immediately emits prompt gamma rays of energies described in Table 4-15 [70]. After prompt X-ray emission from $^{19}O^*$, gamma rays from ^{19}O whose energies is described in Table 4-16 are emitted with half-life of 26 second [71]. These prompt gamma rays and gamma rays can be used as evidence that muon atoms properly came.

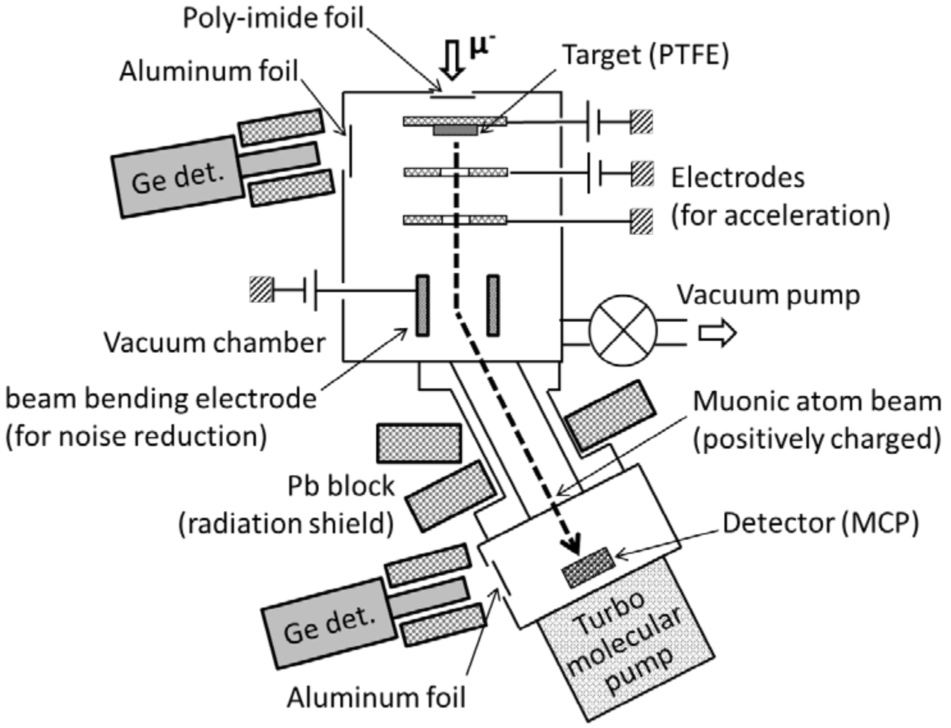

Fig. 4-36 Schematic view of experimental setup of 2015A0237 (Dec. 2016).

Fig. 4-37 Overview of experimental setup of 2015A0237 (Dec. 2016).

Table 4-15 Prompt γ-ray energies of $^{19}O^*$ [70].

E_γ / keV	I_γ / %
96.0	100
1375.7	98.0
1471.7	2.0
1595.7	100
2371.5	100
2473.2	28
2779.0	100
3057.5	92
3153.5	8
3848.9	39
3944.9	33

Table 4-16 γ-ray energies of $^{19}F^*$ (^{19}O) [71].

E_γ / keV	I_γ / %
109.9	2.54
197.1	95.9
1149	5E-4
1236	0.0170
1356.8	50.4
1444.1	2.64
1554.0	1.39
2354.0	0.00181
2582.5	0.0189
3710.6	0.00110
3797.9	0.00133
3907.7	0.00384
4180.1	0.0792

4.5-2 Experimental result

First, the result of the first experiment (2015A0237) is discussed. In this condition, beam bending system had not been installed, thus the beam track of muonic atom was straight. At the beginning of the experiment, muon beam irradiation with beam momentum of 22 MeV/c was performed. However, background noises attributed to muon beam were too much to determine whether the muon atoms were coming or not. Muon beam momentum was increased to 30~40 MeV/c, to irradiate more intense muon beam. In these conditions, optimization of the muon stop position in the target by changing degrader thickness was performed, and determined optimal muon beam momentum from intensity of μF-K_α (170.0 keV, shown in Fig. 4-38).

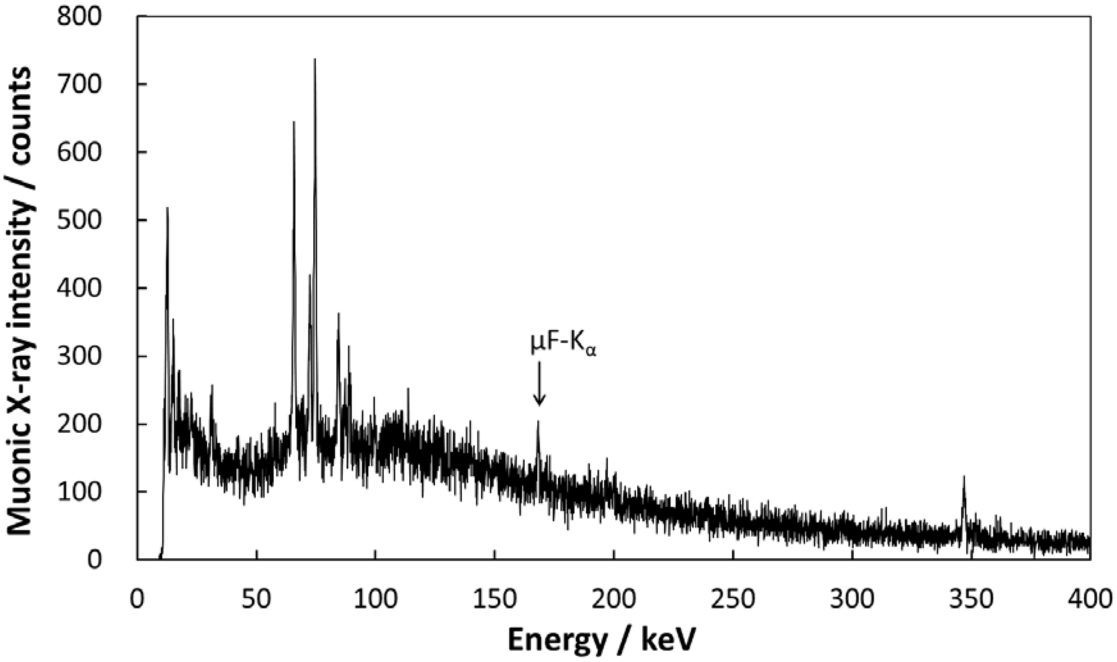

Fig. 4-38 Muonic X-ray spectrum of PTFE target, the peak of μF-K_α (170.0 keV) is found in the spectrum.

Also, Incident angle of muon was changed 0° (perpendicular irradiation to the target surface) to 5° to reduce noises, and a collimator (20mm diameter) was installed at the muon beam entrance window, but remarkable effect was not appeared. Finally, target was changed to copper plate used in the pre-examination, and the flight distance was shortened from 963 mm to 538 mm to increase the chance of entrance for muonic atom to detector. Conditions of no acceleration voltage applied were performed to confirm the difference from the condition of acceleration voltage was applied.

The beam bending system which is described in chapter 4-4 was applied in second experiment (2016A0295). The all experiments were performed under the condition of 40 MeV/c of muon beam momentum to obtain good statistical data. Same as previous experiment, optimization of the muon stop position in the target was performed. However, μF-K_α peak did not clearly appear in the muonic X-ray spectrum and the optimal condition had not been able to be found. Then, the bending electrode voltage was varied, and the TOF spectra were obtained.

As a result of this experiment, it was succeeded to reduce background noises significantly (two orders of magnitude compared with the previous spectrum) by using beam bending system, shown in Fig.4-39. However, no peak appeared in the estimated m/z region attributed to muonic atom ions, and also no significant difference appeared in both applied/no acceleration voltage conditions. The system has sufficient performance for muonic atom extraction and charge separation however the signal which is originated from muonic atom could not be detected. It is considered that the muon beam intensity is insufficient to generate the muonic atom beams. There is another problem, the mechanism how muonic atoms generate from the target material has not been revealed.

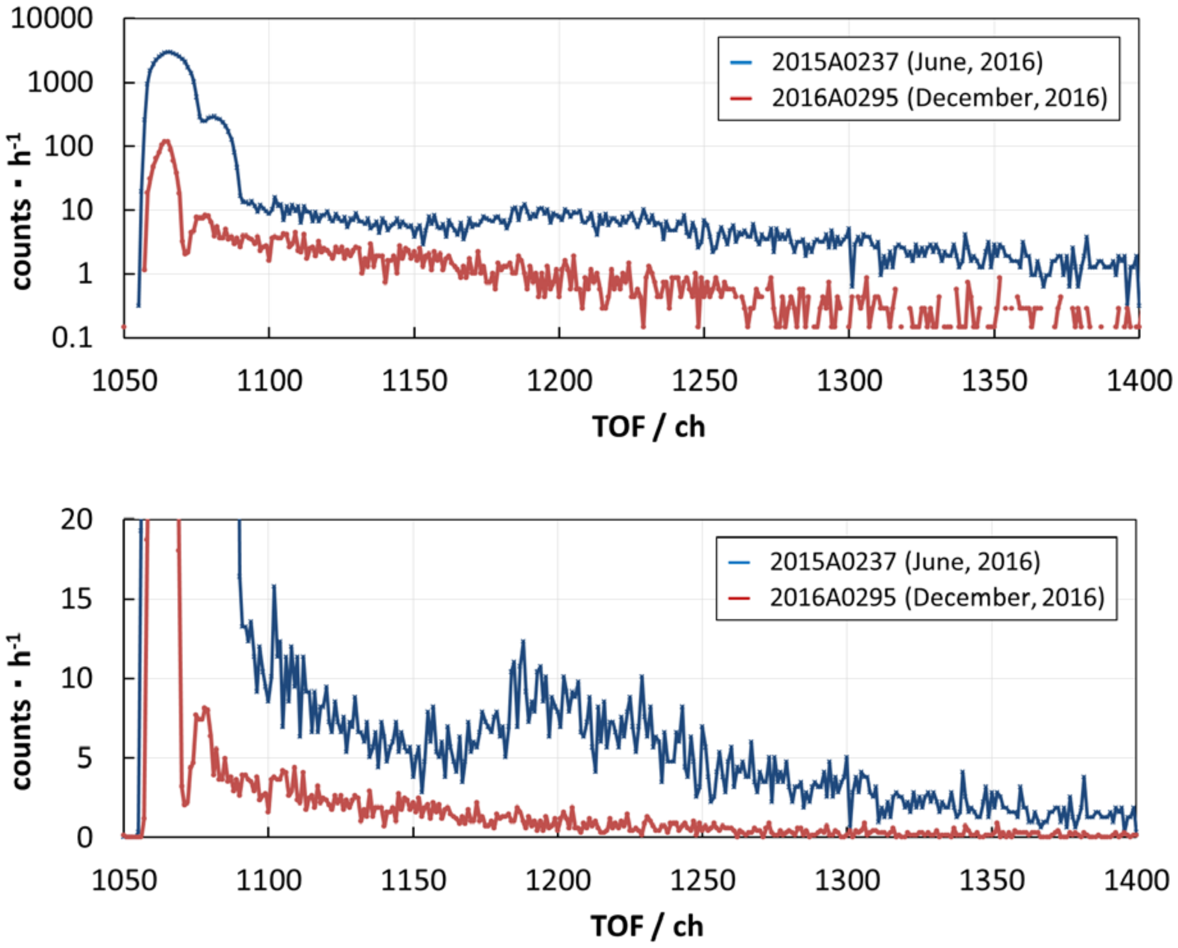

Fig. 4-39 Comparison between TOF spectrum in 2015A0237 (blue ×) and 2016A0295 (red ●). In the spectrum of 2016A0295, background noises were reduced two orders of magnitude compared with the spectrum of 2015A0237.

Chapter5. Concluding remarks

In this thesis, revealing the muonic atom formation process comprehensively was set as the major aim, and the two research themes were performed for this porpose. One is the investigation of the chemical environmental effect on muonic atom formation by muon irradiation for low pressure gases and muonic X-ray measurement. Another is the development of the muonic atom extraction and charge separation system. In conclusion, the chemical enveironmental effect on muonic atom formation was found in CO, CO_2, COS, and CS_2 molecules, and the muonic atom extraction system was developed and preliminary studies were performed using the system. Details of the two research results are mentioned in the below.

1. Investigation of the chemical environmental effect on muonic atom formation by muon irradiation for low pressure gases

For investigating the chemical environmental effect in muonic atom formation process, muon beam irradiation experiments for the low pressure gas samples (CO, CO_2, COS, and CS_2) and and the hydrogen mixture gases (H_2+CO, H_2+CO_2, H_2+COS, and H_2+CS_2) were performed in J-PARC MUSE-D1, and obtaind muonic X-ray spectra of carbon, oxygen, and sulfur atoms in these molecules.

Muon capture ratios of the carbon atom to the oxygen atom “A(C/O)”, the sulfur atom to the oxygen atom “A(S/O)”, and the sulfur atom to the carbon atom “A(S/C)”, were determined precisely from the muonic X-ray intensities of the Lyman series. The numbers of electrons which influence the muon capture were estimated based on calculations using the LMM model. The parameters (n_C, n_O, n_S, m_C, m_O, m_S, and v) were adjusted to explain A(C/O), A(S/O), and A(S/C), for all samples, consistently. The calculation results suggested that the muon capture might be influenced by the lone pair electrons on the carbon atom, when the muon was captured by carbon atom in CO molecule.

Muonic X-ray structures were deduced from muonic X-ray spectra. From both Lyman series and Balmer series X-rays from carbon, oxygen, and sulfur atom, initial angular momentum quantum number distributions of captured muon were estimated by a cascade calculation program. It was revealed that the valence electron state and constituent atom had an influence on the muon capture probability and the quantum state (n, l) of muon just after muon capturing, in a case of a muon captured by CO, CO_2 and COS molecules respectively. Espescially, the lone pair electrons on carbon atom in CO molecule had a large contribution to muon capture process. Differences in muon capture process between CO_2 and COS were not large, although numbers of orbital electrons and atomic radii of oxygen atom and sulfur atom are quite different. We quantified the influence of the lone pair electrons on carbon atom in CO molecule from the muon capture probability and the initial angular quantum number distribution. Such a discussion have never been reported, and it proved the lone pair electrons on carbon atom in CO molecule played an important role in a case of a muon captured by carbon atom in CO, CO_2 and COS molecules.

Muon capture ratios and muonic X-ray structures were deduced from muonic X-rays which were emitted after the muon transfer from muonic hydrogen (H_2+CO, H_2+CO_2, H_2+COS, and H_2+CS_2). The muon capture ratios for the muon transfer process were different from the capture ratios of the direct muon capture process, which were obtained from the experiment using CO and CO_2 gases. The muon capture ratios and muonic X-ray structures from the H_2+CO and H_2+CO_2 samples were statistically similar, regardless of the differing molecular structure. On the other hand, the muon capture ratio A(S/C) for H_2+COS and H_2+CS_2 samples were differnet each other.

2. Development of the muonic atom extraction and charge separation system

For verifying what state the muonic atom has at the initial stage of its formation, we aimed to establish the observation method for the muonic atom ion after its formation. As the first step, charge separation system for muonic atomic ions had developed, based on the TOF mass spectrometer. In the system, muonic florine atom ions were extracted from PTFE target and accelerated by electric fields. Valence of the muonic fluorine atom might be shown in TOF spectrum as mass to charge ratio: *m/z*.

Optimization of the muonic atom extraction system had been performed by laser irradiation for metal plates. Various ions were generated from the target surface and accelerated by electric fileds. From the optimization result, mass resolution R > 260 was achieved and this was sufficient to distinguish fluorine atom (19.0 u) and muonic fluorine atom (19.1 u).

Preliminary experiments using muon beam were carried out at J-PARC MUSE-D2. Background noises originated from various particles which were accompanied to muon beam were observed, although we succeeded to remove these noises significantly by improving the experimental system. The system has sufficient performance for muonic atom extraction and charge separation however the signal which is originated from muonic atom could not be detected. It is considered that the muon beam intensity is insufficient to generate the muonic atom beams. There is another problem, the mechanism that muonic atom ions emerge from the target material has not been revealed. The theoretical approach is required to reveal the mecanisum of muonic atom generation not only experimental approach.

References

1. S. H. Neddermeyer and C.D. Anderson, Phys. Rev. **51**, 884 (1937).
2. Fermilab, Office of Science, United States Department of Energy, Particle
3. M. Conversi, E. Pancini and O. Piccioni, Phys. Rev. **71**, 209 (1947).
4. E. Fermi and E. Teller, Phys. Rev. **72**, 399 (1947).
5. H. Schneuwly and P. Vogel, Phys. Rev. A **22**, 2081 (1980).
6. K. Ninomiya, H. Sugiura, T. Nakatsuka, Y. Kasamatsu, H. Kikunaga, W. Sato, T. Yoshimura, H. Matsumura, K. Takamiya, M. K. Kubo, K. Sueki, A. Yokoyama, Y. Hamajima, T. Miura, K. Nishiyama and A. Shinohara, J. Radioanal. Nucl. Chem. **272**, 661 (2007).
7. D. J. Arseneau, D. G. Fleming and O. Sukhorukov, Physica B **404**, 946 (2009).
8. V. W. Hughes and C. S. Wu, Muon Physics(1). Academic Press, USA, (1977).
9. J. C. Sens, Phys. Rev. **113**, 679 (1959).
10. R. Callies, H. Daniel, F.J. Hartmann and W. Neumann, Phys. Lett. A **91**, 441 (1982).
11. V. R. Akylas and P. Vogel, Computer Physics Communications **15**, 291 (1978).
12. P. Vogel, Phys. Rev. A**22**, 1600 (1980).
13. H. Schneuwly, M. Boschung, K. Kaeser, G. Piller, A. Ruetschi, L. A. Schallcr and L. Schellenberg, Phys. Rev. A**27**, 950 (1983).
14. V. I. Petrukhin and V. M. Suvorov, Zh. Éksp. Teor. Fiz. **70**, 1145 (1976). [Sov. Phys. JETP **43**, 595 (1976).]
15. L. H. Thomas, Proc. Cambridge Phil. Soc. **23**, 542 (1927).
16. E. Fermi, Rend. Accad. Naz. Lincei. **6**, 602 (1927).
17. H. Daniel, Phys. Rev. Lett. **35**, 1649 (1975).

18. H. Daniel, Z. Physik A **291**, 29 (1979).

19. H. Daniel, W. Denk, F. J. Hartmann, and W. Wilhelm, Phys. Rev. Lett. **41**, 853 (1978).

20. W. K. H. Panofsky, R. L. Aamodt and J. Hadley, Phys. Rev. **81**, 565 (1951).

21. N. P. Samios, Phys. Rev. Lett. **4**, 470 (1960).

22. L. I. Ponomarev, Ann. Rev. Nucl. Sci. **23**, 395 (1973).

23. H. Schneuwly, V. I. Pokrovsky and L. I. Ponomarev, Nucl. Phys. A**312**, 419 (1978).

24. T. Suzuki, R.J. Mikula, D.M. Garner, D.G. Fleming and D.F. Measday, Phys. Lett. B **95**, 202 (1980).

25. N. Imanishi, T. Furuya, I. Fujiwara, A. Shinohara, H. Kaji, and S. Iwata, Phys. Rev. A**32**, 2584 (1985).

26. N. Imanishi, T. Fukumura, A. Shinohara, and H. Kaji, Phys. Rev. A**35**, 2044 (1987).

27. J. D. Knight, C. J. Orth, M. E. Schillaci, R. A. Naumann, F. J. Hartmann and H. Schneuwly, Phys. Rev. A**27**, 2936 (1983).

28. P. Ehrhart, F. J. Hartmann, E. Köhler, H. Daniel, Z. Phys. A**311**, 259 (1983).

29. R. Bacher, P. Blüm, D. Gotta, K. Heitlinger, and M. Schneider, Phys. Rev. A**39**, 1610 (1989).

30. V. E. Markushin, Phys. Rev. A**50**, 1137 (1994).

31. P. Hauser, K. Kirch, F. Kottmann and L.M. Simon, Nucl. Instr. Meth. Phys. Res. A **411**, 389 (1998).

32. K. Kirch, P. Hauser, F. Kottmann and L. M. Simons, Hyperfine Interact. **119**, 83 (1999).

33. K. Kirch, D. Abbott, B. Bach, P. Hauser, P. Indelicato, F. Kottmann, J. Missimer, P. Patte, R. T. Siegel, L. M. Simons and D. Viel, Phys. Rev. A**59**, 3375 (1999).

34. K. Ninomiya, T. U. Ito, W. Higemoto, M. Kita, A. Shinohara, T. Nagatomo, M. K. Kubo, P. Strasser, N. Kawamura, K. Shimomura, Y. Miyake and T. Miura, J. Korean Phys. Soc. **59**, 2917 (2011).

35. A. Shinohara, T. Muroyama, J. Shintai, E. Taniguchi, T. Saito, T. Miura, N. Imanishi, Y. Yoshimura and M. Furukawa: Hyperfine Interact. **84**, 569 (1994).

36. A. Shinohara, T. Muroyama, J. Shintai, J. Kurachi, M. Furukawa, T. Miura, Y. Yoshimura, T. Saito, T. Ohdaira and N. Imanishi: Phys. Rev. A **53**, 130 (1996).

37. A. Shinohara, T. Muroyama, C. Murata, T. Miura, T. Saito, A. Yokoyama, S. Kojima and M. Furukawa: Phys. Rev. Lett. **76**, 2460 (1996).

38. A. Shinohara, T. Muroyama, T. Miura, T. Saito, A. Yokoyama and M. Furukawa: Hyperfine Interact. **106**, 301 (1997).

39. J-PARC center: https://j-parc.jp/en/jparc.html

40. S. Nagamiya, Prog. Theor. Exp. Phys. **2012**, 02B001 (2012).

41. R. Kadono and Y. Miyake, Rep Prog Phys **75**, 026302 (2012).

42. Y. Miyake, K. Shimomura, N. Kawamura, P. Strasser, A. Koda, S. Makimura, H. Fujimori, Y. Ikedo, K. Nakahara, S. Takeshita, M. Kato, K. Kojima, Y. Kobayashi, K. Nishiyama, R. Kadono, W. Higemoto, T. U. Ito, K. Ninomiya, M. K. Kubo and K. Nagamine, Physics Procedia **30**, 46 (2012).

43. S. Makimura, N. Kawamura, Y. Kobayashi, Y. Ikedo, R. Kadono, A. Koda, K. M. Kojima, K. Shimomura, P. Strasser, Y. Nakatsugawa, H. Fujimori and Y. Miyake "Installation of Rotating Target at J-PARC/MLF/MUSE" Annual meeting of the Physical Society of Japan (2015).

44. P. Strasser, K. Shimomura, A. Koda, N. Kawamura, H. Fujimori, S. Makimura, Y. Kobayashi, K. Nakahara, M. Kato, S. Takeshita, M. Hiraishi, M. Miyazaki, W. Higemoto, T. U. Ito, K. Ninomiya, K. Ishida, M. K. Kubo, R. Kadono, K. Nishiyama and Y. Miyake, J. Phys. Conf. Ser. **225**, 012050 (2010).

45. J-PARC center: http://j-parc.jp/researcher/MatLife/en/instrumentation/ms3.html

46. K. M. Kojima, T. Murakami, Y. Takahashi, H. Lee, S. Y. Suzuki, A. Koda, I. Yamauchi, M. Miyazaki, M. Hiraishi, H. Okabe, S. Takeshita, R. Kadono, T. Ito, W. Higemoto, S. Kanda, Y. Fukao, N. Saito, M. Saito, M. Ikeno, T. Uchida and M. M. Tanaka, J. Phys. Conf. Ser. **551**, 012063 (2014).

47. H. Hirayama, Y. Namito, A. F. Bielajew, S. J. Wilderman and W. R. Nelson, SLAC-R 730 (Stanford Linear Accelerator Center, Stanford, CA, 2005)

48. K. ninomiya, List of Muonic X-ray energies and binding energy of muon, (Unpublished)

49. A. Werthmuller, A. Adamczak, R. J. Guillarmod, F. Mulhauser, C. Piller, L. A. Schaller, L. Schellenberg, H. Schneuwly, and Y. A. Thalmann, Hyperfine Interact. **103**, 147 (1996).

50. F. Mulhauser, H. Schneuwly, J. Phys. B**26**, 4307 (1993).

51. M. K. Kubo, Y. SAKAI, T. Tominaga and K. Nagamine, Radiochim. Acta **47**, 77 (1989).

52. G. Yoshida, K. Ninomiya, T. U. Ito, W. Higemoto, T. Nagatomo, P. Strasser, N. Kawamura, K. Shimomura, Y. Miyake, T. Miura, K. M. Kubo and A. Shinohara, J. Radioanal. Nucl. Chem. **303**, 1277 (2015).

53. J. E. Huheey, Inorganic Chemistry. Harper & Row publishers, USA, (1983).

54. Y. Jean, F. Volatron, An Introduction to Molecular Orbitals. Oxford University Press, UK, (1993).

55. V. E. Markushin, Hyperfine Interact. **119**, 11 (1999).

56. G. R. Burbidge, and A. H. de Borde, Phys. Rev. **89**, 189 (1953).

57. D. Kessler, H. L. Anderson, M. S. Dixit, H. J. Evans, R. J. McKee, C. K. Hargrove, R. D. Barton, E. P. Hincks and J. D. McAndrew, Phys. Rev. Lett. **18**, 1179 (1967).

58. F. J. Hartmann, T. von Egidy, R. Bergmann, M. Kleber, H.-J. Pfeiffer, K. Springer, and H. Daniel, Phys. Rev. Lett. **37**, 331 (1976).

59. K. O'Leary and Daphne F. Jackson, Z. Phys. A**320**, 551 (1985).

60. T. Siems, D. F. Anagnostopoulos, G. Borchert, D. Gotta, P. Hauser, K. Kirch, L. M. Simons, P. El-Khoury, P. Indelicato, M. Augsburger, D. Chatellard, and J. -P. Egger, Phys. Rev. Lett. **84**, 4573 (2000).

61. R. Jacot-Guillarmod, F. Bienz, M. Boschung, C. Piller, L. A. Schaller, I. Schellenberg, H. Schneuwly, and D. Sirsdovic, Phys. Rev. A**37**, 3795 (1988).

62. H. Ryufuku, K. Sasaki, and T. Watanabe, Phys. Rev. A **21**, 745 (1980).

63. R. Bacher, D. Gotta, L. M. Simons, J. Missimer, and Nimai C. Mukhopadhyay, Phys. Rev. Lett. **54**, 2087 (1985).

64. W.C. Wiley, and I.H. Mclaren, Rev. Sci. Instrum. **26**, 1150 (1955).

65. M. Hashida, H. Mishima, S. Tokita, and S. Sakabe, Optics Express **17**, 13116 (2009).

66. K. K. Okudaira, E. Kobayashi, S. Kera, K. Mase, and N. Ueno, Surface science **593**, 297 (2005).

67. A. Palov, H. Fujii, Yu. Mankelevich, T. Rakhimova, and M. Baklanov, Polym. Degrad. Stab. **97**, 802 (2012).

68. T. Sato, K. Niita, N. Matsuda, S. Hashimoto, Y. Iwamoto, S. Noda, T. Ogawa, H. Iwase, H. Nakashima, T. Fukahori, K. Okumura, T. Kai, S. Chiba, T. Furuta and L. Sihver, Particle and Heavy Ion Transport Code System PHITS, Version 2.52, J. Nucl. Sci. Technol. **50**, 913 (2013).

69. Japan Radioisotope association, Radio isotope pocket data book 11. Maruzen, Japan, (2011).

70. S.Y.F. Chu, L.P. Ekström, and R.B. Firestone, The Lund/LBNL Nuclear Data Search ver.2.0, Feb. 1999: http://nucleardata.nuclear.lu.se/toi/

71. IAEA - Nuclear Data Section, nuclear structure and decay data: https://www-nds.iaea.org

Appendix. List of the energy state of muonic atom

The energy state of the muonic carbon, muonic oxygen, and muonic sulfur atoms are summarized in Table A-1 ~ A-3. The values were caluculated by the Dirac equation. The energy of muonic X-ray can be derived from the subtraction of the two energy states (the befrore transition, and the after transition).

Table A-1 The energy state of the muonic carbon (keV) [48]. The enery states of principal quantum number: *n* = 1 to 16, and angular momentum quantum number: *l* = 0 to 15, are summarized in this table. The values were caluculated by the Dirac equation.

		l															
		0	1	2	3	4	5	6	7	8	9	10	11	12	13	14	15
n	16	-0.39	-0.39	-0.39	-0.39	-0.39	-0.39	-0.39	-0.39	-0.39	-0.39	-0.39	-0.39	-0.39	-0.39	-0.39	-0.39
	15	-0.45	-0.45	-0.45	-0.45	-0.45	-0.45	-0.45	-0.45	-0.45	-0.45	-0.45	-0.45	-0.45	-0.45	-0.45	
	14	-0.51	-0.51	-0.51	-0.51	-0.51	-0.51	-0.51	-0.51	-0.51	-0.51	-0.51	-0.51	-0.51	-0.51		
	13	-0.59	-0.59	-0.59	-0.59	-0.59	-0.59	-0.59	-0.59	-0.59	-0.59	-0.59	-0.59	-0.59			
	12	-0.70	-0.70	-0.70	-0.70	-0.70	-0.70	-0.70	-0.70	-0.70	-0.70	-0.70	-0.70				
	11	-0.83	-0.83	-0.83	-0.83	-0.83	-0.83	-0.83	-0.83	-0.83	-0.83	-0.83					
	10	-1.00	-1.00	-1.00	-1.00	-1.00	-1.00	-1.00	-1.00	-1.00	-1.00						
	9	-1.24	-1.24	-1.24	-1.24	-1.24	-1.24	-1.24	-1.24	-1.24							
	8	-1.57	-1.57	-1.57	-1.57	-1.57	-1.57	-1.57	-1.57								
	7	-2.05	-2.05	-2.05	-2.05	-2.05	-2.05	-2.05									
	6	-2.79	-2.79	-2.79	-2.79	-2.79	-2.79										
	5	-4.02	-4.02	-4.02	-4.02	-4.02											
	4	-6.28	-6.28	-6.28	-6.28												
	3	-11.16	-11.16	-11.16													
	2	-25.12	-25.10														
	1	-100.5															

Table A-2 The energy state of the muonic oxygen (keV) [48]. The enery states of principal quantum number: n = 1 to 16, and angular momentum quantum number: l = 0 to 15, are summarized in this table. The values were caluculated by the Dirac equation.

		l															
		0	1	2	3	4	5	6	7	8	9	10	11	12	13	14	15
n	16	-0.70	-0.70	-0.70	-0.70	-0.70	-0.70	-0.70	-0.70	-0.70	-0.70	-0.70	-0.70	-0.70	-0.70	-0.70	-0.70
	15	-0.80	-0.80	-0.80	-0.80	-0.80	-0.80	-0.80	-0.80	-0.80	-0.80	-0.80	-0.80	-0.80	-0.80	-0.80	
	14	-0.91	-0.91	-0.91	-0.91	-0.91	-0.91	-0.91	-0.91	-0.91	-0.91	-0.91	-0.91	-0.91	-0.91		
	13	-1.06	-1.06	-1.06	-1.06	-1.06	-1.06	-1.06	-1.06	-1.06	-1.06	-1.06	-1.06	-1.06			
	12	-1.24	-1.24	-1.24	-1.24	-1.24	-1.24	-1.24	-1.24	-1.24	-1.24	-1.24	-1.24				
	11	-1.48	-1.48	-1.48	-1.48	-1.48	-1.48	-1.48	-1.48	-1.48	-1.48	-1.48					
	10	-1.79	-1.79	-1.79	-1.79	-1.79	-1.79	-1.79	-1.79	-1.79	-1.79						
	9	-2.21	-2.21	-2.21	-2.21	-2.21	-2.21	-2.21	-2.21	-2.21							
	8	-2.80	-2.80	-2.80	-2.80	-2.80	-2.80	-2.80	-2.80								
	7	-3.65	-3.65	-3.65	-3.65	-3.65	-3.65	-3.65									
	6	-4.97	-4.97	-4.97	-4.97	-4.97	-4.97										
	5	-7.16	-7.16	-7.16	-7.16	-7.16											
	4	-11.19	-11.19	-11.18	-11.18												
	3	-19.90	-19.89	-19.88													
	2	-44.78	-44.74														
	1	-179.1															

Table A-3 The energy state of the muonic sulfur (keV) [48]. The enery states of principal quantum number: *n* = 1 to 16, and angular momentum quantum number: *l* = 0 to 15, are summarized in this table. The values were caluculated by the Dirac equation.

		l															
		0	1	2	3	4	5	6	7	8	9	10	11	12	13	14	15
n	16	-2.81	-2.81	-2.81	-2.81	-2.81	-2.81	-2.81	-2.81	-2.81	-2.81	-2.81	-2.81	-2.81	-2.81	-2.81	-2.81
	15	-3.20	-3.19	-3.19	-3.19	-3.19	-3.19	-3.19	-3.19	-3.19	-3.19	-3.19	-3.19	-3.19	-3.19	-3.19	
	14	-3.67	-3.67	-3.67	-3.67	-3.67	-3.67	-3.67	-3.66	-3.66	-3.66	-3.66	-3.66	-3.66	-3.66		
	13	-4.25	-4.25	-4.25	-4.25	-4.25	-4.25	-4.25	-4.25	-4.25	-4.25	-4.25	-4.25	-4.25			
	12	-4.99	-4.99	-4.99	-4.99	-4.99	-4.99	-4.99	-4.99	-4.99	-4.99	-4.99	-4.99				
	11	-5.94	-5.94	-5.94	-5.94	-5.94	-5.94	-5.94	-5.94	-5.94	-5.94	-5.94					
	10	-7.19	-7.19	-7.19	-7.18	-7.18	-7.18	-7.18	-7.18	-7.18	-7.18						
	9	-8.88	-8.87	-8.87	-8.87	-8.87	-8.87	-8.87	-8.87	-8.87							
	8	-11.24	-11.23	-11.23	-11.23	-11.23	-11.22	-11.22	-11.22								
	7	-14.68	-14.67	-14.67	-14.66	-14.66	-14.66	-14.66									
	6	-19.99	-19.97	-19.96	-19.96	-19.96	-19.95										
	5	-28.80	-28.76	-28.75	-28.74	-28.74											
	4	-45.02	-44.94	-44.92	-44.90												
	3	-80.08	-79.90	-79.84													
	2	-180.3	-179.7														
	1	-720.8															

Acknowledgements

First, I would like to deeply express my gratitude to Professor Atsushi Shinohara (Graduate school of Science, Osaka University) for his constant support, direction, discussion, and encouragemenet thoroughout the course of this study.

I would like to express an acknowledgement to sub-chief examiners of this thesis. Professor Michio Okada (Graduate school of Science, Osaka University) gave kindly discussion and showed the direction, Professor Mitsutaka Okumura (Graduate school of Science, Osaka University) discussed and had interest in this thesis, and Professor Toshiyuki Azuma (RIKEN) gave an enlightening instruction and valuable discuttion.

I would like to deeply express my gratitude to Assitant Professor Kazuhiko Ninomiya for his valuable suggestions, discussions, and constant support on all of my research.

I would like to express grateful appreciation to my co-reserchers for many supports on the muon beam experiments at J-PARC, discussions, valuable advices, and continuous encouragements. Professor Yasuhiro Miyake (KEK) had always supported my experiments at J-PARC and given advices. Dr. Naritoshi Kawamura (KEK) also had given many supports, and valuable advices in my research and experimental method. Professor Kenya Kubo (International Christian University) had given many supports in muon beam experiments at J-PARC, and discussed about the research many time. Professor Koichiro Shimomura (KEK) had given supports in experiments at J-PARC, and discussed. Dr.Patrick Strasser (KEK) had given supports in experiments at J-PARC, and discussed. Professor Wataru Higemoto (JAEA) had given supports in experiments at J-PARC, valuable advices, and discussed. Dr. Takashi Ito (JAEA) had given supports

in experiments at J-PARC. Professor Taichi Miura (KEK) had discussed, and given encouragement. Professor Michisato Toyoda (Graduate school of Science, Osaka University) had given valuable advices, and support in development of muonic atom beam extraction system. Dr. Jun Aoki (Graduate school of Science, Osaka University) had given many advices and supports for development of muonic atom beam experiment, and always discussed. I would like to express the deepest appreciation to Mr. Makoto Inagaki (Graduate school of Science, Osaka University) for his discussion, many supports in my resarch, and encouragement. I also would like to express appreciation to supporting staffs at J-PARC. Mr. Koji Hamada had always helped my experiments and given grateful supports. Dr. Motonobu Tampo and Mr. Shogo Doiuchi had supported experiments.

I would like to express grateful appreciation to Mr. Michio Sakamoto, and staffs of the Center for Scientific Instrument Renovation and Manufacturing Support. Without thier help, the system for muonic atom extraction has never been developed.

I'd llike to express my gratitude to Assistant Professor Yoshitaka Kasamatsu (Graduate school of Science, Osaka University) for his support, discussions, and encouragement. I I'd llike to express my gratitude to Professor Takashi yoshimura (Graduate school of Science, Osaka University) for his valuable advice and discussion. Also I'd like to express ana appreciation to Assistant Professor Naruto Takahashi (Graduate school of Science, Osaka University) for his advice and discussion.

I'd llike to my gratitude to fellow reserchers and gratitudes of research group of secondary particle chemistry in the Laboratory of Radiochemistry for supports, discussions, valuable advices, and continuous encouragements. Mr. Akihiro Nanbu (Graduate school of Science, Osaka University) had supported in the beam experiment

in J-PARC and discussed. Mr. Kazuya Fujihara had discussed. Mr. Ryosuke Yasui had discussed. Mr. Michihiro Kitanaka had discussed. I would like to express the appreciation to Ms. Reiko Nakagaki for her advice and encouragement.

I'd llike to my gratitude to secretary of our laboratory: Ms. Kanako Kawase, for her support and encouragements. I also express my gratitude to many fellows and graduates of Laboratory of Radiochemistry, Dr. Zijian Zhang, Mr. Keigo Toyomura, Mr. Yuki Yasuda, Mr. Kohei Nakamura, Dr. Hayato Ikeda, Dr. Yukiko Komori, Dr. Takuya Yokokita, Ms. Mai Eguchi, Ms. Aiko Kino, Mr. Tatsuki Shiroyama, Mr. Yoshihiko Hayashi, Mr. Keisuke Morimoto, Ms. Moe Seike, Mr. Shunsuke Kakitani, Mr. Yudai shigekawa, Ms. Shizuka Matsunaga, Mr. Yuji Osumi, Ms. Anna Suzuki, Mr. Kohki Ouchi, Mr. Akimitsu Kanda, Ms. Narumi Kondo, Mr. Nobufumi Fujita, Mr. Takumi Ikeda, Mr. Yuki Inai, Mr. Masahiro Nagase, for their continuous supports, discussions, and encouragements.

I would like to express grateful appreciation to Japan Society for the Promotion of Science (JSPS) which gave finalcial supports for me, as Grants-in-Aid for Scientific Research (KAKENHI), and Grant-in-Aid for JSPS Research Fellow (No.261738). I also express grateful appreciation to the tuition fee exemption from Osaka University.

Finally, I would like to offer my special thanks to my darling wife Taki for her invaluable supports and encouragements.

List of Publications

Main Publication

1. Chemical Environmental Effects on Muon Transfer Process in Low Pressure Mixture Gases; H_2 + CO and H_2 + CO_2

   G. Yoshida, K. Ninomiya, M. Inagaki, W. Higemoto, N. Kawamura, K. Shimomura, Y. Miyake, T. Miura, M.K. Kubo, and A. Shinohara, *Radioisotopes* **65**, 113-118 (2016).

2. Muon capture probability of carbon and oxygen for CO, CO_2, and COS under low-pressure gas conditions

   G. Yoshida, K. Ninomiya, T.U. Ito, W. Higemoto, T. Nagatomo, P. Strasser, N. Kawamura, K. Shimomura, Y. Miyake, T. Miura, M.K. Kubo, and A. Shinohara, *J. Radioanal. Nucl. Chem.* **303**, 1277-1281 (2015).

Other Publication

3. Elemental Analysis System with Negative-Muon Beam

   T. Osawa, K. Ninomiya, G. Yoshida, M. Inagaki, M.K. Kubo, N. Kawamura, and Y. Miyake, *JPS Conf. Proc.* **8**, 025003 (2015).

4. Muonic Atom Formation by Muon Transfer Process in C_6H_6 or C_6H_{12} and CCl_4 Mixtures

   M. Inagaki, K. Ninomiya, K. Fujihara, G. Yoshida, Y. Kasamatsu, M.K. Kubo, W. Higemoto, N. Kawamura, T. Nagatomo, Y. Miyake, T. Miura, and A. Shinohara, *JPS Conf. Proc.* **8**, 033004 (2015).

5. The Development of a Non-Destructive Analysis System with Negative Muon Beam for Industrial Devices at J-PARC MUSE

   M. Tampo, K. Hamada, N. Kawamura, M. Inagaki, T.U. Ito, K.M. Kojima, M.K. Kubo, K. Ninomiya, P. Strasser, G Yoshida, and Y. Miyake, *JPS Conf. Proc.* **8**, 036016 (2015).